Opto-electronics for quantum communication at cryogenic temperatures

Der Naturwissenschaftlichen Fakultät

der Universität Paderborn

zur Erlangung des Doktorgrades

Dr. rer. nat.

vorgelegt von

Frederik Thiele

am 4. August 2023

Abstract

In recent years, quantum optics enabled efficient information processing. High performing components are needed in order to preserve the quantum states of light and achieve advantage over classical processing methods. Integrated quantum photonics promises to achieve this with the on-chip integration of all essential components such as single photon sources, modulators and detectors. Lithium niobate is a promising platform to achieve integrated quantum optics due the capabilities in single photon generation with frequency conversion processes and electro-optic modulation. Furthermore, the advent of superconducting nanowire single photon detectors (SNSPDs) enables single photon detection with high detection efficiencies, low timing jitter, low dark counts, and the integration into photonic platforms. However, these superconducting detectors require cryogenic operation temperatures. In order to realize a fully capable quantum photonic platform, we want to operate lithium niobate in the cryogenic temperature regime. Furthermore, we need to combine the operation of light sources, modulators, and detectors for information processing. In this work, we establish cryogenic optical modulation of the main degrees of freedom in light by realizing cryogenic phase modulators, directional coupler, and polarization converters. Building on the cryogenic modulation capabilities, we realize optical operation methods for SNSPDs with opto-electronic components.

Zusammenfassung

Quantenoptik ermöglicht eine effiziente Informationsverarbeitung. Die optischen Komponenten müssen hierfür hohe Anforderungen erfüllen, um die Quantenzustände des Lichts und eine Quantenüberlegenheit gegenüber klassischen Methoden zu erhalten. Integrierte Quantenphotonik verheißt diese Überlegenheit zu ermöglichen, indem essenzielle Komponenten wie zum Beispiel Einzelphotonendetektoren, Modulatoren und Detektoren auf Chips integriert werden. Lithiumniobat ist eine vielversprechende Plattform um integrierte Quantenphotonik zu realisieren, da Einzelphotonengeneration mit Frequenzkonversionsprozessen und elektro-optischer Modulation in diesem System umgesetzt werden kann. Zusätzlich ermöglicht das Aufkommen von supraleitenden Dünnschicht-Einzelphotondetektoren (SNSPDs) eine hohe Detektionseffizienz, ein geringes Taktzittern, ein geringes Dunkelrauschen und eine gute Integrierbarkeit in photonische Systeme. Allerdings benötigen diese supraleitenden Detektoren kryogene Arbeitstemperaturen. Um vollumfängliche quanten-photonische Systeme zu realisieren, werden wir Lithiumniobat-Schaltkreise in diesem Temperaturbereich betreiben. Zusätzlich müssen wir den Betrieb von Lichtquellen, Modulatoren und Detektoren zur Informationsverarbeitung testen. Im Rahmen dieser Dissertation werden wir zeigen, dass die fundamentalen Eigenschaften des Lichts mit kryogenen Phasenmodulatoren, direktionalen Kopplern und Polarisationskonvertern manipuliert werden können. Zusätzlich werden wir opto-elektronische Betriebstechniken von supraleitenden Detektoren entwickeln, die auf den kryogenen Modulationsfähigkeiten aufbauen.

Contents

Introduction 1

Light is widely used in communication applications. Optical communication developed from simple light pulsing with morse code to high data transmission rates with optical fibers and lasers. Several innovations sparked strong improvements in light technologies such as the laser, optical fibers, integrated optical circuits, optical modulators and photodiodes. These technologies also opened new application fields such as quantum optics. The continuous exploration in optics enables to use quantum effects to our advantage.

In recent years, several applications showed that a quantum advantage over classical methods can be achieved in metrology, computation and communication. For example, in metrology applications, the signal to noise ratio has been improved in interferometers for gravitational wave detection [1]. Additionally, quantum communication protocols have been implemented to build secure networks [2]. First studies have shown that a quantum advantage can be achieved in quantum processing to generate random numbers or to execute gaussian boson sampling [3–5].

Quantum optics is one out of many quantum systems which can be realized. In this field, photons are the carriers of quantum states of light. Similar systems have been established for quantum information processing such as Rydberg atoms [6] or superconducting circuits [7]. These systems rely on light or RF-pulses for the signal transmission. Photons as information carriers have the advantage of a low decoherence such that long distance communication can be achieved, in comparison to the direct interaction of Rydberg atoms and superconducting circuits. Furthermore, the main properties of light can be deliberately manipulated on the single photon level such as the phase, polarization, propagation direction or wavelength [8]. In addition, quantum optics can rely on a mature basis of optical technologies such as lasers, optical fibers and photodiodes.

Low loss transmission is mainly enabled by optical fibers which confine the light and achieve low scattering losses. Furthermore, light confinement and waveguiding can also be achieved with waveguides on photonic chips. The waveguide integration can enable a reduction the footprint of optical devices. In addition, these photonic platform promise to be noise resilient and reduce propagation losses in comparison to free space components.

The low transmission losses, an increase in the complexity and the deliberate manipulation of photons is sought after in quantum optics. Integrated optics can therefore enable quantum communication on a larger scale. To achieve this, high quality waveguide platforms are needed which can enable the generation, manipulation, transmission and detection of quantum states of light.

Several integrated photonic platform have been proposed for quantum communication such as Si, SiN and lithium niobate [9, 10]. Low loss waveguiding is achieved in all of these

materials. In the ideal material system a quantum light source, optical modulators and single photon detectors are integrated on the waveguides.

To detect quantum states of light, single photon detectors are desired. One of the highest performing single photon detectors are Superconducting Nanowire Single Photon Detectors (SNSPDs) which can achieve near unity detection efficiencies [11, 12], low timing jitter [13], low dark count rates [14] and can be integrated with waveguides [15]. These detectors require cryogenic operation temperatures to achieve superconduction in the thin film structures [16]. To integrate these devices on waveguides, the integrated photonic structures have to be adapted to cryogenic operation temperatures.

One of the most promising candidates for integrated quantum photonics is lithium niobate [8]. This platform can achieve low transmission losses with titanium in-diffused waveguides [8] or with thin-film ridge waveguides [17]. Furthermore, the material's large second order nonlinearity can be exploited for frequency conversion processes to generate quantum states of light [8, 18]. The light can be manipulated due to the electro-optic properties [19]. Light generation combined with electro-optic modulation has even been shown on single integrated chip to achieve Hong-Ou-Mandel interference[20–22]. With the advent of SNSPDs, single photon detection has been achieved by integrating these detectors on chip [15].

Exploring the capabilities of lithium niobate as a fully capable quantum photonic system will require the combined operation of sources, modulators, and detectors. The cryogenic operation temperature of superconducting detectors dictates a cryogenic temperature environment for the entire integrated circuit [23]. The low noise nature of cryogenic temperatures can be seen as beneficial for sensitive processes such as single photon detection[24]. The cryogenic temperatures will require further investigations whether the nonlinear processes are possible and how the system might be optimized at cryogenic temperatures. Cryogenic frequency conversion processes such as sum frequency generation [25] and parametric down conversion has been achieved in lithium niobate [26]. Initial investigations have shown that electro-optic modulation is possible with lithium niobate at cryogenic temperatures with intensity modulators [27, 28]. However, we are interested to establish optical modulation for the main principles of light namely; phase, direction and phase. To that end, we further investigate active modulation of these properties of light in lithium niobate at cryogenic temperatures.

Focusing on the combined operation of superconducting detectors and electro-optic modulators, three main challenges are revealed to enable quantum photonic circuits:

- Realization of reconfigurable optical components through integrated electro-optic modulators with integrated single photon detectors.
- Signal readout of single photon detectors using cryogenic electro-optic modulators to reduce thermal overhead in cryogenic systems.
- Achievement of feed-forward modulation using superconducting detectors and cryogenic electro-optic modulators for fast deterministic quantum photonic processing.

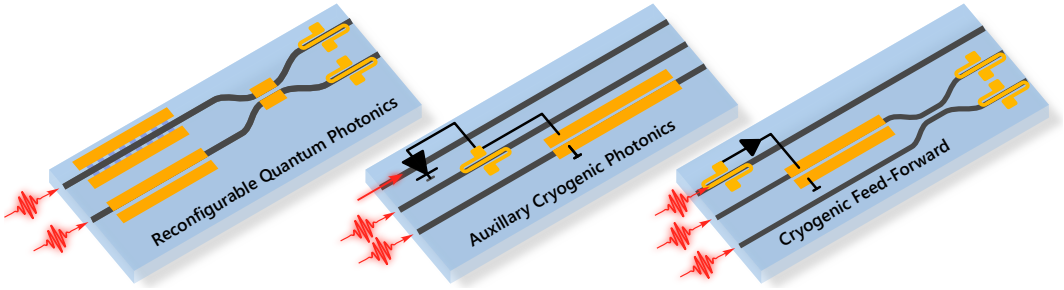

Figure 1.1: Integrated photonic circuits suggested to realize the operation of electro-optic modulators and integrated single photon detectors. Reconfigurable photonics can be realized by integrated modulators. The all-optical operation can be realized by integrated photodiodes and electro-optic modulators. Pushing the previous schemes further, cryogenic feed-forward modulation could be realized by integrated components.

This work aims to explore the capabilities of cryogenic electro-optic modulators fabricated from lithium niobate waveguides for enabling quantum photonic applications with superconducting detectors. We intend to overcome these challenges to promote lithium niobate modulators and SNSPDs as fully capable photonic components in integrated quantum optics. The mentioned main challenges are experimentally investigated and discussed in the following chapters. Figure 1.1 highlights how these main schemes for quantum light processing and communication could be realized in with integrated cryogenic photonics.

Outline

At first electro-optic modulation is investigated at cryogenic temperatures in chapter 2. Reconfigurable photonic components are needed to fine adjust and set up the degrees of freedom of light in the cryogenic environment such as the relative phase between optical paths, the splitting ratio in a beam splitters or polarization of light. Integrated modulators can manipulate the same properties deliberately. To realize a fully integrated quantum photonic circuit we must realize these reconfigurable optical components with SNSPDs at cryogenic temperatures. Initially, we realized a polarization modulator and characterized it from room temperature down to cryogenic temperatures, in section 7.1. To show the full manipulation capabilities of lithium niobate modulators, we establish that phase modulation, directional coupling and polarization is possible in this material platform, in section 7.2. The characterizations revealed that the optical properties can be perturbed during the cooling process of the material system. To investigate this, we further characterized the perturbations and show that the optical perturbations can be linked to the generation of pyroelectric charges in the cooling warming process, in section 7.6. Fortunately, modulators operated at cryogenic temperatures experience no further optical perturbations when this temperature range is reached. Combined with the integration of SNSPDs on lithium niobate waveguides, this platform could be seen as a reconfigurable quantum photonic platform.

Increasing the size and complexity of quantum photonic circuits will require a plurality of modulators and detectors. Typically, these components are controlled over transmission lines spanning from the controller to the device. Using these typical interconnects between room temperature electronics and the cryogenic photonic components will reveal that heat and electronic noise is conducted. In chapter 3 we investigate methods to overcome the heat conducting of typical transmission lines for cryogenic circuits and replace them with opto-electronic power delivery and optical readout techniques. At first, we established a method for optical-to-electric power conversion to operate an SNSPD with a cryogenic photodiode, in section 7.3. In this study a similar performance was observed in comparison to the typical operation of an SNSPD. We show an all-optical method to operate an SNSPD by combing an optical power delivery with the established electro-optic modulation, in section 7.4. All interconnects are replaced by single mode fibers such that the cryogenic photodiode and electro-optic modulators acts as converters between optical and electrical signals. In the chapter 3, we explore the concepts of the involved single photon detectors, power delivery, cryogenic signal amplification and optical signal readout as well as the application of the SNSPD operation.

The characterization of the all-optical operation of an SNSPDs reveals the key strength and weaknesses in the optical readout. Furthermore, the realization of this operation method highlights how the combined operation can be optimized. Ideally, we want to achieve a full optical modulation from a single photon detection event. In quantum photonics this direct manipulation of single photons is desired for quantum processing. This feed-forward modulation can enable the operation of controlled NOT gates when applied to entangled sets of photons. The realization of CNOT gates is desired to achieve universal quantum computation schemes [29, 30]. In the final chapter 4, we will take the all-optical operation of an SNSPD as a case study and an outlook on how cryogenic feed-forward modulation can be achieved. The key figures of merit of the all-optical operation are extracted and extrapolated.

An adaption to a cryogenic temperature is at the moment unavoidable for single photon processing with integrated photonics. This work will explore key concept of electro-optic modulation combined with single photon detection to enable quantum photonics. Solving and understanding these challenges drives photonics further towards fully integrated quantum processing.

Reconfigurable Cryogenic Photonics

2

Declaration:
The ideas and content presented in this chapter are partly taken from the following publications:

- Thiele et al. "Cryogenic electro-optic polarisation conversion in titanium in-diffused lithium niobate waveguides," in Opt. Express, vol. 28, no. 20, p. 28961, Sep. 2020. The publication is presented in section 7.1.
- Thiele et al. "Cryogenic electro-optic modulation in titanium in-diffused lithium niobate waveguides," in J. Phys. Photonics, vol. 4, no. 3, p. 034004, Jul. 2022. The publication is presented in section 7.2.
- Thiele et al. "Pyroelectric Influence on Lithium Niobate During the Thermal Transition for Cryogenic Integrated Photonics," in arXiv:2306.12123, Jun. 2023. The publication is presented in section 7.6.

Quantum optics relies on linear optical components such as beam splitters and waveplates [30, 31]. Key features are of light can be manipulated with the combination of these components such as the phase, direction, and polarization. On the path towards large scale quantum applications, a plurality of optical components are needed [9, 32]. Integrated photonics promises to increase the component density of these components while maintaining high optical performances. In integrated photonics these key features of light can be manipulated by integrated phase modulators, polarization converters and directional couplers [8]. Realizing fully integrated quantum photonic processing will require the additional integration of single photon sources and detectors [33].

One of the highest performing single photon detectors are superconducting nanowire single photon detectors (SNSPDs) [23, 24]. Their near unity detection efficiency [11, 12], low timing jitter [13] and low dark count rates [14] is most suitable for quantum applications. Integrating these detectors in photonic networks will require an adaptation of the circuits for the detector's cryogenic operation temperature. Integrated SNSPDs have been shown in a variety of photonic platform such as Si, SiN and lithium niobate waveguides [15].

An ideal quantum photonic platform must prove that all components from the source to the detector can be operated together. To that end, we need to choose a platform in which all three components can be realized at cryogenic temperatures. Partitioning this

issue reveals that the integrated of integrated quantum light sources and modulators as well as modulators and single photons detectors need to be shown. For example, for quantum light sources the integration of parametric down conversion and electro-optic modulation has been shown to achieve Hong-Ou-Mandel interference on a single chip [20]. Furthermore, the implementation of the parametric down-conversion [26] as well as the integration of SNSPDs [34, 35] has been shown in the same material system at cryogenic temperatures. To further push cryogenic photonics, we need to explore optical modulation in this environment.

In this chapter, we will explore which type of optical modulation is available in cryogenic photonics in section 2.1. Our choice of a quantum photonic platform is dictated by the capability of integrated single photon sources, optical modulation, and single photon detection. The previous examples highlight that in lithium niobate waveguides are suitable to do this at cryogenic temperatures. Quantum light generation can be achieved by cryogenic frequency conversion [25, 26], optical modulation is achieved by cryogenic electro-optical modulation [28, 36] and single photon detection can be realized by SNSPDs [34, 35]. To explore electro-optic modulation capabilities in detail at cryogenic temperatures, we characterized at first a polarization modulator in section 7.1. Furthermore, to highlight the full capability of the lithium niobate platform, we characterized a phase modulator, directional coupler and polarization converter in section 7.2.

These investigations in the device performance reveal that the electro-optic modulation is working in a temperature range from room temperature to cryogenic temperatures. During the characterization optical and electronic perturbations occurred in the lithium niobate waveguides. To investigate the origin of the effect, we additionally measured the changes in the waveguide's birefringence and the detected pyroelectric charges during the temperature change from room temperature to cryogenic temperatures. We will show in section 7.6 the optical and electronic perturbations can be correlated and linked to pyroelectric charge generation.

In summary, we can show that lithium niobate is a capable platform for quantum photonics and can be adapted for the use in the cryogenic temperature environment.

2.1 Cryogenic optical modulation

In photonic networks light is used as the transmission medium of information. Optical modulation is employed to imprint information deliberately in the photonic network by changing properties of light namely; phase, direction, polarization and wavelength. One of the most common techniques to change these properties is the modulation of the refractive index. Various refractive index modulation methods can be used by temperature dependent effects, electro-optic effects, magneto-optic effects, strain and carrier injection [37]. In photonic networks materials with a strong refractive index response and a fast change in the refractive index are desired. Minimizing transmission losses is of high interest to reduce the overall loss for quantum applications. In addition, a platform with light confinement is

desired to generate a large interaction between the refractive index perturbation and the transmitted light.

In this work, a material system is needed which can realize quantum photonic platforms. To that end, the modulators must be integrated in low loss waveguides. Furthermore, generation of quantum light and single photon detection should be achievable by system integration. As highlighted in section 1 and 3.1, single photon detection will require cryogenic operation temperatures. Optical modulation must be therefore established at cryogenic temperatures, ideally with a low thermal power dissipation. To that end, we will investigate lithium niobate as a cryogenic optical modulation platform in section 7.1 and 7.2.

Optical modulation at cryogenic temperatures is an active field of research due to the advent of superconducting single photon detectors. Several modulation platforms have been established for room temperature applications and are converted for cryogenic temperatures. Thermo-optic phase shifters are commonly used for telecommunication applications with integrated Si-circuits at room temperature photonics. However, in Si, SiN and SiO-waveguides the thermo-optic effect decreases by several orders of magnitude at cryogenic temperatures [38, 39]. Moreover, these devices dissipate heat into the waveguides such that their low power performance is limited. Alternatively, the refractive index can be changed by carrier injection in semiconductor waveguides. The challenge in these devices is to mitigate the risks of carrier freeze out at cryogenic temperatures. The decreased temperature will reduce the free carrier density generated by thermal carriers. Recently, a ring-resonator-modulator has been realized below 5 K as a cryogenic modulator [40, 41] which has overcome this challenge.

An initial study has recently shown the operation of magneto-optic modulators which alters the waveguides refractive group index by a magnetically sensitive material. This technology is promising to be operated with superconducting circuits such as SNSPDs which are current modulating devices. Diverting the SNSPDs bias current after the detection could generate changes in the magnetic fields with electro-magnets for an optical signal readout [42]. However, achieving this application will require additional optimizations in the operation current.

Electro-optic modulators are widely established and high performing due to their operation speed and low operation voltages in material systems such as lithium niobate. Initial investigations adapt the established technology for cryogenic operation temperatures [27, 36, 43]. In electro-optic materials a refractive index change is achieved by inducing a constant electric field in the material. The electric field for optical modulation is typically generated by a capacitor structure realized by electrodes placed around the waveguide. The change in the waveguides refractive index is scaled by electro-optic coefficient r_{ij} (Pockels coefficient) depending on the incident direction of the applied electric field E_j [37, 44] The placement of the electrodes can be optimized to achieve a large overlap between the electric field and transmitted light. This will reduce the modulation voltage to induce a refractive index change. The modulation voltage for the electro-optic modulator can be generated and signals can be amplified by a mature variety of electronic platforms. Furthermore, the

electrode structures of the modulator can be optimized for high modulation speeds since it it mostly limited by the electronic characteristics of the electrodes [45, 46]. The shunt resistance of the electrodes is very large in for most electro-optic materials. Furthermore, the thermal power dissipation of electro-optic modulators is mostly dependent on the RF-resistance during the capacitive loading and unloading. To minimize the power dissipation the electrodes impedance should be matched to the impedance of the signal generator such that electronic reflections are avoided.

2.1.1 Theory: electro-optic modulation

In this work, several electro-optic modulators are realized and the publications 7.1 and 7.2 will describe the theoretical background in more detail. In these modulators, the waveguide's refractive index $\tilde{n}_i$ is deliberately altered by inducing an electric field E_j with an electrode structure. The change in the reciprocal refractive index $\Delta(1/n_i^2)$ is scaled by the electro-optic coefficient r_{ij} [37, 44];

$$\Delta\left(\frac{1}{n_i^2}\right) = r_{ij}E_j, \tag{2.1}$$

$$\Delta n_i \sim \frac{\tilde{n}_i^3}{2} r_{ij}E_j \tag{2.2}$$

The change in the refractive index Δn_i is dependent on the direction ij of the incident electric field.

The modulators alter the output state of incoming light. To describe the change of an input state A_{in} to an output state A_{out}, the transformation can be described by a linear equation with a transfer matrix M,

$$A_{\text{out}} = M \times A_{\text{in}}. \tag{2.3}$$

In this description, the input input state is represented by the amplitudes $a_{m,l}$ with the input vector $A = (a_m, a_l)^T$. The indices can represent either two orthogonal polarization states or two outputs of spatial channels. The modulators couple light from one channel to the other. For each modulator a coupling parameter κ can be derived for a given input wavelength λ and applied voltage V to the electrodes,

$$\kappa = \frac{\pi\tilde{n}_i^3 r_{ij} V \eta}{\lambda G}. \tag{2.4}$$

In this representation, the electrode geometry is summarized as the electrode gap G and the overlap between the optical modes and the electric field η. The overlap between the optical mode of the waveguide $E_{m,l}$ and the induced electric field E^{DC} can be derived from

a normalized field overlap:

$$\eta = \frac{G}{V} \frac{\int_A E_m^* E^{\mathrm{DC}} E_l \mathrm{d}A}{\sqrt{\int_A E_m^* E_m \mathrm{d}A \int_A E_l^* E_l \mathrm{d}A}}. \tag{2.5}$$

The full transfer matrices and the exact coupling parameters are given in section 7.2. The transfer matrix for the phase modulator is given in equation 7.11 for the phase modulator, in equation 7.16 for the directional coupler and in equation 7.18 for the polarization converter.

2.1.2 Integrated cryogenic modulators

A large variety of electro-optic materials have been investigated and developed for a room temperature operation of photonic networks. Figure 2.1 shows a summary of electro-optic materials which have been established with their respective Pockels coefficients. A large electro-optic coefficient is beneficial since this minimizes the applied modulation voltage to achieve a desired optical modulation. Figure 2.1 shows that Pockels coefficients of up to 1000 pm/V can be achieved by material such as BaTiO3. In comparison, lithium niobate, which is a well-established material system, achieves an electro-optic coefficient of about 30 pm/V.

We seek a photonic platform for quantum optical applications in which quantum states of light, optical modulation and the detection of quantum states of light can be achieved. Choosing superconducting detectors for single photon detection dictates a cryogenic operation temperatures. The choice of photonic platforms for active quantum optics will be determined by the capability to integrate single photon sources, low waveguide losses, low interface losses, the capability to integrate SNSPDs and the modulation strengths of integrated modulators. Table 2.1 summarizes photonic platforms in which cryogenic optical modulation is established. Key characteristics are highlighted such as the required

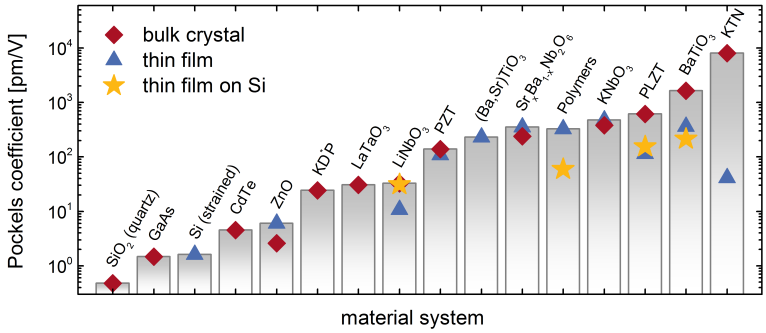

Figure 2.1: Electro-optic coefficients of different materials at room temperature. This figure is copied from [47].

modulation input to generate a change in optical output state. Additionally, the table highlights the kind of optical property altered such as the amplitude of the output intensity, relative phase to a reference beam, propagation direction or polarization. Furthermore, material the platform and operation wavelength is summarized. It becomes apparent in table 2.1 that Si, SiN and SiO photonic platforms have no optical modulation properties at cryogenic temperatures. To achieve optical modulation in these plaforms additional optically active materials are deposited and integrated in these structures. We highlight these hybrid structures in table and discuss hybrid modulation platform in further detail in section 2.1.5.

type	waveguide	active material	platform	altered opt. property	modulation	wavelength	Ref.
magneto-optic	Si	Ce:YIG	hybrid	amplitude (ring)	200 pm/mA	1550 nm	2022 [41]
electro-optic	Si	BaTiO	hybrid	amplitude (MZI)	5 Vcm	1550 nm	2020 [48]
electro-optic	Si	BaTiO	hybrid	amplitude (ring)	200 pm/V	1550 nm	2020 [48]
carrier-injection	Si	Si-diode	monolithic	amplitude (ring)	50 pm/V	1550 nm	2017 [40]
carrier-injection	Si	InP-diode	hybrid	amplitude (ring)	20 pm/V	1550 nm	2022 [42]
carrier-injection	Si	diode	monolithic	amplitude (ring)	200 pm/V	1300 nm	2021 [49], 2021 [50]
carrier-injection	Si	diode	monolithic	amplitude (ring)	1 nm/V-10 nm/V	1550 nm	2020 [51]
opto-mechanical	SiN	piezo (AlN)	monolithic	amplitude (ring)	24 Vcm	780 nm	2019 [52]
opto-mechanical	SiN	piezo (AlN)	monolithic	amplitude (MZI)	5 pm/V	780 nm	2019 [52]
opto-mechanical	SiN	piezo (AlN)	monolithic	amplitude (MZI)	65 Vcm	780 nm	2022 [53]
opto-mechanical	SiN	-	monolithic	amplitude (MZI)	0.16 Vcm	1550 nm	2022 [54]
opto-mechanical	SiN	-	monolithic	amplitude (MZI)	0.48 Vcm	1550 nm	2021 [55]
electro-optic	SiN	graphene	hybrid	amplitude (ring)	0.8 dB/V	1550 nm	2020 [56]
electro-optic	SiO	polymer	hybrid	amplitude (MZI)	0.2 Vcm	1550 nm	2022 [57]
electro-optic	TFLN	LN	monolithic	amplitude (MZI)	2.6 Vcm	1550 nm	2021 [58]
electro-optic	Ti:LN	LN	monolithic	phase	48 Vcm	1550 nm	2020 [59], Sec. 7.2
electro-optic	Ti:LN	LN	monolithic	polarization	20 Vcm	1550 nm	Sec. 7.1 and 7.2
electro-optic	Ti:LN	LN	monolithic	direction	52 Vcm	1550 nm	Sec. 7.2
electro-optic	Ti:LN	LN	monolithic	amplitude (Michelson)	13.2 Vcm	1550 nm	Sec. 7.4
electro-optic	Ti:LN	LN	monolithic	amplitude (MZI)	8 Vcm	1300 nm	1992 [36],1999 [27]

Table 2.1: Overview of integrated modulators operated at cryogenic temperatures. Waveguides with additionally added or integrated optically active structures are considered as hybrid structures. The modulation strength of the structures are normalized to the electrodes length. Furthermore, the modulation strength is summarized as the electronic input required to induce a phase shift at the output of $\pi/2$ or to achieve a detuning of the transmission wavelength in a resonant structure.

2.1.3 Cryogenic titanium in-diffused lithium niobate

Lithium niobate is a promising platform for quantum optics [8, 20]. Titanium in-diffused lithium niobate waveguides are established for the quantum application at cryogenic temperatures. In particular, low-loss waveguiding, single photon generation by spontaneous parametric down-conversion [26, 60], integrated superconducting single photon detectors [34, 35, 61] and electro-optic modulation has been individually shown at cryogenic temperatures [36, 43, 58] (and this work in section 7.1 and7.2). These initial works show a great promise for a monolithic realization of photonics such that interface losses can be avoided in this material. At room temperature, the monolithic integrated chip of more than one device has been shown. To do so, parametric down-conversion and electro-optic modulation has been been combined to achieve Hong-Ou-Mamdel interference single chip in lithium niobate [20]. We are interested to exploit quantum phenomena like these on chip and expand the capabilities by integrating superconducting single photon detectors. In the scope of this work, we investigate the cryogenic performance of lithium niobate modulators such that they can be directly integrated with the established single photon detectors and cryogenic frequency converters.

In this platform, light confinement is achieved by raising the refractive index by titanium in-diffusion at the surface of the substrate. The realized waveguides are well matched to standard single mode fibers such that high coupling efficiencies of approximately 90% can be achieved [62]. These initial investigations mainly focused on z-cut lithium niobate in which the crystal axis is pointing in the direction of the top surface plane [18]. Initially we investigated waveguide coupling between single mode fibers and lithium niobate waveguides at cryogenic temperatures with fiber-to-fiber efficiencies of up to 43%, as discussed in section 7.1. Building on these results we have shown that electro-optic modulation is possible in lithium niobate by realizing a polarization converter below 1 K, which we investigate in the following in section 7.1. To highlight the full capabilities of the lithium niobate platforms we further investigate in section 7.2 that phase modulation, directional routing and polarization modulation with electro-optic modulators can be realized at cryogenic temperatures.

In these investigation, we have observe a temperature dependent change in the refractive index resulting in a shift in the wavelength dependent behavior of the devices. In particular, the operation wavelength of the polarization converter shifted by about 100 nm around 1550 nm. In addition, we observe a temperature dependent shift in the electro-optic coefficient. As a result the required operation voltage to induce the same optical change almost doubled. During the thermal transition between room temperature and cryogenic temperatures pyro-electric charges are generated in lithium niobate which influence the point of operation for these devices. We discuss the influence of pyroelectric charges in section 7.6. In summary, the optical characterizations show that an pyroelectric influence vanishes in lithium niobate at cryogenic temperatures [58, 63–65].

2.1.4 Cryogenic thin-film lithium niobate

An alternate form to realize lithium niobate waveguides are ridge waveguides. In this platform, a lithium niobate thin film is deposited on a base substrate such as Si, SiO or SiN [17, 66]. The ridge waveguide is designed such that light confinement is established between the lithium niobate and air as well as lithium niobate and base substrate [17, 66]. The main advantage of this material system is that a stronger confinement in comparison to titanium in-diffused lithium niobate waveguides is achieved. The stronger confinement enables tighter bending radii and an increased electric-to-optical field overlap to enhance the electro-optic modulation capabilities. As a result, low modulation voltages in the sub-volt range have been realized with integrated modulators [67]. Furthermore, the dispersion of the waveguides can be optimized by the ridge waveguides dimension to improve the mode matching and therefore the dispersion in frequency conversion processes [68, 69]. Furthermore, in thin film lithium niobate the integration optical components has been shown such as quantum dots as single photon sources [70], electro-optic modulators and integrated single photon detectors[58, 71].

Thin film lithium niobate is more compact material platform than titanium indiffused lithium niobate. More optical devices can be realized on the same footprint and the tighter bending radii offer more capabilities to scale up this photonic networks. Light coupling from the waveguide to single mode fibers is mainly achieved by grating couplers which introduce transmission losses in the coupling to single mode fibers [58, 71, 72].

This platform has been established for room temperature and expanded into the cryogenic environment. In the thermal transition between these temperatures the influence of pyroelectric charges has not been investigated yet. Initial reports show that bias drifts are observed at room temperature, especially if a resistive cladding structure is placed around the waveguides [22, 58]. Furthermore, the reports show that bias drifts are strongly reduced when operated at cryogenic temperature [58]. This could be explained by the reduced pyroelectricity at cryogenic temperatures, which we investigate in section 7.6.

2.1.5 Cryogenic hybrid photonic platforms

Integrated photonic networks are well established in Si and SiN at room temperature. In particular, the fabrication process is mature enough to enable large scale and high quality wafer production. However, these platforms cannot achieve a significant optical modulation at cryogenic temperatures. Introducing optically active structures in the vicinity of the waveguides can introduce an optical modulation. A large variety of these hybrid structures have been established even at cryogenic temperatures, as it is highlighted in table 2.1.

In these platforms, the waveguides are realized in a ridge waveguide geometry. Tight light confinement promises in this platform scalability for large scale application. The generation of quantum states of light can be achieved spontaneous four wave mixing in spiral

waveguides [73] or by the integration of quantum dots [74]. In addition, superconducting single photon detectors have been successfully integrated in these platforms.

Unfortunately, two photon absorption can introduce large losses in the Si-waveguides [74]. To that end, SiN is established as silicon platform to mitigate this risk. Furthermore, Si and SiN have no fast modulation capabilities like the electro-optic effect. Monolithic Si and SiN offer a thermal-optic effect which is slow, dissipates heat in the photonic chips and vanishes at cryogenic temperatures. To achieve high speed optical modulation in Si and SiN, hybrid structures have been developed for optical modulation also at cryogenic temperatures; namely BaTiO3 [48], InP[75] and polymers [57] for electro-optic modulation.

BaTiO3 has the benefit of a large electro-optic effect at cryogenic temperatures and the substrate can be epitaxially grown with conventional semiconductor technologies [48]. Initial results of heterogeneously integrated InP modulators have shown high modulation speeds at cryogenic temperatures [75]. One of the highest modulation bandwidths have been shown on hybrid polymer waveguides at cryogenic temperatures in excess of several GHz [57]. One of the lowest modulation voltages for electro-optic modulation has been shown in integrated diode structures for carrier injection at cryogenic temperatures[40, 51]. The challenge in diode structures at cryogenic temperatures is the mitigation of the risk of carrier freeze-out.

In addition to these Si and SiN hybrid structures, initial results of hybrid structures with lithium niobate as the active material has been shown at room temperature [76, 77]. These hybrid lithium niobate structures offer to combine the strength of each platform. However, the compatibility of the hybrid integrated lithium niobate structures have to be shown even at cryogenic temperatures.

An ongoing challenge for all of the aforementioned hybrid photonic structures is the insertion loss towards the photonic structures. The losses are generated either by the coupling from one waveguide to the other or by scattering on the interface in the multi-material systems. Furthermore, the Si and SiN waveguides have typically a coupling loss of about 3 dB with single mode fibers [78]. Some techniques to improve the waveguide coupling have been employed [78]. Reducing losses in these photonic networks will continue to be a challenge which will need further improvements to elevate quantum photonic processing

2.2 Electro-optic characterization methods at cryogenic temperatures

Quantum photonics requires electro-optic modulators to manipulate light in the cryogenic environment. Our platform of choice is titanium in-diffused lithium niobate waveguides due to the highlighted capability to integrate frequency conversion sources and single photon detectors. Alongside these investigations, we are interested to build a versatile platform for light manipulation of the phase, direction and polarization. The realization of lithium niobate phase modulators, directional couplers and polarization converters has been well established at room temperature and their technology has been even packaged as commercial devices. However, the conversion of the lithium niobate electro-optic modulators for the cryogenic operation environment is not trivial. In the following, the challenges and methods are highlighted to establish cryogenic lithium niobate modulators for the manipulation of the phase, direction and polarization. The concepts, methods and results are presented in the publications in section 7.1, 7.2 and 7.6.

The electro-optic modulators are realized as integrated devices with titanium-indiffused waveguides. In electro-optic characterizations in section 7.1 and 7.2 , light is coupled into the waveguides while a voltage sweeps are applied to the electro structure. Changes in the optical properties are then detected in the setup such as the output polarization, relative phase between light beams or the intensity at a waveguide port. In addition, the operation wavelength is changed to determine the wavelength dependent characteristics. In these measurements key figures of merit are extracted such as the voltage required to switch from one output state to the other and the wavelength of the most efficient operation.

Optical access and light transmission:
The modulators waveguides are optimized for a large optical mode overlap with standard single mode fibers at room temperature [8, 79]. Coupling efficiencies of approximately 88% can be achieved [62]. As a result, two main techniques can be applied to achieve an optical access to the waveguides. Either a single mode fiber can be attached to the endfacet known as pigtailing or butt coupling [62]. An alternative method is to couple light into the waveguide with a lens. Both methods have their respective challenges in the implementation at cryogenic temperatures.

Pigtailing:
In the initial characterization of the polarization converter, we needed to establish if the lithium niobate waveguide is transmissive at cryogenic temperatures. To test the optical transmission of the waveguides and the coupling to the single mode fibers, we monitored the optical transmission of light during the cooling process. These titanium in-diffused lithium niobate waveguides are transmissive at cryogenic temperatures and fiber-to-fiber efficiency of approximately 43% is achieved in comparison to a 55% transmission efficiency at room temperature. This measurement indicates that the optical mode is not significantly altered and no significant effect is introduced which induces strong changes in

transmissivity. We mainly attribute the change in the transmission to mechanical changes in the fiber-to-waveguide coupling.

The main challenge in the pigtailing is to package the lithium niobate sample and single mode such that the device maintains a high mechanical stability during the temperature changes between room temperature and cryogenic temperatures. The fibers are attached to the sample in a pigtailing process. To do so, the sample is placed on a sample holder and an optical access is realized with lens coupling system. Light is then coupled through the lithium niobate waveguides and the alignment is optimized by the optimization of the optical throughput. In the next steps, the lens-incoupling is replaced with a single mode fiber. The fiber is then moved close to the waveguide with a mechanically actuated stage. The fibers position is aligned again by the optimization of the transmitted power. To adhere the fiber to the samples endfacet, a UV-adhesive is placed at the fiber tip. After a realignment of the fibers position, the adhesive is cured by illuminating it. A UV curable adhesive is chosen which has a low contraction during the curing process (Norland 81 [80]) to mitigate coupling shifts in the curing process. Further studies on cryogenic adhesives suggest to use similar adhesives for cryogenic optical coupling [81].

To enlarge the cross section of the fiber tip and therefore increase the adhesion, a fiber with a glass ferrule is chosen. The mechanical stability of the pigtailed is further increased by installing so-called tension release blocks. The lithium niobate sample sits on a metal block and side blocks are attached such that they extend over the edge of the sample towards the fibers. The fibers are adhered to the side blocks with the UV-adhesive such that mechanical stress are taken by side blocks instead of the fiber-to-waveguide interface. The sample sticks to the sample holder with vacuum grease (Apiezon N [82]) such the sample can be slightly move under mechanical stress and conduct heat better to the sample holder.

The pigtailing technique enables an optical access in a temperature range from 0.8 K to 300 K. In addition, multiple waveguides can be coupled by a multicore fiber core ferrule. Unfortunately, the fibers can become loosen during the cooling process at the interface between the UV-adhesive and the fiber ferrule. Mechanical stresses in the mechanical joint can overcome the adhesion. Once a pigtailed sample is in the cryogenic temperature range and a high transmission is achieved, the high transmission remains in the sample. Increasing the yield of the sample will need further investigations to improve the adhesion as well as the packaging of the device.

Free-space coupling:
An alternative method to achieve an optical access to the lithium niobate waveguides at cryogenic temperatures is with free space optics. In this method, the sample is placed in a cryostat with windows in the sample chamber to achieve an optical access. The light is coupled into the waveguide with a lenses placed on the room temperature side of the cryostat. The main advantage of this system is that versatile optical setups can be achieved around the sample. Furthermore, the coupling into the waveguides can be readjusted if the mechanical alignment shifted after a temperature change in the cryostat. The cryostat must be optimized for low vibrations of the mechanical stages to maintain a high coupling efficiencies.

Electric-optical characterizations:
The modulation voltage of the modulators is expected to change with the change of temperature since the related electro-optic coefficient decreases with the decrease in temperature [83]. Sweeping the voltage and simultaneously acquiring the optical output allows us to extract the modulation voltage. In this work, we extract the modulation voltage in a temperature range from 300 K to below 10 K. This shows that the electro-optic modulation is preserved in this range. Furthermore, the modulation voltage increases for the modulators by a factor of about 2 from room temperature to cryogenic temperatures.

In addition to the modulation voltage, the operation wavelength is swept in the characterization. The realized polarization converter and directional coupler show a wavelength dependent coupling dependence of the output states. This mainly attributes to the dispersion of the birefringent lithium niobate. To investigate this, we sweep the input voltage and wavelength at different operation temperatures. The directional coupler shows that the wavelength of the bar state shifts by approximately 85 nm over the entire temperature range (the state in which the intensity remains in the same output side as the input of the coupler). In addition, the operation wavelength of the polarization converter shifted by about 107 nm from 300 K to 8 K.

The characterization of the polarization converter was challenging during the cooling process since the wavelength and voltage sweeps needed to be performed around the phasematched wavelength. The phasematched wavelength shifted constantly during the cooling process. To balance the acquisition time of the voltage and wavelength sweeps with the wavelength scanning range, we generated a algorithm which identifies the phasematched wavelength from the previous measurements. The subsequent measurements are adjusted to be centered around the phasematched wavelength. The voltage and wavelength sweeps revealed that this overall modulation map was continuously distorted during the cooling process. A possible cause was appointed to pyroelectric charge build up in the sample which could generated additional electric field in the sample.

Refractive index extrapolation:
The electro-optic characterizations reveal that the waveguides refractive index shifts with the temperature and operation wavelength. Ideally, we design and fabricate a modulators for a specified cryogenic operation wavelength. To better inform the design the process in the future for integrated devices, we simulated and extracted the waveguide's refractive index and performed the electro-optic characterizations. In particular, the polarization converter is strongly dependent on the waveguides dispersion since the conversion process is most efficient at the phase matched wavelength in the periodically poled structure. To extract the phase matched wavelength in the temperature range from 300 K to 1 K, we made continuous sweeps wavelength and voltage sweeps around the phase matched wavelength during the cooling process.

As a comparison, we simulated the waveguides refractive index and dispersion with a finite difference method [84]. This model takes the refractive index of the birefringent lithium niobate from the Sellmeier equations and extrapolates them to cryogenic temperatures [85]. In addition, the refractive index is raised in the material by a titanium in-diffusion

model which leads to waveguiding in the material [62]. The finite difference model solver computes the resulting optical modes and refractive indices.

The comparison of the experimental and simulated phase matched wavelength reveals a close matching at room temperature. The change in the wavelength shift increases below 150 K. This indicates either that additional refractive index perturbations occurred in the sample or that the simulation model should be improved further.

Pyroelectric charge investigations:
The electro-optic characterization of the lithium niobate modulators show that they are operate at cryogenic temperatures. The voltage and wavelength sweeps also reveal that this overall modulation map is shifted by a voltage offset, as shown in section 7.1 and 7.2. A voltage shifts in the cryogenic modulators was observed by 42 V for the directional coupler and 2.1 V for the polarization converter. The theoretical description does not introduce a voltage shift with the decrease of temperature. To that end, an additional source of charges must induce constant electric fields in the vicinity of the waveguide. Furthermore, changing distortions in the modulation map of the polarization converter are observed during the cooling process. In the publications, these perturbations and voltage shifts were attributed to the generation of pyroelectric charges in lithium niobate. To further investigate the generation of pyroelectric charges and their influence on the optical characteristics, we performed further measurements during the cooling process with lithium niobate waveguides. In section 7.6, we can measure charges generated during the cooling and warming process in the vicinity of the waveguide. Furthermore, we can correlate the occurrence of the pyroelectric charges with changes in the waveguides birefringence.

The pyroelectric charge characterization indicates a strong correlation between the charges and the optical characteristics. To measure the generated charges and changes in the birefringence in a temperature range between 300 K and 20 K, we combined to measurement techniques. We connected a current meter to electrodes on the waveguide sample which acquires changes in the charge flow. Furthermore, we mounted the lithium niobate sample in a free space cryostat and realized a Sénarmont method to acquire changes in the waveguide's birefringence. The main challenge in the optical acquisition is to maintain light coupling through the waveguide and compensate for the change in the optical throughput. Thermal contraction and expansion of the sample holder shift the light coupling during the cooling and warming process of the cryostat. To overcome this challenge, we realized the Sénarmont method which measures changes in the birefringence from two polarization outputs. In the analysis, the optical transmission can be normalized by the relative throughput in both polarizations. This normalization technique minimized the needed iterations for a throughput reoptimization during the temperature changes in the cryostat.

Auxillary opto-electronics for cryogenic photonics 3

Declaration:
The ideas and content presented in this chapter are partly taken from the following publications:

- Thiele et al. ”Opto-electronic bias of a superconducting nanowire single photon detector using a cryogenic photodiode,” in APL Photonics, vol. 7, no. 8, p. 081303, Aug. 2022. The publication is presented in section 7.3.
- Thiele et al. ”All optical operation of a superconducting photonic interface,” in arXiv:2302.12123, Feb. 2023. The publication is presented in section 7.4.

Integrated quantum photonics aims to combine several optical components on a single chip. The combined operation offers noise resilience, small device footprints and short transmission delays. To enable quantum operations with a fidelity high, performing devices are needed for quantum light sources, modulators, and single photon detectors. In recent years, SNSPDs have been established as one of the highest performing single photon detectors for quantum applications [11, 13, 14, 16]. We established cryogenic electro-optical modulation with lithium niobate in the previous chapter, to enable electro-optic modulators at the operation temperature of SNSPDs. Building on this capability we intend combine the operation of SNSPDs with opto-electronic components for application studies.

Opto-electronic components such as SNSPDs and modulators require electronic interfaces between the room temperature and cryogenic environment, as it is shown in Fig. 3.1 a). Unfortunately, typical transmission lines conduct heat and introduce electronic noise when operated between these environments. Cryostats provide the cryogenic operation temperatures for the quantum photonic circuits. Unfortunately, cryostats are limited in their ability to maintain cryogenic temperatures under a dissipated heat input by the electronic and optical circuits. The number of electronic interconnects and maximal operation power of the circuits is therefore limited.

An alternative to typical transmission lines are single mode fibers which can transmit light between the room temperature and cryogenic environment. Single mode fibers are made from low thermally conductive glass and are resilient to electronic noise. To provide the electronic operation power and read out electronic signals for cryogenic electronic circuits, we require opto-electronic converters at cryogenic temperatures.

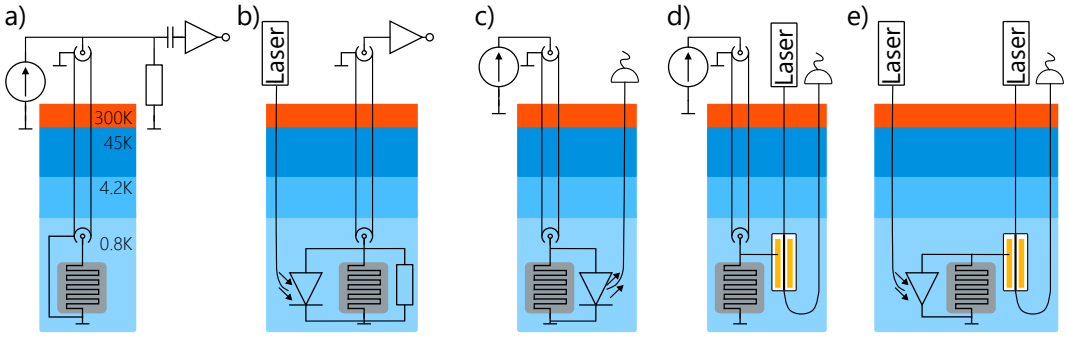

Figure 3.1: Power delivery and signal readout methods for SNSPDs in a cryostat. a) The typical operation of an SNSPD with a current source, coax line and amplifier. b) Opto-electronic bias of an SNSPD with a cryogenic photodiode. c) Optical signal readout of an SNSPD with a cryogenic laser diode. d) SNSPD readout by a cryogenic electro-optical modulator. e) All-optical operation of an SNSPD.

SNSPDs are essential devices to realize quantum photonics which require the cryogenic operation temperatures. Figure 3.1 b)-e) highlights main strategies for opto-electronic signal converters for an SNSPD operation. To provide the operation power optically, a cryogenic photodiode can establish the power conversion, as highlighted in Fig. 3.1 b)-e). The detection signal of the SNSPD could be converted to an optical signal by a laser diode or by an electro-optic modulation in a cryogenic modulator, shown in Fig 3.1 c) and d). The combined operation of both the optical input and output technique can enable an all-optical operation of an SNSPD, schematically shown in Fig 3.1 d). In this work, we realize a photodiode bias of an SNSPD in section 7.3 and realize an all-optical operation of an SNSPD in the section 7.4.

We will establish and discuss the optical operation techniques of SNSPDs. In preparation of these investigations, we discuss the state of the art of single photon detectors and in particular SNSPD in section 3.1. Furthermore, we make a case study of cryogenic transmission lines to show that single mode fibers have thermal advantage over classical transmission lines in section 3.2. In the application, we will investigate optical biasing techniques with cryogenic photodiode to operate an SNSPD, shown in Fig. 3.1 b). At first, we discuss the photodiode bias in section 3.3 and we show the operation of an SNSPD in the section 7.3. In addition, we show that photodiodes are a versatile tool to enable a pulsed operation of SNSPD for fast detection efficiency modulation in section 3.3.1. Furthermore, we provide a computational model to describe a cryogenic photodiode in section 3.3.2.

We want to achieve an all-optical operation of an SNSPD with the established techniques of a photodiode bias and the electro-optic modulation. In preparation of the all-optical techniques, we discuss the state of the art of cryogenic readout techniques in section 3.4. Furthermore, we discussion the methods required for an optical readout with an electro-optic modulator in section 3.5. The discussion reveals that large signal amplitudes are required from the SNSPD. To that end, we establish the state of the art of cryogenic amplification techniques in section 3.5. Furthermore, we establish an alternative technique

to increase the SNSPDs signal amplitude without additional amplifiers in section 3.7. Several of the discussed techniques must be combined to establish an all-optical operation of an SNSPD. In the section 7.4, we realize and discuss the all-optical operation of an SNSPD.

3.1 Single Photon Detection

Single photon detectors are the key to measure quantum states of light in quantum optics with a high fidelity. Two main techniques have been established for single photon detection namely; avalanches in photomultiplier tubes and diode structures as well as the superconductive to normal resistive transition [24]. Based on these effects, photon multiplier tubes (PMTs), avalanche photodiodes (APDs), transition edge detectors (TESs) as well as superconducting nanowire single photon detectors (SNSPDs) have been established. An ideal single photon detector achieves near unity detection efficiency, photon number resolution, a high timing resolution and minimal dark counts. Each of these properties can be almost achieved by some of the device types, but not all properties in a single device [24, 86]. Single photon detector mechanisms have been summarized and reviewed by Migdall et al. [24] as well as in review articles for APDs [87], TESs [88] and SNSPDs [15, 23, 89, 90].

In quantum photonic applications the on-chip integration is also desired to enable a scalable system architecture. Furthermore, integrated detectors promise to minimize transmission losses and time delay in comparison to separated single photon detectors. In this work, we are interested in electro-optic modulation for quantum optic applications. To that end, we are interested in the capability of single photon detectors to be integrated into photonic circuits with electro-optic modulators. In the following, the operation principles of the APDs, TESs and SNSPDs are summarized and their capabilities to be integrated into photonic platforms. This will inform our decision to choose superconducting single photon detectors in our photonic applications.

3.1.1 Single photon avalanche photodiodes

Photons are detected in photodiodes by the inner photo-effect. In this process, electron-hole pairs are generated by the impinging photon in a semiconductor material by a band transition. Classical photodiodes are designed such that these generated carriers are separated by an intrinsic field. The electric field is generated by the doping of the semiconductor material. The charge flow will generate a photo-current from an incident photon-flux. Single photon sensitivity can be achieved when a large external field is generated and applied to the diode structure. The generated electrons are accelerated in the electric field and scatter in the diodes domain. As a result additional electron-hole pairs are generated by impact ionization. The multiplied carriers generate a detectable signal for the readout electronics [24].

Avalanche photodiodes are an established platform for single photon detection for quantum applications implemented for cryptography [91], metrology [92] and computing [93]. These detectors can achieve detection efficiencies above 70% [94] and a timing jitter below 32 ps [95]. Limiting the dark count rates is challenging with these detectors due to thermal noise at higher operation temperatures and a so-called afterpulsing. Electron-hole pairs generated by thermal fluctuations or by trapping on defects can trigger the avalanche process without the presence of impinging photons. Reducing the operation temperature can reduce these effects as well.

In recent years, the development of single photon avalanche photodiodes has been established for quantum applications due to their large active area and near room temperature operation. The on-chip integration of APDs has shown to be challenging since the diode material and waveguide material should be compatible [87]. Recently, single photon sensitive avalanche photodiode have been established in an integrated platform by Zhang et al. [96] by a hybrid integration in silicon waveguides. The main advantage of this technology can be the operation near room temperature. However, in quantum applications a near unity detection efficiency and low dark count rates are desired which has not been shown by APDs, yet.

3.1.2 Superconducting detectors

Superconducting single photon detectors exploit the transition between the superconducting and resistive state when a single photon impinges on a thin film superconductor [24]. Two main superconducting detectors have been established namely, the transition edge sensor (TES) and the superconducting nanowire single photon detector (SNSPD). At first the key principles of TESs is established and afterwards the SNSPD operation principle is explained. At the end, the choice for the use of SNSPDs as our key single photon detectors is established.

Transition Edge Sensors

Transition Edge Sensors (TESs) are micro bolometers achieving single photon sensitivity. When a single photon is absorbed by the devices structure the temperature is raised in a detection structure. Most TESs read out the temperature of the detection structure by a change in a temperature dependent resistance. To achieve a high temperature sensitivity, superconductors with a strong temperature dependence at the transition edge between the superconducting and normal state are used. For the operation, the material is cooled below the critical temperature. A current is then pushed through the material. The photons heat will increase the materials resistance partially along the superconducting thermal transition. Multiple impinging photons can also increase the temperature further which relates to a photon number resolving capability. After the absorption of the photons, the substrate surrounding the detector will cool the device back to the initial state. These devices are typically operated below 100 mK to exploit the superconducting transition in

materials such as tungsten [88]. Their main advantage is the photon number resolving capabilities and their near unity detection efficiencies [88]. These detectors can also be integrated in photonic platforms such as lithium niobate [61]. Typically, the TESs resistance change is readout with superconducting quantum interference devices (SQUID) which act as current amplifiers, operated at 100mK. The operation temperature imposes strong technical challenges for large scale integrated applications.

Superconducting Nanowire Single Photon Detectors

Superconducting nanowire single photon detectors operate on the principle of the breakdown of superconductivity when a single photon impinges on a superconducting nanowire [23, 97, 98]. To do so, a nanowire is cooled below the critical temperature of the material. A current is then pushed through the superconducting nanowire biased below the critical current of the structure, as shown in Fig. 3.2. Initially, the nanowire structure has practically no resistance since it is superconducting. When a photon impinges on the nanowire, the photons energy is absorbed, heats the nanowire and the superconductivity breaks down locally. A resistive hotspot is then established across the nanowire and voltage is read out by the resistance change. The resulting hotspot reaches resistances of a few kilo-Ohm. In a typical operation of the SNSPD, an additional parallel resistor is included in the circuit to reset the SNSPDs the superconducting state. The parallel resistor has typically a resistance of about 50 Ω [23]. As a result, the bias current is redirected through the parallel resistor when a hotspot is formed since redirection of the bias current minimizes the joule heating of the nanowires hotspot. The cooling of the substrate is then larger than the joule heating of the hotspot and the nanowire is reset to the initial state. This process summarized in Fig. 3.2 from step b) to f) can be then triggered again to detect other photons.

The nanowire geometry and material are chosen such that a photon's dissipated energy is large enough to generate a hotspot across the entire width of the structure. The hotspot size is then increased further by joule heating through of the current flowing through the hotspot, as shown in Fig. 3.2 c) to e). A surplus of the generated thermal power breaks down the superconductivity in the vicinity of the hotspot. The hotspot grows in length and therefore resistance until the entire nanowire is resistive. Alternatively, the hotspot size increases until the provided electrical power is equal to the dissipated thermal energy into the substrate. The initial generated hotspot is aided in the hotspot generation by the kinetic inductance of the SNSPD structure. The sudden change in the devices resistance in the superconducting breakdown is opposed by the inductance of the SNSPD such that most of the kinetic inductance energy is dissipated through joule heating of the hotspot.

The detection mechanism and the initial generation of a hotspot across an entire nanowire can be explained by two known models. In the hotspot model, a single photon is absorbed by an electron in the superconducting nanowire. If the photons energy is larger than the energy gap of the superconductor, a so-called hot electron is created. The hot electron creates a localized perturbation by electron-electron and electron-phonon interactions in the nanowire and rising the local temperature above the critical temperature of the

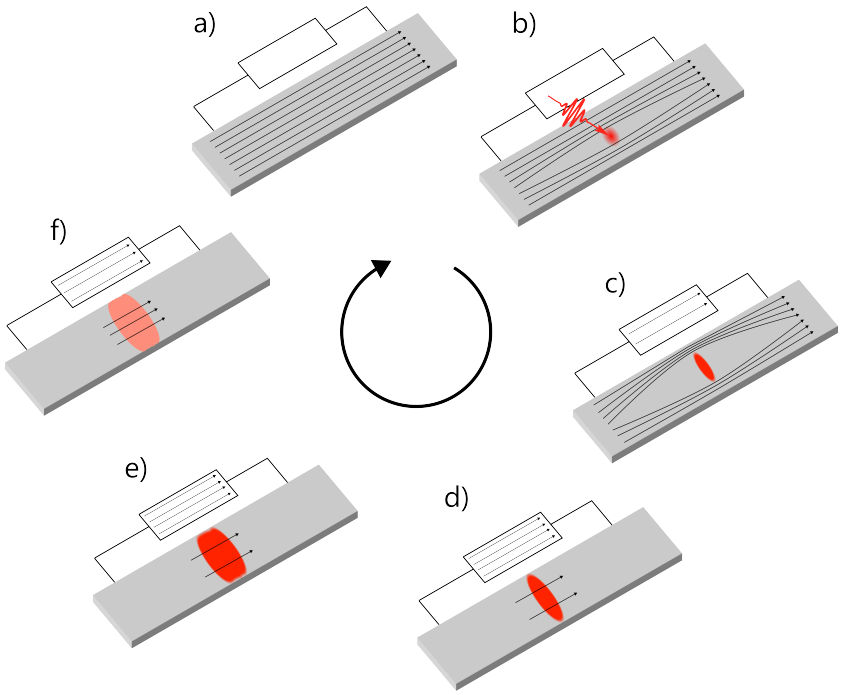

Figure 3.2: Single photon detection in SNSPDs. a) Initial state of the superconducting nanowire. b) A photon impinges creating a local superconducting breakdown. c) Initial hotspot growth by the inductance of the nanowire. d)-e) Bias current redirection through the parallel resistor and growth of the hotspot by joule heating. f) The substrate cooling is larger then the dissipated heat in the nanowire. The nanowire return to the initial superconducting state.

superconductor [97, 98]. This initial hotspot diverts the current in the nanowire such that the critical current is surpassed across the entire nanowire's width.

In the vortex-antivortex models, vortices are formed in a superconducting nanowire. Impinging photons perturb the propagation of these vortices which result in a phase transition and the local breakdown of the superconductivity in the nanowire [89].

These detection models are not necessarily competing in the description for the initial formation of the superconducting breakdown across the nanowire. A model might be more suiting depending on the detectors geometry and choice of material. In the application of this work, we mainly focus on the breakdown of the superconductor after the hotspot has been established across the nanowire. After the initial breakdown, the dynamics of the hotspot is mainly governed by the thermal coupling between the superconductor and substrate by the joule heating and thermal conduction [99–101].

3.1.3 Application and capabilities of SNSPDs

Superconducting single photon detectors are a field of active research especially for quantum photonics. These structures can achieve near unity detection efficiencies [11, 12], low timing jitter [13] and low dark count rates [14]. High performing devices like these were mainly established with free space and fiber coupled components. Similar performance regimes are sought after in integrated photonic platforms to enable scalable photonic processing. The main advantage is that a small device footprint can be achieved and the interface losses between waveguide components and the detector can be reduced. The superconducting nanowires can be deposited on waveguides in various photonic platforms. The light is then evanescently coupled to detector structure and detected [33].

High detection efficiencies are in high demand for quantum applications in order to achieve quantum operations with a high fidelity. In integrated photonic systems, detection efficiencies of above 70% have been reported on [102, 103]. A low timing jitter is to be desired in quantum optics since this will determine the width of the coincidence window to distinguish between simultaneous events. The timing jitter is the variation in timing delay of the detection signal at the signal acquisition. Reducing the coincidence window can reduce the error rates of unwanted detection events such as dark counts. Several mechanisms on the influence of the timing jitter in superconducting nanowires are known [104] such as the geometric jitter determined by the devices geometry and the intrinsic breakdown mechanism of the superconductor [89]. Integrating superconducting nanowires on photonic waveguides can even reduce the influence of the geometric timing jitter since overlap between the waveguide and SNSPD can be confined. SNSPDs can achieve low dark count rates, below one dark count per hour [14]. The low temperature environment significantly aids the reduction of dark counts by the lack of thermal photons and electronic fluctuations [24]. SNSPDs integrated in photonic structures have shown to achieve low dark count rates as well [105]. However, when realizing large scale photonic structures on chip light scattering from various optical channels have to be considered.

In addition to the integration of SNSPDs in photonic platforms, the detectors are applied in other fields to achieve a photon number resolution, to operate the SNSPD in a pulsed mode or to combine SNSPDs directly with modulators. In the following, we explore several concepts which have been realized in recent years and highlight essential capabilities for quantum optics.

Combined operation of SNSPDs and electro-optic modulators
In recent years, the development of superconducting single photon detectors has sparked the exploration of new capabilities for the development of integrated quantum circuits. A large set of photonic platforms have been established with quantum light sources and electro-optic modulators. The integration of superconducting single photon detectors is the cornerstone to realize quantum applications for several photonic circuits.

Integrated photonic platforms for quantum applications require optical modulation in applications such as configurable photonic circuits, optical readout or feed-forward modulation. To highlight previous implementations of these applications, we summarized them in the following table 3.1. In this summary, key figures of merit of integrated superconducting detectors are compared such as the detection efficiency and timing jitter. More details on the integrated cryogenic modulators are discussed in section 2.1.

Type	OCDE	Jitter FWHM [ps]	Modulator Type	On Chip	References
SiN	-	250	MEMS	all on-chip	[55]
SiN	88%	12.1	opto-mechanical	all on-chip	[54]
TFLN	46% / 24%	32/41	electro-optic	all on-chip	[58, 71]
SOI	(70%)	-	p-n junction ring resonator	off-chip detection	[51]
Ti:LN	(85%)	500	electro-optic Michelson	off-chip detection	this work (sec. 7.4)

Table 3.1: Summary of integrated SNSPDs operated in conjunction with cryogenic electro-optic modulators. The implementations highlight that SNSPDs and electro-optic modulators can be operated on a single chip. Other applications show that electro-optic modulators can be used as a optical readout method for the SNSPDs detection signal.

The highlighted studies in table 3.1 show clearly that superconducting single-photon detection and optical modulation can be performed on integrated photonic chips. These are proof-of-principle studies and the performance of the SNSPDs and modulators are likely to be improved further. Although SNSPDs have not been integrated with titanium in-diffused lithium niobate electro-optic modulators on a single chip, this is a promising platform for quantum optics. In this platform, spontaneous parametric down-conversion [26], electro-optic modulation (this work) and single photon detection [34, 35] can be achieved at cryogenic temperatures.

Detection efficiency of integrated SNSPDs
SNSPDs achieve a near unity detection efficiency via free space coupled detectors [11, 12]. These structures have been optimized to achieve a large overlap with the output of a single mode fiber. The on chip integration of single photon detectors promises to achieve high system detection efficiencies (SDE) since interface losses between the waveguides and single mode fibers are avoided. The shown examples in table 3.1 show that SDE of

above 80% can be achieved. Increasing the SDE requires the optimization of the coupling from the waveguide to the detector and a strong light absorption in the superconducting structure.

Pick and Place strategies for SNSPDs
These photonic platforms clearly show that superconducting detectors can be integrated. In addition to a monolithic integration approach, pick-and-place integration of single photon detectors are developed [106, 107]. In this technique, SNSPD are manufactured on a carrier substrate, characterized and placed on the photonic chip. At the moment, the high production yield of superconducting detectors is not guaranteed. To increase the yield of complete photonic circuits pick-and-place techniques are developed [106, 107].

Photon number resolution with SNSPDs
The mode of operation in superconducting single photon detectors is mainly a threshold detection of a photon's presence. In recent years, two concepts have been established to achieve photon number resolving capabilities namely detector multiplexing and transition edge analysis of detection signals. In the transition edge detection, the photon number resolution is extracted by a change in the electronic characteristic in detection signal induced by multi-photon events [108, 109]. To do so, the rise time and the amplitude of the detection signal are correlated to the incident photon number of light pulses. At the moment, these techniques require the acquisition of the electronic trace with an oscilloscope which will be then processed. Improvements in the post-processing could be achieved by the development of electronic circuits which discriminate the amplitude and risetime on chip for the readout.

An alternative strategy to extract the photon number is to split the photon input into multiple paths in which the single photons are then detected by the SNSPDs. These multiplexing strategies are used to achieve a pseudo photon number resolution. Several multiplexing schemes have been established with beam splitters and delay lines which are summarized by Schapeler et al. [110]. The multiplexing schemes will need to accommodate an increasing number of optical components such as beam splitters and delay lines. Integrated photonics can aid in the scalability of multiplexing SNSPDs. In additionally, arrays of SNSPDs have been developed. A multi-pixel readout approach has been expanded from a few-pixel to a kilo-pixel SNSPD array in recent years [111, 112].

Multiplexed biasing
In the typical operation of an SNSPD, every single detector is current biased and the signal is transmitted through a single coaxial cable. Increasing the number of SNSPDs on an integrated photonic network requires an increased number of interconnections on chip. A larger number of SNSPDs is demanded by the operation of multiple parallel optical channels to achieve a photon number resolution. Parallel biasing and readout techniques have been established to reduce the number of transmission lines [113]. To do so, an input line provides a bias current for multiple parallel SNSPDs. When a photon impinges on an SNSPD, a voltage pulse is generated and readout through a capacitor. Coincidences of multiple detection events are detected and can be added up for the readout in the readout line. This technique can be limited by the electronic and thermal cross talks of the

parallel channels. The parallel operation of SNSPDs is ideally suitable for the resolution of coincident photons since the voltage pulses are added in amplitude while non-synchronous detection events can be suppressed by previous events.

High temperature SNSPDs
Quantum photonic applications demand the operation of a multitude of SNSPDs on a single chip. For example to achieve photon number resolving capabilities or to introduce multiple optical channels. However, increasing the number of SNSPDs is mainly limited by ability of the cryostats to accommodate multiple SNSPDs. The main limit is the heat dissipation by the electronic interconnects. Heat is mainly dissipated in the operation of an SNSPD in a cryostat by the transmission lines for the signal and bias power. The heat dissipated by the resistive hotspot is marginal. In section 3.2 the transmitted heat of typical transmission lines is calculated and concepts to mitigate these risks are discussed. The overall heat load can also be reduced by increasing the operation temperature of the cryostat. To that end, high temperature SNSPDs are desired with the same performance to existing SNSPDs operated below 4 K. Typically, SNSPD have been realized by NbN, WSi or MoSi superconducting film with a critical temperature of up to 16 K which are then operated below 4 K [89]. Increasing the operation temperature significantly will therefore require superconducting films with high temperature superconductors. Initial results on the realization of nanowire structures such as YBCO are challenging since the YBCO thin-films are difficult to fabricate [114]. In addition, achieving single photon sensitivity can barely be achieved by a breakdown of the superconductor in this material class[114]. Recently, the realization of high temperature SNSPDs with LSCO and BSCCO superconducting films have been shown which also achieve single photon sensitivity [115, 116]. However, it remains an open field to achieve a similar performance at higher operation temperature in comparison to other established high performance SNSPDs.

Pulsed operation of SNSPDs
A majority of quantum optical process are driven in a pulsed operation in order to maintain a consistent clocking in the information processing. This enables a precise timing control in the photon manipulation and aids the post-processing in the single photon detection. SNSPDs are typically operated in a constant current mode. However, dark counts impinging before an expected detection event blind the detector which is limited by the detectors reset time. In particular in pump probe experiments, light from an initial pulse can blind a superconducting detector from consecutive signal pulses. The detection of false detection events can be minimized by the deliberate modulation of the detection efficiency. To do so, the bias current can be modulated between a high and low current to switch the detection on and off.

In the typical operation of an SNSPD the bias current is generated by a constant voltage source pushing the current through a resistor in range of 1 MΩ to achieve a bias current in the 10 µA range. The large impedance of the biasing resistor limits the current modulation speed of the SNSPD. An alternative method is to generate the current pulses by a dedicated circuit at cryogenic temperatures. This technique has been realized by Hummel et al. [117] at cryogenic temperatures. The initial results have shown that the SNSPD can be switched

to modulate the detection efficiency. The limit in the rise time of the SNSPD's switching speed is given by the inductance of the SNSPD.

An alternative method for the bias current modulation can be achieved by the photocurrent modulation with a cryogenic photodiode. Modulating the input power to a photodiode will modulate the converted current of the photodiode. In section 7.3, we will show that a photodiode can be used as a current bias for an SNSPD without a significant performance degradation. In section 3.3.1, bias current pulsing of an SNSPD with a cryogenic photodiode is shown as a direct comparison to Hummel et al. [117]. In this investigation, a rise time of 7 ns was achieved again. The modulation speed of the SNSPD was here indicated to be limited again by the inductance of the SNSPD. The modulation speed of the cryogenic photodiode was limited, as well. However, photodiodes with a high responsivity and a higher modulation bandwidth are available at cryogenic temperatures as well [118].

Pump filtering with integrated SNSPDs
Lithium niobate shows great potential as a platform for cryogenic quantum photonics. TESs and SNSPDs can be integrated in the platform, as well as electro-optic modulators and spontaneous parametric down-conversion can realized at cryogenic temperatures. Ideally, all components are integrated on a single chip to reduce interface losses. One main challenge when integrating single photon detectors with pumped single photon sources is the filtering of pump light which will introduce additional dark counts. To mitigate this risk, pump filtering must be established. Typically, a bright optical pump pulse is send into the frequency conversion structure and only a few photons are converted. Due to the ratio between the bright pump pulses and generated signal photons, a pump suppression over multiple orders of magnitude is needed. State of the art methods aim to achieve pump suppression ratios of about 100 dB [62]. In particular, a pump suppression of 95 dB has been reached with on chip filtering [119]. The pump suppression on chip is a field of active research and will need to be established also at cryogenic temperatures.

SNSPDs integrated on lithium niobate
Lithium niobate is a pyroelectric material such that pyro-electric charges are generated when the temperature of the material is changed [18, 37]. In the thermal transition from room temperature to the cryogenic operation temperature these charges can accumulate at material boundaries. When a critical charge density is reached, large electric fields can be generated and discharge through the material domain. The placement of a nanowire structure on titanium in-diffused lithium niobate waveguides has shown that these pyroelectric charges can generate discharges and violently destroy the devices structure [35]. As a result, techniques to relax the pyroelectric charges must be employed such as buffer layers or a reduction of the cooling rates(Master Thesis Felix Dreher [120]). The challenge in these techniques is to couple light from the waveguide even if a buffer layer is incorporated with the nanowire. The integration of SNSPD on thin film lithium niobate waveguides have been reported [71, 121]. However, in this platform a direct influence of the pyroelectric effect on the superconducting detectors has not been reported.

3.2 Cryogenic transmission lines

The operation of integrated circuits requires electronic interconnects for signal and power transmission. Coaxial cables are most commonly used for the signal and power transmission for integrated electronic circuits. With these transmission lines, a high signal transmission speed and a low signal attenuation can be achieved. In experimental quantum optics, these coaxial cables are commonly used for the power delivery and signal transmission for SNSPDs, electro-optic modulators and intermediate amplifiers. These three devices are indispensable building blocks to realize active integrated devices. However, the interconnects are susceptible to noise and conduct heat if these devices are connected between room temperature and cryogenic temperatures. The combined operation of SNSPDs, amplifying circuits and modulators at cryogenic temperatures is desired to reduce transmission losses and to reduce the signal delays.

A common noise source in electronic systems is the thermal noise generated by resistive components [122, 123]. In addition, the combination of multiple electronic components will introduce relative potential differences in the electronic network. As a result, leakage current and low voltage oscillations can be transmitted by the transmission lines. Coax cables are fabricated from low resistive materials such as metals and alloys like copper, aluminum, or stainless steel [122, 124]. The electronic noise is therefore transmitted to components which are susceptible to the noise, in particular bias current sensitive SNSPDs. These noise contributions can be partially filtered out in a desired frequency band [123]. However, the addition of filters will limit the bandwidth of transmitted signals. To that end, transmission lines with a high transmission bandwidth and low noise-pick up are desired.

Most transmission lines, fabricated from metals, are also good thermal conductors which is described by the Wiedemann-Franz-law [125]. The thermal load must be therefore considered when transmitting power and signals between room temperature and cryogenic temperatures. Cryostats are limited in their capability to maintain their target temperature under a given dissipated thermal energy [122, 123]. This associated cooling power is limited by the number of transmission lines and the cryogenic devices which dissipate heat during their operation.

The thermal load of a transmission line can be calculated based on their material properties and geometry. Cryostat are typically designed to accommodate multiple stages with a higher cooling power at higher temperature stages, as it can be see in Fig. 3.1 a). To improve the cooling performance, thermal anchoring of transmission lines is established at intermediate stages. As a result, the conducted heat is dissipated on these stages which will reduce the thermal load for consecutive colder stages in the cryostat. The operation temperature of the cold stages are fixed by the cryostat design. For example, one of the cryostats used in this work has a cooling power of 3 W at the 45 K stage and 0.16 W at the 4 K stage [126]. In the following, we estimate the dissipated heat by transmission lines onto the various cold stages of an exemplary cryostat used during this work (Photonspot [126]).

In cryogenic applications SMA-cables are typically used, made with a copper or stainless-steel shielding [124]. The conducted heat P_{heat} can be calculated with the cross section A from the materials, the length of the conductors L, the temperature differences between T_1 and T_2 as well as the conductivity of the materials λ [122]:

$$P_{heat} = A/L \int_{T_1}^{T_2} \lambda(T) dT \tag{3.1}$$

We calculated the power dissipation between room temperature and the 45 K stage with a 20 cm cable, as well as from 4 K to 40 K with a 30 cm cable, as highlighted in Fig, 3.1. These are the cable lengths used in the exemplary cryostat which is also used in this work;

Type	45 K-stage	4 K-stage
SMA-cable (copper)	180 mW	41 mW
SMA-cable (stainless)	1.5 mW	30 µW
SMF (glass)	24 µW	0.9 µW

Table 3.2 shows that a considerable thermal power is dissipated onto the cold stages of the cryostat. It is therefore evident that the number of used coaxial lines is limited in a cryostat. In this configuration about 16 copper transmission lines can be accommodated. However, scaling photonic circuits up to a few hundred optical channels with modulators and detectors will become unachievable. If these photonics circuits with a multiple opto-electronic and electro-optic components are needed, transmission lines with a lower thermal conductivity or cryostats with an increased cooling power are desired.

Single mode fibers fabricated from glass have inherently a much lower thermal conductivity than classical coaxial cables, as it can be seen in table 3.2. The reduced cross-section and the low thermal conductivity of glass limits the heat flux in the cryostat. In addition, glass fibers do not transmit any electrical noise due to their high electrical resistance. Single mode fibers are therefore the ideal candidate for the transmission of power and signals between room temperature and cryogenic temperatures. In this configuration, significantly more single mode fibers can be installed without exceeding the thermal limit of the cryostat. Single mode fibers are commercially available and have been proven to be operated at cryogenic temperatures. However, power converters are needed to convert between an electrical and optical power. Cryogenic photodiodes are and ideal candidate for the optical-to-electrical power conversion which is highlighted in Fig. 3.1 b) for an SNSPD. In this work, the optical bias of an SNSPD is established in section 3.3 and 7.3. Exploring this optical signal transmission concept further will require an optical readout of the SNSPDs detection signal. The optical readout of electronic signal can be realized by electro-optic components such as cryogenic lasers and modulators which will be discussed in section 3.4. These three methods, highlighted in Fig 3.1 c)-d), convert only the input or the output to the optical domain. However, an advantage in the thermal or noise performance cannot be expected if transmission lines are still needed for the bias or signal transmission, as shown

in Fig 3.1 b)-d). To that end, the optical bias and signal transmission is combined as shown in Fig. 3.1 e) and experimentally shown in section 7.4.

3.3 Optical power delivery with cryogenic photodiodes

In order to use single mode fibers for a signal transmission with cryogenic electronics, optical input signals must be converted from an optical to an electronic domain. Photodiodes are an ideal candidate for the energy transformation. Light impinging onto the photodiode will generate carriers by the inner photo-effect. The generated current can then be used as a bias current for electronic circuits. Modulating the transmitted power to the photodiode will modulate the electronic output to switched off the photocurrent deliberately.

The technique of the optical-to-electrical power and signal conversion has been used before at cryogenic temperatures for the operation superconducting circuits. Morse et al. [28], Sobolewski et al. [127], Karlsen et al. [128], and Suzuki [129] et al. developed cryogenic photodiode for the current pulsing to operate Josephson junction. Alongside this application, cryogenic photodiodes have been investigated by Shi et al. [129]. Photodiodes fabricated from InP-InGaAs are most promising since the InP aids the generation of free carriers to generate the photocurrent [118, 129, 130]. Expanding on the optical biasing concept, Lecocq et al. [131] established the operation of photodiode arrays and optical multiplexing to generate multiple optical signal inputs with only one single mode fiber.

The key for an energy efficient power transformation is to use a photodiode material with a high responsivity at cryogenic temperatures. In the preparation of opto-electronic bias with a cryogenic photodiode, we tested several off-the-shelf photodiodes fabricated from InGaAs and observed no responsivity at cryogenic temperatures. In contrast, off-the-shelf photodiode based on InP-InGaAs showed a high responsivity. This material achieves a responsivity of 0.66 A/W with input light at 1530 nm. Photodiodes fabricated from Si or InGaAs can undergo carrier freeze-out and achieve only a limited responsivity at cryogenic temperatures. As a result, the density of free carriers needed for the current generation is strongly reduced. In addition, the bandgap of the photodiodes increases, described by the empirical Varshni rule [132]. As a result, the maximal operation wavelength of the photodiode is decreased.

The high responsivity InP-InGaAs is well suited for cryogenic temperature power conversion to minimize the power dissipation. In section 7.3 the characterizations are shown to generate the bias current for an SNSPD. We characterized the wavelength dependent responsivity and linearity of the responsivity by multiple orders of input power. In our characterization it is highlighted that the dark current of the photodiode is strongly reduced to below 10 pA at cryogenic temperatures in comparison to room temperature at 1 µA. This shows that the photodiode can be used to decouple electronic components galvanically in combination with single mode fibers. A similar study has shown that a cryogenic photodiode can be used as a shot noise limited current source [131]. The opto-electronic bias of SNSPD in section 7.3 shows clearly that a photodiode can provide the bias current to an

SNSPD without a significant performance degradation. In the experiments, additional dark counts are generated from scattered light to the photodiode. However, with additional shielding this influence can be strongly reduced.

The opto-electronic bias of an SNSPD in section 7.3 shows mainly the capabilities as a current source. In this configuration, the photodiodes electrical load is between zero and 50 Ω. However, in the all-optical operation of an SNSPD the photodiode must provide an electrical power with a larger electrical load. In section 7.4, we additionally characterize the capabilities of the cryogenic photodiode for power delivery. This investigation shows that an electrical power of up to 1 µW can be generated with an input power of about 6 µW at 1530 nm, as well as an output voltage of above 500 mV. The high responsivity and power conversion capabilities of the photodiode shows clearly that optical biasing techniques are well suited for a low power power transmission for SNSPDs.

3.3.1 Pulsed operation of an SNSPD with a cryogenic photodiode

Superconducting nanowire single photon have proven to be one of the highest performing detectors for single photons. The majority of applications have shown a constant current bias for SNSPDs.

The operation of cryogenic photodiodes as current sources is established in section 7.3. In this operation the high performance properties of SNSPDs are exploited while achieving a low power method to provide the operation power with a constant bias. As a result, the detector is always sensitive until a detection event is triggered. The reset time of the detector limits the sensitivity for a secondary photon impinging on the nanowire. In pump probe experiments or LIDAR applications bright input pulses are generated which generate a response with a few photons. In the following, we want to explore the pulsing capabilities of SNSPDs with cryogenic photodiodes.

Ideally, detectors are modulated to be insensitive to the bright input pulse and sensitive again when signal light is expected. Initial results have shown the detection efficiency modulation of an SNSPD by modulating the bias current. In these studies a continuous wave modulation was applied as a bias current [133–136]. In addition, slow current modulations have been implemented with room temperature bias current modulation [137–139]. However, in most applications a fast transition between the on- and off-state is desired to minimize the minimal delay time between the input and signal pulses. The key to achieve this is to generate fast bias current modulations of the SNSPDs which modulates the detection efficiency.

In the typical operations of an SNSPD a current is passed through a large resistor such that a bias current in the 1-100 µA range is generated [23]. This technique cannot enable fast current modulations since the impedance of the bias resistor, transmission lines and superconducting nanowire are unmatched. In order to overcome this challenge Hummel et al. [117] has shown that current pulses can be generated by integrated electronics at cryogenic temperatures in the cryostat for an SNSPD bias. These initial results have

shown that the detection efficiency can be modulated with a rise time of 2.4 ns. The main limit of this operation is the inductance of the SNSPD. The nanowires inductance inhibits fast changes of the bias current which is needed to generate single photon signals in the detection mechanism.

The results of the integrated current source have shown that fast detection efficiency modulations are possible. In the opto-electronic bias of an SNSPD in section 7.3 we have also shown that a photodiode can be used as an integrated current source at cryogenic temperatures. The investigations showed that the photocurrent bias performance as well as a typical bias of an SNSPD. In addition, in section 7.4 we have shown that modulating of the photocurrent can be used to switch off a latched SNSPD in a pulsed operation. Building on these results, in the following we will show that pulsing the input power to a photodiode can be also used for fast modulation of an SNSPD.

The pulsed operation of the SNPSD is achieved by modulating the input power to the photodiode with a laser. The laser transmits light through a single mode fiber which then illuminates the photodiode placed at the 1 K stage in a cryostat. The generated photocurrent is then transmitted through a coaxial cable to an SNSPD. On the PCB-board of the photodiode, a parallel 50 Ω is included to reset the SNSPD after a detection event. The generated detection signals are then transmitted through a coaxial cable to a room temperature amplifier and then acquired by a time tagger. In this experiment, a low inductance SNSPD, of about 260 nH, is chosen such that fast modulation of the bias current is possible. The SNSPD is illuminated by a single mode fiber for flood illumination. This detector is not designed with an alignment structure for the single mode fiber such that the single mode fiber be placed in the optimal position to extract a high detection efficiency.

As a comparison, we have chosen the same SNSPD as in the paper from Hummel et al. [117] to compare the modulation speed in the detection efficiency, as shown in Fig. 3.3 a). In order to extract the time dependent count rates, we generate a rectangular on-off input pulse with a 45% duty cycle and a 5 MHz repetition rate for the laser. The resulting optical modulation is shown in Fig. 3.3 b) which is transmitted to the cryogenic photodiode. Figure 3.3 c) shows an acquired trace when no single photon signal is generated within a duty cycle. When the current is changed from the on-to-off state at 10 ns an inductance pulse is generated. The inductance pulse is inverted when the bias current is switched from on to off.

A trace of a single photon event is shown in Fig. 3.3 c), as well. The reset time and the length of the inductance pulse length is approximately 7 ns. In a direct comparison, a larger amplitude signal is generated by the single photon signal such that the inductance pulses and single photon peaks can be discriminated by the amplitude.

As a next step, we extracted the rise time of the detection efficiency. In this operation, the SNSPD is flood illuminated by an 1550 nm input light source and the detection events are recorded by the time tagger. The recorded events are presented as histograms depending on the time of arrival in relation to the optical modulation, in Fig. 3.3 d). This measurement

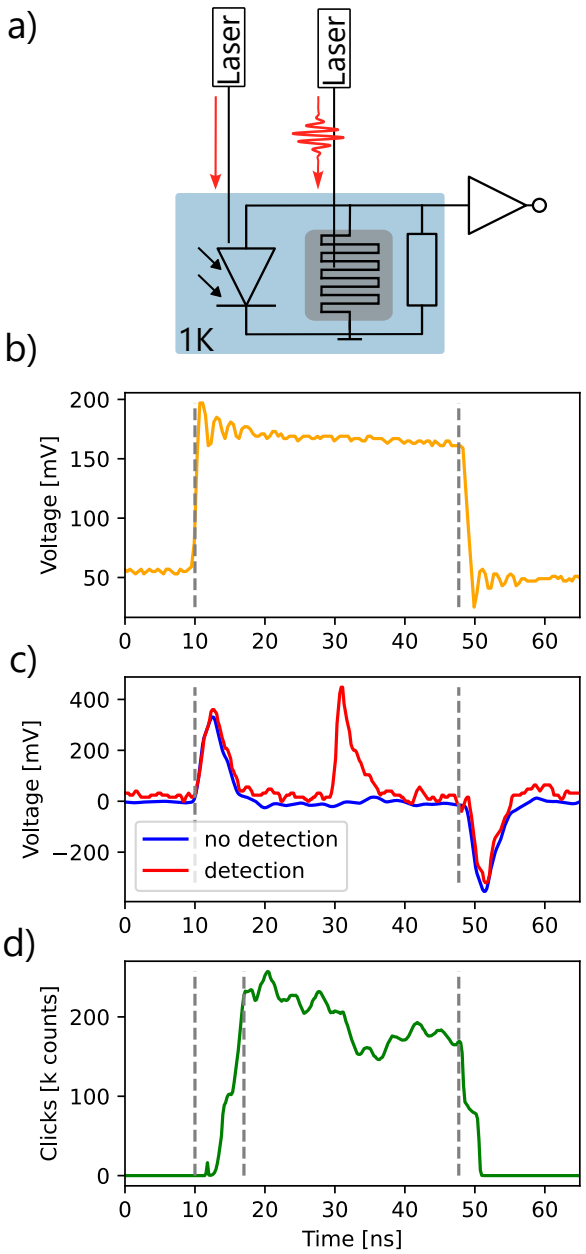

Figure 3.3: Pulsed bias current operation of an SNSPD by a photodiode. a) Setup for the optical pulsing of the photodiode and SNSPD. b) Acquired optical pulse by the photodiode. c) Oscilloscope traces of a repetition cycle. (Blue: without a detection event) (Red: with a detection event at 30 ns) d) Histogram of detection events synchronized to the repetition of the bias modulation.

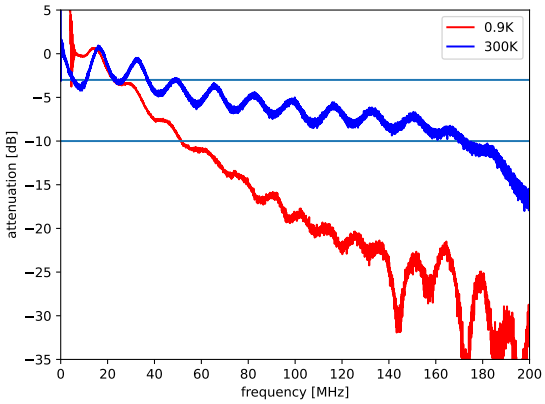

Figure 3.4: Bandwidth of the InP-InGaAs photodiode. An optical modulation of a laser source is transmitted onto the photodiode at wavelength of 1530 nm. The normalized amplitude of the electronic response signal is shown.

discriminated inductance pulses and single photon signals by their amplitude. A total integration time of 5 s was recorded in this measurement.

This measurement show clearly that count rate can be modulated by modulating the bias power of the photodiode. It is important to highlight that no light is detected when the bias power is switched off. In this experiment, the input to the photodiode was modulated with a 1 ns risetime. In comparison a 90%-risetime of 7 ns in the count rate was achieved. The risetime of the photodiode bias is limited by the bandwidth of the photodiode and the inductance of the SNSPD. As a direct comparison, a 90% risetime of about 2.4 ns was achieved by Hummel et al. [117]. We can therefore expect that the count-rate risetime is mainly limited by the bandwidth of the photodiode. To test this, we recorded the bandwidth of the photodiode at room temperature and cryogenic temperatures. Fig. 3.4 shows that a bandwidth of about 45 MHz can be achieved at room temperature which decreases to about 20 MHz. In the future, higher rise times can be achieved by using a different InP-InGaAs photodiode with a higher bandwidth. Bardalen et al. [118] has shown cryogenic photodiode with a high modulation bandwidth and responsivity are available which can enable faster gating.

In summary, we have shown that a fast opto-electronic bias of an SNSPD is possible. To do so, we generated current pulses with a cryogenic photodiode and modulated the bias current to an SNSPD. The recorded risetime is around 7 ns which is limited by the bandwidth of the cryogenic photodiodes. The risetime is comparable with a current bias with an integrated current source realized by Hummel et al. [117]. The main advantage of the photodiode bias in comparison to the integrated current source is the reduction in the heat load.

3.3.2 SPICE model of a cryogenic photodiode

Cryogenic photodiodes are used in this work for the biasing of SNSPDs. Alongside the application, the cryogenic photodiode was mainly characterized in the constant current operation in the opto-electronic bias of the SNSPD in section 7.3 and the all-optical operation of an SNSPD in section 7.4. In the future, other electrical components might be added in the electrical network such as amplifiers or logical gates for further signal processing. Planning and designing electrical circuits for new applications will require a simulation model of the cryogenic model. An ideal model of semiconductor could be adapted if common figures of merit are known such as the diodes shunt resistance, parallel resistance or threshold voltage. However, the extraction of these parameters are not trivial and real diodes vary slightly from the ideal diode model. To that end, we will introduce an adaptation of a non-ideal photodiode for the description of the cryogenic photodiode. To use this model conveniently with other electrical circuit models, we implement the model in the simulation framework SPICE [140].

A photodiode can be described by an ideal photodiode model and a current source I_{photon} for the generated photon input. The output current I_{out} of the photodiode is therefore the sum of the photon current and the scaled saturation current of the diode I_{sat},

$$I_{out} = I_{sat}\left(e^{qV_a/k_bT} - 1\right) - I_{photon} \tag{3.2}$$

Applying a voltage V_a to the diode will change the output current scaled by the thermal energy k_bT of the diode structure and the generated carriers q.

In the ideal photodiode model, only the dark saturation current I_{sat} is a free parameter. In recent years, various models have been created to describe photodiodes and photovoltaic cells. To do so, the photodiode is represented in a lumped model, which is presented in Fig. 3.5 a). The output current I_{out} can then be described with a semiconductor diode with the non-ideality factor a, a shunt resistance R_{shunt}, a series resistance R_{series} and the thermal voltage V_T [141, 142]:

$$I_{out} = I_{photon} - I_{sat}\left[exp\left(\frac{V_a + I_{series}}{aV_T}\right) - 1\right] - \frac{V_a + I_{out}R_{series}}{R_{shunt}}. \tag{3.3}$$

This model requires 5 parameters for to fit the IV-characteristics to the an real photodiode. However, obtaining the shunt resistance or series resistance is not trivial. An alternative approach is to extract characteristic parameters of the real photodiode and adjust the model accordingly. To do so, the open circuit voltage V_{oc} and shunted current I_{sc} can be easily obtained under a given illumination power. In addition, a IV-curve can be easily obtained by changing the photodiodes load resistance under the same illumination power, as it can be seen in Fig. 3.5 b). In this IV-curve the maximal output power point can be extracted with a the given current I_{mpp} and voltage V_{mpp}. The non-ideal photodiode models can

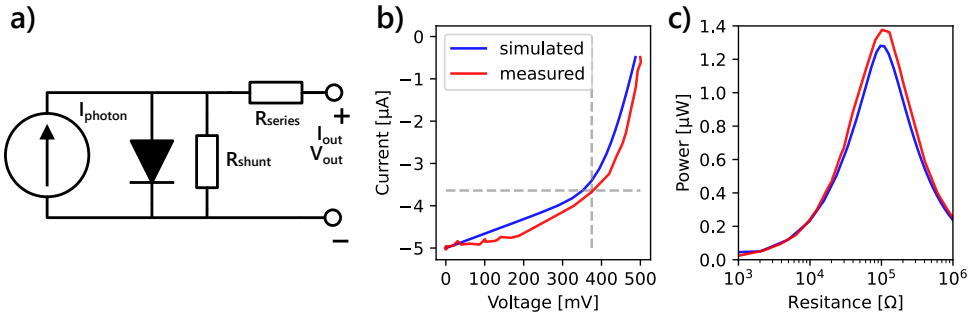

Figure 3.5: a) Lumped element model to describe a real photodiode. b) IV-curve of the measured cryogenic photodiode and the simulated photodiode under a input power of 9 µW and wavelength of 1550 nm. c) Output power of the cryogenic photodiode with a changing electrical load resistance under the same input power and wavelength.

then relate back to the series and shunt resistances ([143] equation 12 and 13):

$$R_{shunt} = \frac{V_{oc} - V_{mpp}}{2I_{mpp}} \tag{3.4}$$

$$R_{series} = \frac{V_{mpp}}{I_{sc} - I_{mpp}} \tag{3.5}$$

Furthermore, the output current I_{out} and the photon current I_{photon} can be computed [142]:

$$V_T = \frac{k_B T}{e} \tag{3.6}$$

$$I_{photon} = I_{sc} \frac{R_{shunt} + R_{series}}{R_{shunt}} \tag{3.7}$$

$$I_{out} = \frac{(R_{shunt} + R_{series})\, I_{sc} - V_{oc}}{R_{shunt} exp\left(\frac{V_{oc}}{aV_T}\right)} \tag{3.8}$$

This model was implemented as a SPICE subcircuit and can be seen the appendix A.1. Furthermore, the model is applied to simulate the dynamics of the cryogenic photodiode placed at cryogenic temperatures. To do so, we acquired IV-curves at cryogenic temperatures at a wavelength of 1530 nm, as shown in Fig. 3.5 b). The maximum power point is highlighted with the dashed lines in Fig. 3.5 b) at 3.64 µA and 375 mV at an input power of 9 µW. The derived model closely matches the IV-curve of the measured data, as shown in Fig. 3.5 b). In addition in Fig. 3.5 c), the output power of the photodiode is derived from the IV-curve. The main parameters such as shunt resistance and the series resistance are computed in this method. The ideality-factor a can be adjusted for a curve fit and should be in the range of 1 to 1.5 [142].

In the all-optical operation of an SNSPD the photodiode was used to provide the operation

power for the latching SNSPDs, in section 7.4. In this mode of operation, the electrical output of the photodiode was dissipated in the SNSPD such that the resistance increased. In addition, the output power changed with the change of the resistance. The electronic dynamics of an SNSPD can also be computed with a SPICE model [100, 101]. The combination of the SNSPD and photodiode model can be used to optimize the output voltage and risetime in the combined operation.

3.4 Signal readout with opto-electronics

In photonic networks, electronic signals are generated mainly by detectors such as single photon detectors. To avoid the use of electrical transmission lines, single mode fibers guiding optical signals can be used. Similar to the established optical power delivery for superconducting detectors an electronic-to-optical signal conversion is desired. Two promising methods have been established to convert electronic signals from the electronic to the optical domain at cryogenic temperatures, namely by cryogenic lasers diodes and electro-optic modulators. In quantum optics, the readout of single photon detectors such as SNSPDs are of high interest to achieve low operation power interconnects. However, the output signal of single photon detectors such as SNSPDs in the few mV-range. The electrical-to-optical signal converters will need to be sensitive for this change to generate a strong readout signal.

Laser readout
Lasers operated at cryogenic temperatures can be modulated by an electrical signal, as it is shown in Fig. 3.1 b). To read out a detection signal of a superconducting detector, the output signal of the SNSPD will modulate the bias current to the laser. The optical modulation will then be detected at room temperature. Morse et al. [28], Lu et al. [144] and Fu et al. [145] have shown that cryogenic lasers can be used as an optical interconnect between room temperature and cryogenic temperature. In these applications a Josephson's junctions was read out. However, additional transmission lines for the laser diode bias must be established at cryogenic temperatures which are susceptible to electronic noise. In addition, a large portion of the generated power is needed to generate a signal above the lasing threshold. A clear improvement of the low temperature power dissipation with the lasers diodes has not not been shown.

Electro-optic readout
Alternatively, electro-optic modulators placed a cryogenic temperatures can convert an electrical to an optical signal. To achieve this, light is guided through a cryogenic electro-optic modulator and an input voltage modulates the transmitted light. The modulated light then transmitted to room temperature for the signal acquisition, as it is shown in Fig. 3.1 d). In this technique, the electro-optic modulator operates as an auxiliary signal converter.

Initial implementations of an electro-optic signal readout has been shown for superconducting electronic circuits by Morse [28] et al. and by Sahu et al.[146]. Additionally, Youssefi et al [59] realized a similar electro-optic readout with intermediate amplifiers to achieve stronger optical signal. Furthermore, the readout of an SNSPD with electro-optic modulators has been established by de Cea et al. [51] and by Thiele et al. with an intermediate amplifier [147]. The key for the optical readout is to minimize the dissipated optical power at cryogenic temperatures. In addition, the modulation bandwidth should be large enough to convert the electrical signals.

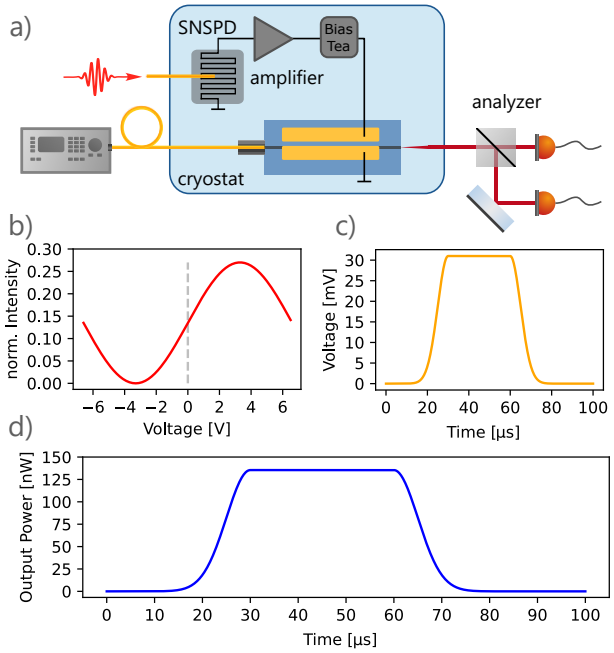

Figure 3.6: Conceptual overview of the optical readout of an SNSPD. The expected optical response is calculated from the exemplary figures of merit in section 7.4. a) Setup of the optical readout of an SNSPD with an electro-optic modulator. b) Modulation response of the electro-optic modulator with a V_π of 6.6 V. The modulation map is normalized to the input power, assuming a fiber-to-fiber coupling efficiency of approximately 27%. b) Detection signal of the SNSPD after amplification. c) Change in the output intensity induced by the detection signal. The response is calculated for a offset voltage of 0 V at the bias tea and an input power to the modulator of 68 µV

3.5 Optical readout amplitude estimation

In the following we investigate several figures of merit which need to be considered for the task of optical readout at cryogenic temperatures. Our objective is to generate optical signals with a large signal to noise ratio from a given detection signal of the SNSPD. As an example, we discuss the readout of an SNSPD with a titanium in-diffused lithium niobate modulator which is used in the publication of the all-optical readout of an SNSPD in section 7.4. The figure 3.6 conceptualizes the main components required for an optical readout. Furthermore, detection pulse is of the SNSPD is sent onto the electro-optic modulator such that the optical modulation can be extracted in the figures 3.6 b) to d).

Waveguide coupling
A high coupling efficiency between single mode fibers and the waveguides of the electro-optic modulator is needed. Unmatched optical modes will result mainly in light scattering and therefore heat dissipation in the cryostat. In addition, single photon sensitive detectors will experience an increase in the dark count rates. The lithium niobate waveguides, used in this work, can achieve a mode matching of more than 88% (−0.6 dB) for both transmitted

polarizations with standard single mode fibers with endfacet coupling techniques [62]. In the optical coupling, reflection losses should also be considered if refractive index of the modulators waveguide and the single mode fiber are unmatched. A reflection losses of about 4% (−0.13 dB) is given between the lithium niobate waveguide and single mode fiber. Additionally, we can expect a fiber-to-fiber transmission efficiency of approximately 80%(−0.2 dB) to a single waveguide device with a length of 20 mm. In this work, we operated our lithium niobate waveguides with fiber coupled optical access and achieve fiber-to-fiber efficiencies of around 55% (−2.6 dB) at room temperature and 27% (−5.7 dB) at cryogenic temperatures as shown in section 7.4. Furthermore, the electro-optic modulators are operated at cryogenic temperatures such that additional strain shifts the fiber coupling towards the waveguide. In section 7.1, we can achieve fiber-to-fiber efficiencies are cryogenic temperatures of approximately 43% (−3.7 dB).

Linear losses
The linear losses of the electro-optic waveguides must be considered. The electro-optic modulators are typically fabricated with waveguides for the light confinement. Scattering at material defects of the waveguide's sidewalls the main contributor to transmission losses. The electrodes placed on the top of the waveguide do not introduce significant losses in the modulators since a SiO_2-buffer layer is deposited between the waveguide and the metal electrode. In titanium-indiffused lithium niobate waveguides of this work the waveguide losses are in the range of 0.1dB/cm, as shown in section 7.1, 7.2 and 7.4. The main method to determine the losses of the waveguides used in this work is the so called Fabry-Pérot method [148]. In this method, the losses are related to the contrast of the intensity pattern generated by interference fringes in the waveguide.

Modulation voltage
The modulation strength of the electro-optic modulators is one of the key metrics. Ideal electro-optic modulators achieve a large optical modulation with a small electronic input signal. In section 2.1 and table 2.1 are the electro-optic modulators summarized for cryogenic modulation. The electro-optic modulator in this example requires a modulation voltage of 6.6 V for a complete change in the output amplitude, see fig 3.6 b). The key objective is to use an optical modulation technique which will not use additional amplifiers to reduce the thermal heat load of the system. In addition, the signal-to-noise ratio should not be decreased by the conversion from an electrical-to-optical signal. The amplification techniques at cryogenic temperatures are discussed in section 3.6.

Offset voltage
The input signal induces the optical modulation in the modulator. The strongest response is achieved if the modulation is a the highest slope of the optical response, see 3.6 b). To maximize the optical response, the offset voltage can be shifted by an additional bias tea. However, the operation of the bias tea could also induce an additional heatload when operated cryogenically. To avoid this in the all-optical operation of an SNSPD, we changed the operation wavelength of the modulator to maximize the optical response. Changing the operation wavelength in the Mach-Zehnder interferometer changes the phase at the 0 V point.

Signal amplitude
In the all optical SNSPD operation, a 31 mV output signal will be generated as a electronic readout signal of the SNSPD. This signal will be converted to a 136 nW optical modulation amplitude from an input power of 68 µW, which can be seen in Fig. 3.6 d). In this optical readout scheme, an optical input power must be chosen such that the readout photodiode can detect the intensity changes after the modulation. The used readout photodiode is this configuration an SFP-module which has integrated amplifiers. These photodiodes were able to detect readout signals with an amplitude of approximately 136 nW. The acquisition photodiodes high sensitivity enables a low operation power of the cryogenic electro-optic modulator.

Electronic bandwidth
The detection signal of the SNSPDs have a signal rise time of below 1 ns, see section 7.3. In order to convert these signals, the bandwidth of the modulators should be large enough. The lithium niobate modulators in this work achieve a band width of approximately 0.5 GHz to 1 GHz, given by the electrode structure [45]. Lithium niobate modulators with this electrode geometry are mainly limited by capacitive loading time of the electrodes RC-time. The bandwidth can therefore be increased by the reduction of the capacitance. When operating the modulators in a travelling wave configuration the bandwidth of the electro-optic modulation is limited by the mismatch between the electrode's propagation speed and the waveguides propagation speed. Dispersion engineering of the electrodes to the waveguides have shown in thin film lithium niobate significantly higher modulation bandwidths [46]. The presented risetime in figure 3.6 c) and d) is in the order of 10 µs and matches risetime of the all-optical operation of an SNSPD in section 7.4. In this scheme the risetime of the detection signal was reduced to increase the output amplitude.

In summary, titanium in-diffused lithium niobate modulators are an ideal device for the cryogenic signal readout. A high fiber-to-fiber transmission as well as a low modulation voltage can be achieved. In this work, we use this platform to realize an all-optical operation of an SNSPD without additional amplifiers only from the single photon output signal, as discussed in section 7.4. In the implementation a 31 mV output signal will be generated as a electronic readout signal. This signal will be converted to a 136 nW optical modulation converted from an input power of 68 µW which was detectable by our photodiodes. Other types of electro-optic modulators can achieve a stronger optical modulation. However, the used lithium niobate modulators balance out low transmission and coupling losses with a comparatively high optical modulation voltage.

3.6 Cryogenic Signal Amplification

A main objective of this work is the combined operation of the single photon detector and electro-optic modulators. The direct comparison of the typical output voltages of an SNSPD and the modulation voltage of an electro-optic modulator reveals a large discrepancy. Driving the electro-optic modulator with an SNSPD detection will result in a small optical

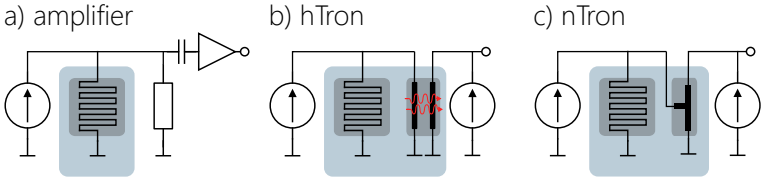

Figure 3.7: Signal amplification methods for detector signals. a) Typical operation of an SNSPD with an amplifier. b) hTron amplifier with an SNSPD (heat based triggering). c) nTron amplifier with an SNSPD (current based triggering).

modulation which is barely detectable. Typical SNSPDs generate an output voltage of about 1 mV and a cryogenic electro-optic modulator a typical modulation voltage of about 6 V. In order to increase the signal to noise ratio in the optical channel, additional electronic amplifiers are needed, as shown in Fig. 3.7. To do so, the detection signal is amplified such that a larger voltage is generated which is used for the electro-optic modulation.

Ideally the amplifier maintains a fast rise time of the signal to reduce the signal delay. Additionally, the amplifiers add no additional noise in the output to achieve a large signal-to-noise ratio. At room temperature, a large variety of electronic amplifiers are available based on mature semiconductor platforms. However, when using room temperature amplifiers, the detection signal has to be transmitted between the cryogenic and room temperature environment. In the signal transition, additional noise and signal delay is added. To that end, the operation of cryogenic amplifiers is advantageous to reduce signal delay and to improve the noise performance. A mayor technical challenge is to realize cryogenic amplifiers with a low heat dissipation, to maintain a low operation temperature.

In recent years, cryogenic amplifiers have been developed with semiconductor integrated circuits. These type of amplifiers are based on integrated circuit components on a single semiconductor dye with a high performance at room temperature. When adapting these circuits for cryogenic applications, the semiconductor devices can undergo carrier freeze out or other shifts in the material properties. As a result, the device performance can be drastically reduced. Integrated semiconductor have been optimized for the cryogenic amplification based on HEMT [149–151] or BiCMOS [152–154]. The reported heat load of these devices are in range of 300 µW to a few mW. In addition, these amplifiers achieved an amplification in range of 20 to 30 dB. The operation of such a semiconductor amplifier could amplify the SNSPD signals into the volt range which is adequate for the operation of electro-optic modulators.

An alternative approach to signal amplification can be achieved with superconducting thin-film structures. One of the first known superconducting amplifiers are SQUID amplifiers. These devices can achieve a current amplification in Josephson Junctions [155]. Initial operation of these amplifiers in combination with SNSPDs have been shown [156]. However, SQUIDs require lower operation temperatures then SNSPDs. As a result, more stringent technical requirements have to be realized in cryostat which can limit the scalability of the system.

Amplification in superconductive structures has also been investigated by the breakdown in the superconductivity. In these structures, a superconducting thin film is biased below the critical current and the superconductivity breakdown is deliberately triggered. To trigger the breakdown, either a micro-heater heats the superconductor or an additional current is injected into the main structure which surpasses the critical current threshold. The change in the devices resistance is used to generate a strong voltage pulse. Heater based systems, known as hTrons and shown in Fig. 3.7 b), have been established with thin film metal layers deposited on superconducting nanowires [157–159]. Current based amplifiers, known as nTrons and shown in Fig. 3.7 c), have been estblished in recent years [160–162] and can even realize electronic logical gates [160, 163]. As a first proof of principle study the logic operations of nTrons were combined as a counter for SNSPD detection events [164]. The main advantage of the hTrons and nTrons as amplifiers is that they rely on the same superconducting thin films as SNSPDs and can be operated at the same temperature. Superconductors are operated at cryogenic temperatures which are inherently in a low noise environment. Furthermore, their low resistivity nature can reduce the operation power.

The combined operation of SNSPDs and electro-optic modulators will also require matching of the electronic impedance of their electronic characteristics. The SNSPDs impedance is mainly determined by the shunt resistance. Furthermore, the electro-optic modulators impedance is mainly determined by the electronic layout of the electrode. The intermediate amplifier should be designed such in- and output impedances are matched towards the SNSPD and modulator. A good impedance matching will reduce refraction losses and therefore reduce noise and power dissipation in the system.

3.7 SNSPD amplitude increase by the superconducting transition

The operation of electro-optic modulator with a typical SNSPD signal cannot generate a sufficient modulation which can be readout at room temperature. In the previous section 3.6 several amplifiers types are discussed. However, it becomes apparent that these amplifiers require additional electrical connections and can dissipate heat at cryogenic temperatures. Ideally, no amplifiers are required in the interface between the SNSPD and modulator. To achieve this, the output signal must be increased in the detection mechanism in the SNSPD. In the following, we discuss how the SNSPDs signal generation method can be altered to generate an increased output signal. In this technique, the superconductive breakdown after the detection is explored, inspired by superconducting amplifiers such hTrons. This technique favors a strong output amplitude and sacrifices a fast signal risetime.

The core principle of the superconducting breakdown is used in the single photon detection in SNSPDs. If a strong output signal after a single photon detection is desired, a close look at the breakdown mechanism reveals high potentials. Initially, the SNSPD has no resistance and no output voltage is created. After the formation of the initial resistive

hotspot the resistance rises to a few kΩ [100, 101]. Once a hotspot is created, the bias current is pushed through the nanowire and the hotspot grows in size, because the joule heating of the nanowire heats the nanowire in the vicinity of the hotspot. Expanding the hotspot such that the entire nanowire becomes resistive could generate resistances of a few MΩ. These resistances can be generated by omitting the parallel shunt resistor of in the typical operation of an SNSPD. The initial hotspot is increased by continuously pushing a bias current through the structure. As a result, an increased output signal in comparison to the typical SNSPD operation is generated.

The nanowire will remain in the normal resistivity state indefinitely since the bias current pushed through the nanowire heats the structure. To that end, the structure does not reset into the superconducting state. The remaining in the high resistivity state is also called latching. The operation of an SNSPD in the latching operation is a largely unexploited scheme. The main advantage is that large output voltages can be generated from an initial single photon triggered breakdown. The generation of larger hotspots will decrease the risetime of the full signal since the risetime is dependent on the growth speed of the resistivity breakdown. The resistivity breakdown of these structures can be described by thermal coupling between the resistive nanowire and the substrate at a lower temperature [100, 101]. The maximal achievable output voltage of SNSPDs breakdown is therefore dependent on the provided electrical power to the structure.

To reset the nanowire the bias current must be switched off. The key to enable the latching operation is to use a current source closely integrated with the SNSPD. In the previous section 7.3, we established that a cryogenic photodiode can be used as a bias current source for an SNSPD. The cryogenic photodiode is therefore an cryogenically integrated optical-to-electrical power converter. Building on this principles, we can enable the latching technique of the SNSPD to achieve a larger output voltage of an SNSPD. The generated output voltage can be large enough such that the signal is large enough to achieve significant optical modulation with a electro-optic modulator.

Combining the opto-electronic bias of an SNSPD with an optical readout through an electro-optic modulator can achieve an all-optical operation. In section 7.4 this technique will be implemented and characterized. In the implementation, the output voltage is determined by the power provided by the cryogenic photodiode and the power dissipated by the SNSPD. The cryogenic photodiode is a non-ideal power source since it is not a perfect optical-to-power converter. Therefore, the maximal output voltage of the SNSPD is limited which has been shown in the characterization in section 7.4.

Towards feed-forward modulation: An outlook

4

In recent years, a quantum advantage in the photonic processors has been successfully shown [3, 5, 165]. Most prominent examples are the probabilistic process such as gaussian boson sampling [3, 5, 165]. However, these applications lack in the implementation universal logical gates such as controlled not gates [30, 31]. Alternative optical computing schemes were proposed such as the so-called one-way computing [29]. Following the proposed one-way computing scheme, an early implementation of one-way computing with active photonic components was shown with controlled CNOT-gate [93, 166]. To do so, a large set of entangled photons are generated known as cluster states. Based on the outcome of the measurement, consecutive cluster photons are modulated with an electro-optic modulator. The controlled modulation is known as feed-forward modulation.

In principle, an ancillary photon is detected and thus absorbed which will trigger an optical modulation in the network. Up to now, optical nonlinearities capable of inducing such a strong modulation are not known [30]. All-optical switching techniques require typically much stronger optical pulses [167, 168]. In order to realize such a strong optical nonlinearity, the nonlinearity is established with electronically with light detection, signal amplification, and optical modulation. The optical-to-electrical conversion is used here to amplify the intermediate signals [93, 169, 170].

The technical implementation of a feed-forward enabled quantum computer is challenging due to the requirements for modulators and single photon detectors. Ideally, the single photon signal is amplified to a level such that the full optical modulation is achieved in the modulator such as a π shift in a phase modulator, a polarization rotation of about $\pi/2$ in a polarization converter or full coupling change from one output across to the other in a directional coupler.

In room temperature applications, feed-forward modulation was implemented for Shore's sorting algorithm [93]. Furthermore, the feed-forward operation is implemented to generate large entangled sets of photons such as cluster states [169, 170]. In these and similar implementations, the intermediate amplification is realized by room temperature amplifiers [171–174]. Scaling these applications up for more complex quantum computations will require the direct integration with cryogenic SNSPDs. A cryogenic feed-forward modulation has not been shown yet.

The field of cryogenic feed-forward modulation will need to employ low power amplifiers, capable of switching the SNSPDs output signal to the desired input amplitude for the electro-optic modulator. The technical challenges are similar the optical readout of cryogenic

electronic with modulators. A large output amplitude is desired and as well as a fast rise time. Key features can be identified in the all-optical operation of an SNSPD (in section 7.4) such that cryogenic feed-forward modulation can be implemented in the future.

One of the main requirements is a full optical modulation in the electro-optic modulator. In our initial implementation a signal of about 31 mV was achieved. Increasing the amplitude of the signal can be achieved by an optimization of the latching technique or by the addition of another amplifier. In the all-optical operation in section 7.4, the maximal output voltage was achieved when the input power to the nanowire is equal to the dissipated power. The nanowires heat dissipation is therefore dependent on the dimension of the nanowire and the heat coupling to the substrate [100, 101]. Other base substrates with a lower thermal dissipation can be considered to generate larger resistances in the latching operation in the SNSPD[89].

The cryogenic photodiode is used in this application as the power source. The investigations in section 7.4 show that the output voltage increases with the electrical load. Furthermore, the output power increases with the electrical load until it reaches a local maximum and decreases again. Generating a larger electrical load at lower resistances will generate a larger surplus of the dissipated heat and thus aid the growth of the resistive area. The increased input power will generate faster signal rise times and generate larger output voltages. In the photodiode investigations in section 7.4, it becomes evident that the output power becomes larger if the optical input power is increased. To that end, SNSPDs with a large bias current should be used such that the optical input power at the 90% bias point can be increased. The maximally achievable output voltage of the all-optical bias is limited to approximately 550 mV limited by the threshold voltage of the cryogenic photodiode.

Reconfiguring the tested electro-optic modulator could approach lower modulation voltages. The Michelson-interferometer required a modulation voltage of 6.6 V at cryogenic temperatures to switch between the reflected channels. In this configuration, the operation voltage can be halved to 3.3 V by modulating both waveguides in the opposite phase. To do so, a third electrode is placed on the second waveguide channel. This will induce a opposite phase shift in the second waveguide and thus double the phase difference. Further improvements in this material can only be achieved by increasing the length of the electrodes. To achieve a modulation voltage of about 500 mV for an all-optical feed-forward modulation will require about 130 mm long electrodes. However, the bandwidth of this modulator will be reduced by a factor of 6 due to the increase of the electrodes capacity. In addition, the footprint of the modulator is also strongly increased.

In lithium niobate, the modulation voltage can also be strongly decreased by light confinement. Thin film electro-optic modulators can be realized at cryogenic temperatures. Lomonte et al. [121] showed a thin film modulator with a voltage length product of about 3 Vcm. In a recent study an optimization of the electrode and waveguide structure demonstrated near 1 Vcm modulation strength at room temperature [175]. The lithium niobate platform promises to achieve with the higher confinement a stronger optical switching with a smaller footprint.

A convergence in the detectors output signal and modulators voltage will achieve cryogenic feed-forward modulation. However, the latching methods trades mainly the rise time with a large output amplitude. A fast signal rise time is desired in feed-forward applications since this will determine the length of optical delay lines for consecutive photons. Ideally, delay lines are realized with low loss waveguides on the integrated chips. On chip delay lines are can be realized in the order of a few centimeters. Bends in waveguides can make delay lines more compact. However, in titanium in-diffused waveguides bends cannot integrated space efficiently. In these applications, light can be delayed in single mode fibers since a high coupling efficiency can be achieved between fibers and lithium niobate. The total optical delay time must be equal to the rise time of the detection signal. In the all-optical SNSPD operation, a single mode fiber length of at least 2400 m should be used to achieve the 12 µs delay. Furthermore, the optical losses should be considered in the application. On chip delay lines achieve losses of about 0.1 dB/cm (10 dB/m). In comparison, single mode fibers achieve waveguide losses of 0.3 dB/km (0.0003 dB/m) such that interface losses between the fiber and waveguide are the largest contributor.

An alternative form of the signal amplification is the use of integrated amplifiers at cryogenic temperatures. Converting existing amplifiers from room temperature applications to the cryogenic applications can achieve fast signal rise times and a sufficient amplification. However, the power dissipation of these amplifiers will need to be considered. These amplifiers will need to bridge a signal gap of approximately 40 dB, assuming a 1 mV signal voltage and a modulation voltage of 6.6 V.

The introduced latching technique can aid the design of cryogenic amplifiers. Typically, the input impedance of the SNSPD and readout amplifier are matched to about 50 Ω. In contrast, the latching methods switches from a low resistive state in a high resistive state. Matching the input impedance of the signal amplifiers could enable more favorable amplification ranges. Furthermore, electronic reflections can be avoided which can perturb the electronic characteristics.

Feed-forward modulation at cryogenic temperatures is limited by the capabilities of the available photonic devices, in the near-term future. Lithium niobate remains as an important material platform for quantum photonic applications. The material benefits from low transmission losses, low coupling losses to single mode fibers as well as the large second order nonlinearity. Improving the modulation voltage with amplifiers at cryogenic temperatures is a significant aspect for the feed-forward modulation. Furthermore, bridging the gap between the single photon signal and the required modulation voltages remains an open challenge. Additionally, the signal risetime will need to be optimized to enable on chip delay lines for on-chip feed-forward modulation. In addition to the integration of nonlinear sources and integrated superconducting detectors, low coupling losses to waveguides are important to achieve low loss optical delays. In summary, the all-optical modulation of the SNSPD revealed key aspects to be optimized in the future for feed-forward modulation. Nonetheless, pursuing the path of all-optical feed-forward modulation could enable low power quantum operations in the future.

Summary

5

On the journey of quantum optical information processing, we need to tackle a broad range of challenges in the implementation. On the endeavor to use quantum optical systems to solve complex problems, large scale quantum optic systems are needed. Partitioning these complex problems allows to identify key fields of interest such as reconfigurable quantum systems, low power circuit operations and feed-forward modulation.

Photonic integration allows us to realize optical components for photon processing in a small system foot print. In this work, we identified lithium niobate as our material of choice since it enables us to build integrated quantum light sources, modulators and integrated single photon detectors. The capability to realize electro-optic modulation in the same environment as superconducting detectors lets us explore key concept for quantum photonic processing at cryogenic temperatures. Characterizing the electro-optic modulation in lithium niobate enabled the base understanding of the cryogenic modulation capabilities. Driving the platforms capabilities further enabled the low power operation of superconducting single photon detectors. The key to achieve this lies in the signal transformation between the optical and electronic domain. To achieve an optical power delivery for the superconducting detectors, we investigated cryogenic photodiodes as integrated current and power supplies. The opto-electronic bias of SNSPDs showed no significant performance degradation in comparison to the typical operation. However, the combined operation of a opto-electronic bias and electro-optic modulation shows key features to be optimized in the future such as the signal rise time and added dark counts. Nonetheless, the all-optical operation of the SNSPD also reveals that improvements in the optical modulation and detection signal amplitude can enable feed-forward modulation.

In summary, we characterized the operation of key opto-electronic components for quantum photonic applications. The explored lithium niobate platform allows us to manipulate the phase, direction and polarization of light in an integrated cryogenic platform. Furthermore, we can combine cryogenic photodiodes with electro-optic modulation to operate superconducting detectors in a low power method.

Publications and Contributions

6

6.1 First Author publications

- **Publication:**
  "Cryogenic electro-optic polarisation conversion in titanium in-diffused lithium niobate waveguides," in Opt. Express, vol. 28, no. 20, p. 28961, Sep. 2020.

  Authors:
  Frederik Thiele[1], Felix vom Bruch[2], Victor Quiring[2], Raimund Ricken[2], Harald Herrmann[2], Christof Eigner[2], Christine Silberhorn[2] and Tim J. Bartley[1]

  Affiliations:
  [1] Mesoscopic Quantum Optics, Department Physics, Paderborn University, Warburger Str. 100, 33098 Paderborn, Germany
  [2] Integrated Quantum Optics, Department Physics, Paderborn University, Warburger Str. 100, 33098 Paderborn, Germany

  Contribution:
  FT designed and constructed the setup for the cryogenic electro-optic characterization. FT prepared the wavelength and temperature dependent simulations of the refractive index. FvB, VQ and RR fabricated the lithium niobate sample. FT packaged and pigtailed the sample. FT carried out the room temperature and cryogenic characterization and data analysis. FT wrote the manuscript with the supervision of TB. TB supervised the project. All authors contributed to the discussion of results and commented on the manuscript.

- **Publication:**
  "Cryogenic electro-optic modulation in titanium in-diffused lithium niobate waveguides," J. Phys. Photonics, vol. 4, no. 3, p. 034004, Jul. 2022.

  Authors:
  Frederik Thiele[1], Felix vom Bruch [2], Julian Brockmeier [1], Maximilian Protte [1], Thomas Hummel [1], Raimund Ricken [2], Victor Quiring [2], Sebastian Lengeling [2], Harald Herrmann [2], Christof Eigner [2], Christine Silberhorn [2] and Tim J. Bartley [1]

  Affiliations:
  [1] Mesoscopic Quantum Optics, Department Physics, Paderborn University, 33098 Paderborn Warburger Str. 100, Germany

[2] Integrated Quantum Optics, Department Physics, Paderborn University, 33098 Paderborn Warburger Str. 100, Germany

Contribution:
FT designed and constructed the setup for the cryogenic electro-optic characterization. FvB, JB, MP, RR, VQ and SL fabricated the lithium niobate samples. FT carried out the characterizations between room temperature and cryogenic temperatures. The analysis was done by FT. FT wrote the manuscript with the supervision of TH and TB. TB supervised the project. All authors contributed to the discussion of results and commented on the manuscript.

- **Publication:**
  "Opto-electronic bias of a superconducting nanowire single photon detector using a cryogenic photodiode," in APL Photonics, vol. 7, no. 8, p. 081303, Aug. 2022.

  Authors:
  Frederik Thiele[1], Thomas Hummel[1], Maximilian Protte[1] and Tim J. Bartley[1]

  Affiliations:
  [1] Physics Department, Paderborn University, Paderborn 33098, Germany

  Contribution:
  The idea was conceived by FT. FT carried out the characterizations between room temperature and cryogenic temperatures. The analysis was done by FT in discussion with TH. FT wrote the manuscript with the supervision of TH and TB. TB supervised the project. All authors contributed to the discussion of results and commented on the manuscript.

- **Publication:**
  "All optical operation of a superconducting photonic interface," in arXiv arXiv:2302.12123, Feb. 2023.

  Authors:
  Frederik Thiele[1], Thomas Hummel[1], Adam N. McCaughan[1], Julian Brockmeier[1], Maximilian Protte[1], Victor Quiring[1], Sebastian Lengeling[1], Christof Eigner[1], Christine Silberhorn[1] and Tim J. Bartley[1]

  Affiliations:
  [1]Institute for Photonic Quantum Systems, Paderborn University, Warburger Str. 100, Paderborn, Germany
  [2]National Institute of Standards and Technology, 325 Broadway, Boulder, CO, USA, 80305

  Contribution:
  The idea of an all-optical SNSPD operation was conceived by FT. The superconducting latching idea for signal amplification was conceived by AMcC. JB, MP, RR, VQ and SL fabricated the lithium niobate samples. FT carried out the characterizations

at room temperature and cryogenic temperatures. The analysis was done by FT in discussion with TH. FT wrote the manuscript with the supervision of TH and TB. TB supervised the project. All authors contributed to the discussion of results and commented on the manuscript.

- **Publication:**
  "Pyroelectric Influence on Lithium Niobate During the Thermal Transition for Cryogenic Integrated Photonics," in arXiv arXiv:2306.12123, Jun. 2023.

  Authors:
  Frederik Thiele[1], Thomas Hummel[1], Nina Amelie Lange[1], Felix Dreher[1], Maximilian Protte[1], Felix vom Bruch[1], Sebastian Lengeling[1], Harald Herrmann[1], Christof Eigner[1], Christine Silberhorn[1], and Tim J. Bartley[1]

  Affiliations:
  [1] Department of Physics & Institute for Photonic Quantum Systems, Paderborn University, Warburger Str. 100, Paderborn, Germany

  Contribution:
  FD and TH made initial investigations in the electronic characterization of lithium niobate in thermal transition between room temperature and cryogenic temperatures. FT conceived the idea of the simultaneous electronic and optical measurement in lithium niobate in discussion with FD. JB, MP, RR, VQ and SL fabricated the lithium niobate samples. FT carried out the characterizations at room temperature and cryogenic temperatures. The analysis was done by FT in discussion with TH. FT wrote the manuscript contributions of NL and TH. TB supervised the project. All authors contributed to the discussion of results and commented on the manuscript.

6.2 Contributed Publications

- **Publication:**
  "Cryogenic Second-Harmonic Generation in Periodically Poled Lithium Niobate Waveguides," Phys. Rev. Appl., vol. 15, no. 2, p. 024028, Feb. 2021.

  Authors:
  Moritz Bartnick[1], Matteo Santandrea[1], Jan Philipp Höpker[1], Frederik Thiele[2], Raimund Ricken[2], Viktor Quiring[2], Christof Eigner[2], Harald Herrmann[2], Christine Silberhorn[2] and Tim J. Bartley[1]

  Affiliations:
  [1] Department of Physics, Mesoscopic Quantum Optics, Paderborn University, Warburger Strasse 100, Paderborn 33098, Germany
  [2] Department of Physics, Integrated Quantum Optics, Paderborn University, Warburger Strasse 100, Paderborn 33098, Germany

Contribution:
MB made the optical characterization. MB wrote the manuscript. FT provided MB with refractive index simulations dependent on the wavelength and temperature. All authors contributed to the discussion of results and commented on the manuscript.

6.3 Conference Contributions

- **Presentation:**
  "Polarisation Modulation in Lithium Niobate Waveguides at 0.8K," DPG Herbsttagung 2019.

  Authors:
  Frederik Thiele[1], Jan Philipp Höpker[1], Patrick Bartowiak[2], Felix vom Bruch[2], Raimund Ricken[2], Victor Quiring[2], Christof Eigner[2], Christine Silberhorn[2] and Tim J. Bartley[1]

  Affiliations:
  [1] Department of Physics, Mesoscopic Quantum Optics, Paderborn University, Warburger Strasse 100, Paderborn 33098, Germany
  [2] Department of Physics, Integrated Quantum Optics, Paderborn University, Warburger Strasse 100, Paderborn 33098, Germany

  Contribution:
  Oral presentation by Frederik Thiele

- **Presentation:**
  "Electro-optic polarisation conversion at 0.8K in titanium in-diffused lithium niobate waveguides," in Conference on Lasers and Electro-Optics, OSA Technical Digest (Optica Publishing Group, 2020), paper STh1F.2.

  Authors:
  Frederik Thiele[1], Jan Philipp Höpker[1], Moritz Bartnick[1], Felix vom Bruch[2], Harald Herrmann[2], Raimund Ricken[2], Victor Quiring[2], Christof Eigner[2], Christine Silberhorn[2] and Tim J. Bartley[1]

  Affiliations:
  [1] Department of Physics, Mesoscopic Quantum Optics, Paderborn University, Warburger Strasse 100, Paderborn 33098, Germany
  [2] Department of Physics, Integrated Quantum Optics, Paderborn University, Warburger Strasse 100, Paderborn 33098, Germany

  Contribution:
  Oral presentation by Frederik Thiele

- **Presentation:**
  "Cryogenic operation of a polarisation cinverter and directional coupler in

LiNbO3 for quantum circuits," in European Conference on Integrated Optics, 2020.

Authors:
Frederik Thiele[1], Jan Philipp Höpker[1], Felix vom Bruch[2], Harald Herrmann[2], Raimund Ricken[2], Victor Quiring[2], Christof Eigner[2], Christine Silberhorn[2] and Tim J. Bartley[1]

Affiliations:
[1] Department of Physics, Mesoscopic Quantum Optics, Paderborn University, Warburger Strasse 100, Paderborn 33098, Germany
[2] Department of Physics, Integrated Quantum Optics, Paderborn University, Warburger Strasse 100, Paderborn 33098, Germany

Contribution:
Poster presentation by Frederik Thiele

- **Presentation:**
  "Optical readout of a superconducting single photon detector with a cryogenic modulator," in Conference on Lasers and Electro-Optics Europe, 2021.

  Authors:
  Frederik Thiele[1], Thomas Hummel[1], Felix vom Bruch[2], Victor Quiring[2], Raimund Ricken[2], Harald Herrmann[2], Christof Eigner[2], Christine Silberhorn[2] and Tim J. Bartley[1]

  Affiliations:
  [1] Department of Physics, Mesoscopic Quantum Optics, Paderborn University, Warburger Strasse 100, Paderborn 33098, Germany
  [2] Department of Physics, Integrated Quantum Optics, Paderborn University, Warburger Strasse 100, Paderborn 33098, Germany

  Contribution:
  Oral presentation by Frederik Thiele

- **Presentation:**
  "Cryogenic electro-optic modulation in titanium in-diffused lithium niobate waveguides," in DPG Frühjahrstagnung, 2021.

  Authors:
  Frederik Thiele[1], Felix vom Bruch[2], Julian Brockmeier[1], Maximilian Protte[1], Thomas Hummel[1], Raimund Ricken[2], Victor Quiring[2], Sebastian Lengeling[2], Harald Herrmann[2], Christof Eigner[2], Christine Silberhorn[2] and Tim J. Bartley[1]

  Affiliations:
  [1] Department of Physics, Mesoscopic Quantum Optics, Paderborn University, Warburger Strasse 100, Paderborn 33098, Germany
  [2] Department of Physics, Integrated Quantum Optics, Paderborn University, Warburger Strasse 100, Paderborn 33098, Germany

Contribution:
Oral presentation by Frederik Thiele

- **Presentation:**
  "Cryogenic Optical Biasing of a Superconducting Nanowire Single Photon Detector with a Photodiode," in Conference on Lasers and Electro-Optics, OSA Technical Digest (Optica Publishing Group, 2022), FM4C.2, 2022.

  Authors:
  Frederik Thiele[1], Thomas Hummel[1], Maximilian Protte[1] and Tim J. Bartley[1]

  Affiliations:
  [1] Department of Physics, Mesoscopic Quantum Optics, Paderborn University, Warburger Strasse 100, Paderborn 33098, Germany

  Contribution:
  Oral presentation by Frederik Thiele

- **Presentation:**
  "Cryogenic Electro-Optic Modulation in Titanium in-diffused Lithium Niobate Waveguides," in International Conference on Integrated Quantum Photonics 2022.

  Authors:
  Frederik Thiele[1], Felix vom Bruch[1], Julian Brockmeier[1], Maximilian Protte[1], Thomas Hummel[1], Raimund Ricken[1], Victor Quiring[1], Sebastian Lengeling[1], Harald Herrmann[1], Christof Eigner[1], Christine Silberhorn[1] and Tim J. Bartley[1]

  Affiliations:
  [1] Institute for Photonic Quantum Systems, Department of Physics, Paderborn University, Warburger Str. 100

  Contribution:
  Oral presentation by Frederik Thiele

- **Presentation:**
  "All optical operation of a superconducting photonic interface" in Bristol Quantum Information Technologies Workshop 2023.

  Authors:
  Frederik Thiele[1], Thomas Hummel[1], Adam McCaughan[2], Julian Brockmeier[1], Maximilian Protte[1], Victor Quiring[1], Sebastian Lengeling[1], Christof Eigner[1], Christine Silberhorn[1] and Tim J. Bartley[1]

  Affiliations:
  [1] Institute for Photonic Quantum Systems, Department of Physics, Paderborn University, Warburger Str. 100
  [2] National Institute of Standards and Technologies, 325 Broadway, Boulder, CO, USA, 80305

Contribution:
Poster and Oral presentation by Frederik Thiele

- **Presentation:**
  "All-optical biasing and readout of a superconducting single photon detector" in Conference on Lasers and Electro-Optics, OSA Technical Digest (Optica Publishing Group, 2023), 2023.

  Authors:
  Frederik Thiele[1], Thomas Hummel[1], Adam McCaughan[2], Julian Brockmeier[1], Maximilian Protte[1], Victor Quiring[1], Sebastian Lengeling[1], Christof Eigner[1], Christine Silberhorn[1] and Tim J. Bartley[1]

  Affiliations:
  [1] Institute for Photonic Quantum Systems, Department of Physics, Paderborn University, Warburger Str. 100
  [2] National Institute of Standards and Technologies, 325 Broadway, Boulder, CO, USA, 80305

  Contribution:
  Oral presentation by Frederik Thiele

- **Presentation:**
  "Characterizing all-optical biasing and readout of a superconducting optoelectronic circuit" in Conference on Lasers and Electro-Optics Europe, 2023.

  Authors:
  Frederik Thiele[1], Thomas Hummel[1], Adam McCaughan[2], Julian Brockmeier[1], Maximilian Protte[1], Victor Quiring[1], Sebastian Lengeling[1], Christof Eigner[1], Christine Silberhorn[1] and Tim J. Bartley[1]

  Affiliations:
  [1] Institute for Photonic Quantum Systems, Department of Physics, Paderborn University, Warburger Str. 100
  [2] National Institute of Standards and Technologies, 325 Broadway, Boulder, CO, USA, 80305

  Contribution:
  Oral presentation by Frederik Thiele

Publications 7

7.1 Cryogenic electro-optic polarisation conversion in titanium in-diffused lithium niobate waveguides

Frederik Thiele[1], Felix vom Bruch[2], Victor Quiring[2], Raimund Ricken[2], Harald Herrmann[2], Christof Eigner[2], Christine Silberhorn[2] and Tim J. Bartley[1]

[1] Mesoscopic Quantum Optics, Department Physics, Paderborn University, Warburger Str. 100, 33098 Paderborn, Germany
[2] Integrated Quantum Optics, Department Physics, Paderborn University, Warburger Str. 100, 33098 Paderborn, Germany

Publication:
"Cryogenic electro-optic polarisation conversion in titanium in-diffused lithium niobate waveguides," Opt. Express, vol. 28, no. 20, p. 28961, Sep. 2020.
https://doi.org/10.1364/OE.399818

Abstract

Many technologies in quantum photonics require cryogenic conditions to operate. However, the underlying platform behind active components such as switches, modulators and phase shifters must be compatible with these operating conditions. To address this, we demonstrate an electro-optic polarisation converter for 1550 nm light at 0.8 K in titanium in-diffused lithium niobate waveguides. To do so, we exploit the electro-optic properties of lithium niobate to convert between orthogonal polarisation modes with a fiber-to-fiber transmission >43%. We achieve a modulation depth of 23.6±3.3 dB and a conversion voltage-length product of 28.8 Vcm. This enables the combination of cryogenic photonics and active components on a single integration platform.

Introduction

The current state-of-the-art in high-speed single photon detectors are based on superconducting nanowires [61, 176]; such detectors have demonstrated timing jitters below 5 ps [177]. Modulation in quantum photonics typically exploits advances in integrated optics, although the lowest loss implementations still rely on bulk devices to maximise efficiency. This makes integration with superconducting detectors extremely challenging due to the cryogenic operating requirements. Indeed, many modulation techniques in

integrated platforms also rely on approaches which are incompatible with cryogenic or low-loss operation, such as thermo-optic[178] or carrier-injection[40].

By contrast, integrated optics based on titanium in-diffused waveguides in lithium niobate (Ti:LN) platform offers several advantages in this regard. As a material with a high electro-optic coefficient, it is compatible in principle with cryogenic operation. Furthermore, its large mode sizes are well-matched to optical fibre, which reduces overall losses. Indeed, many quantum photonic components have been integrated on this platform. However, quantum-compatible operation of these components under cryogenic conditions - and thereby compatibility with integrated superconducting detectors, remains an open challenge.

While phaseshifting has been achieved at cryogenic temperatures in lithium niobate [28, 59, 83, 179] and other platforms [40, 48], low-temperature operation of active polarisation conversion is yet to be demonstrated. The polarisation degree of freedom is a very natural basis for encoding qubits on a single photon level, therefore efficient control is an important tool in many quantum photonic information tasks. Moreover, at room temperature active polarisation conversion has been established since the 1980s [180–184] and has also been developed in thin-film lithium niobate (LNOI) [185, 186]. However, until now, active polarisation conversion at low temperatures has not been demonstrated.

In this paper, we demonstrate that polarisation conversion in z-cut Ti:LN is indeed fully functional at the temperatures required for superconducting detectors. We show electro-optic conversion between orthogonal polarisation modes from room temperature down to 0.8 K. This expands the degrees of freedom with which single photons can be manipulated for quantum photonic tasks [9] whilst maintaining compatibility with the operating conditions of superconducting detectors, as well as other low-temperature quantum photonic technologies such as many single photon emitters.

This paper is organised as follows. We first describe the operation of the electro-optic polarisation converter in terms of a temperature-dependent quasi-phase-matched nonlinear process. We then present the experimental methods for testing the device in a robust, plug-and-play configuration. The results are presented in section 7.1 before summarising in section 7.1.

Temperature dependence of polarisation conversion

Phase-matching

Polarisation conversion in lithium niobate is a phase-matched interaction between two orthogonally polarised optical modes [44] (henceforth referred to as transverse electric - TE, and transverse magnetic - TM) and a static electric field. The interaction can be modeled as a coupling between the TE and TM modes, mediated by the DC electric field E_{DC}, in a configuration shown in Fig. 7.1.

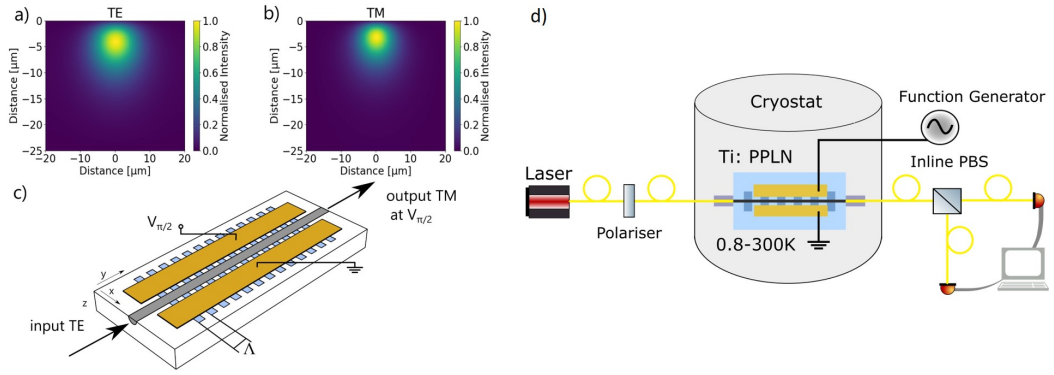

Figure 7.1: a), b) The normalised spatial intensity distribution of the supported optical modes, TE and TM, respectively. c) Schematic of the polarisation converter, including poling period Λ. The linear polarisation mode TE is converted to TM if the voltage of $V_{\pi/2}$ is applied at the electrodes. d) Schematic of the optical characterisation set up. All components other than the waveguide operate at room temperature. The sample is optically accessed via fiber feed-throughs.

An important property of the waveguides in Ti:LN is that they support low-loss propagation of orthogonal polarisation modes with a high degree of overlap (as shown in Fig. 7.1 a)); however, since lithium niobate is a birefringent material, the propagation constants for each mode are different. However, a periodic domain inversion in the crystal, with a chosen period length Λ, can be used to compensate the phase mismatch between the two polarisation modes at a specific wavelength λ_{pm}. Given temperature- and wavelength-dependent refractive indices $n_{\mathrm{TE}}(\lambda, T)$, $n_{\mathrm{TM}}(\lambda, T)$, the phase mismatch between the modes $\Delta\beta$ is given by

$$\Delta\beta = 2\pi \left(\frac{n_{\mathrm{TE}}(\lambda, T) - n_{\mathrm{TM}}(\lambda, T)}{\lambda} \right) - \left(\frac{2\pi}{\Lambda} \right) . \tag{7.1}$$

While the period length Λ remains broadly temperature insensitive, it is clear that the phase-matched wavelength $\lambda_{\mathrm{pm}} = \Lambda \left(n_{\mathrm{TE}}(\lambda, T) - n_{\mathrm{TM}}(\lambda, T) \right)$, for which $\Delta\beta = 0$, will vary with temperature.

To phase-match the conversion process in the optical telecommunication band at room temperature, a poling period of around 20 µm is required. By extrapolating the Sellmeier equations for the refractive indices for our waveguide system [187] down to cryogenic temperatures around 1 K, and taking into account the effective refractive index caused by the titanium diffusion profile of our waveguides, we expect a shift in the phase-matched wavelength by up to 100 nm. This is indicated in Fig. 7.2. We thus choose a poling period of 19.9 µm, which is expected to be phase-matched around 1560.5 nm at cryogenic temperatures and 1467.4 nm at room temperature. Phase-matching across this range of wavelengths can be tested using a tunable laser of suitable tuning range, as described in Section 7.1.

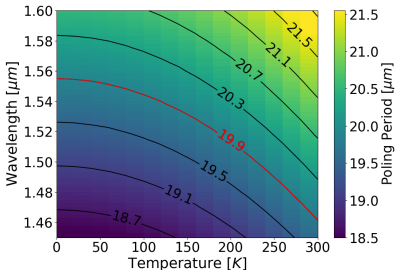

Figure 7.2: Extrapolated poling period from the Sellmeier equations in combination with the titanium in-diffusion profile required to phase-match the conversion process at a given wavelength and temperature.

Coupled mode equations

Given initial amplitudes of the orthogonal modes $A_{\mathrm{TE}}(0)$, $A_{\mathrm{TM}}(0)$, the solution of the coupled mode equations describing the conversion process after propagating a distance y are given by [44]

$$\begin{pmatrix} A_{\mathrm{TE}}(y) \\ A_{\mathrm{TM}}(y) \end{pmatrix} = \begin{pmatrix} \cos(sy) + \frac{i\Delta\beta}{2s}\sin(sy) & -\frac{\kappa}{s}\sin(sy) \\ +\frac{\kappa}{s}\sin(sy) & \cos(sy) - \frac{i\Delta\beta}{2s}\sin(sy) \end{pmatrix} \cdot e^{\frac{i\Delta\beta y}{2}} \begin{pmatrix} A_{\mathrm{TE}}(0) \\ A_{\mathrm{TM}}(0) \end{pmatrix}, \tag{7.2}$$

with $s = \sqrt{\kappa^2 + (\Delta\beta/2)^2}$. The coupling strength κ, given by

$$\kappa = \frac{\pi\, n_{\mathrm{eff}}^3 \eta r V}{\lambda G}, \tag{7.3}$$

depends on the crystal orientation of the lithium niobate and the corresponding electro-optic coefficient r, as well as the spatial mode overlap η of the polarisation modes E_{TE}, E_{TM} and electric field E_{DC}, which is generated by a voltage V at the electrodes with the gap G. The effective refractive index is here defined as $n_{\mathrm{eff}}^3 = n_{TE}^{3/2} n_{TM}^{3/2}$ and the spatial overlap η is determined by the spatial overlap of the electric fields, namely

$$\eta = \frac{G}{V} \frac{\int_A E_{\mathrm{TE}}(x,z) E_{\mathrm{TM}}(x,z) E_{\mathrm{DC}}(x,z)\,\mathrm{d}A}{\int_A E_{\mathrm{TE}}(x,z) E_{\mathrm{TM}}(x,z)\,\mathrm{d}A}. \tag{7.4}$$

Experimental implementation

To demonstrate the effects of temperature on the electro-optic conversion process, we fabricated and characterised a robust, fibre-coupled device based on titanium in-diffused

waveguides in periodically-poled, z-cut lithium niobate [8, 79]. Despite the lower electro-optic coefficient of z-cut lithium niobate, this cut was chosen in order to be forward compatible with other nonlinear processes such as frequency conversion.

Device geometry

The device itself consists of a waveguide of a length of 25 mm, which is is poled with a period of 19.9 µm. The waveguides are formed by in-diffusing a 6 µm-wide and 80 nm-thick stripe of titanium into the lithium niobate sample. Afterwards, the poling structures are fabricated using liquid electrodes, followed by application of high voltage pulses to invert the crystal. After the poling procedure, gold electrodes with a buffer-layer of 200 nm SiO_2 in between were deposited, with a length of 15 mm, a separation of 15 µm and a width of 400 µm. This electrode structure should act as an ideal capacitor, of capacitance of 9.2 pF, given the electrode geometry [45]. As such, the converter should not dissipate any electric energy, which would be detrimental to operation inside a low-temperature cryostat. In practise, however, impedance miss-matches and stray resistances throughout the circuit may cause some electrical energy dissipation. Wire bonds from the electrodes to electrical connectors allow an external bias voltage to be applied via a coaxial cable. The linear losses in these waveguides are measured to be about 0.17 dB/cm in the TE-polarisation and 0.17 dB/cm in the TM-polarisation at room temperature in the optical C-band [148].

Packaging

To enable operation of the sample in a cryostat, the device was butt-coupled ("pigtailed") to single mode polarisation maintaining (PM) fibres using UV-curable adhesive (Norland 81). Together with an anti-reflective coating between the fibre and sample, fiber-to-fiber efficiency of 55% were achieved at room temperature. For mechanical robustness during temperature cycling, the sample is mounted on a copper holder and the fibres are attached to additional side blocks for strain relief. These fibres are then spliced (with approximately 0.01dB additional loss per splice) to PM fiber feed-throughs, providing optical access in and out of the cryostat. When cooled to cryogenic temperatures, coupling efficiencies of 43% were achieved. Changes in the coupling efficiency can be attributed to thermal stresses at the butt-coupled joints.

Characterisation methods

To characterise the device at cryogenic temperatures, the device is mounted on a cold stage of a closed-cycle cryostat (PhotonSpot Cryospot 4) which can reach a base temperature of 0.77 K, as shown in Fig. 7.1 d). During the device cooling process, light of one polarisation was coupled into the device, and the output polarisation was optically monitored. Effects of both wavelength and applied voltage were monitored during the cooling process. Using a tunable laser (EXFO T100S-HP/SCL) with a power of approximately 200 µW, the

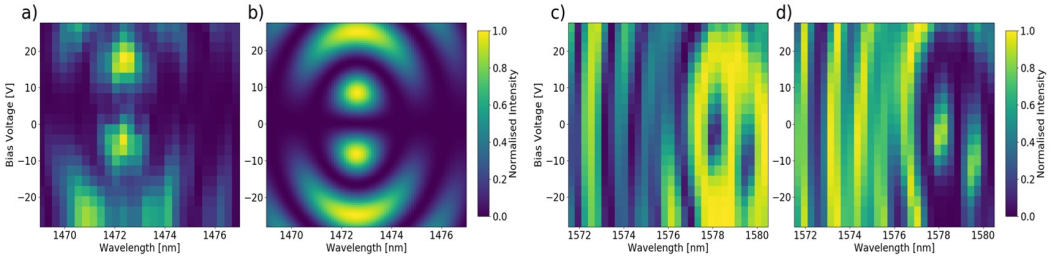

Figure 7.3: Conversion maps showing the normalised intensity of the TM polarisation mode by modulating the bias voltage and wavelength given a TE input polarisation. a) Experimental data of conversion at room temperature. b) Theoretical conversion map determined by the transfer matrix in Sec. 7.1. Conversion maps for c) TE and d) TM output polarisation at 0.8 K given a TE input polarisation. The intensities in these graphs are normalised for every data point by the sum of the intensities of both polarisations: $I_{\mathrm{TE,TM}}(V,T)/[I_{\mathrm{TE}}(V,T)+I_{\mathrm{TM}}(V,T)]$

wavelength was swept in 0.3 nm steps in a range of 9 nm centred at a wavelength of 1472.5 nm, and the bias voltage swept from -30 to 30 V in 2.5 V steps. The entire sweep lasts approximately 100 seconds. The resulting intensity modulation at 296 K is represented as a conversion map in Fig. 7.3 a) and is in a good agreement with the theoretically determined conversion map in Fig. 7.3 b), determined by the derived transfer matrix in Sec. 7.1.

This sweep was repeated during temperature cycling, whereby the center wavelength around which the laser was swept was based on a tracking algorithm which sought the wavelength which maximised conversion efficiency. Using this technique, 576 wavelength-voltage conversion maps, such as Fig. 7.3 a) and b), were acquired across a temperature range from 296-0.8 K, and an overall wavelength range of 1468 nm to 1581 nm. The overall cool-down time is around 16 hours, with a maximum cooling rate of approximately 0.3 K/min. This method results in a temperature uncertainty across the switching maps of less than 1 K.

Results

The primary result is that polarisation conversion was observed down to 0.8 K, at a wavelength of 1578.2 nm, with a modulation depth of 23.6±3.3 dB, and a modulation voltage of 19.1±2.1 V. The switching map at this temperature, as shown in Fig. 7.3 c) and d), shows significant deviations from the expected behavior, and quantitative analysis of this discrepancy is highly challenging. We suggest that it is the effects of pyro-electric charge accumulation due to the temperature changes which play a significant role in affecting the field distribution both inside and outside the poled region of the waveguide, giving rise to additional polarisation mode coupling conditions. Despite these effects, by considering solely the phase-matched wavelength, the device retains its functionality across the whole temperature range.

In terms of cryogenic compatibility, optical losses are the primary source of thermal heat load of the device. When testing at base temperature, the 43% fiber-to-fiber efficiency and testing at an optical power level of ca. 200 µW raised the base temperature by around 200 mK to 1 K (over a timescale of ca. 10 minutes). This base temperature is well-within the operating requirements of superconducting detectors, and furthermore the temperature increase would not be present if the device was operating on the single-photon regime. Additional thermal effects arising from the modulation circuitry were not observed, and would anyway depend on the operating speed of the device.

Using the conversion maps obtained during temperature cycling (see Visualisation 1 [188]), we characterise our device at the phase-matched wavelength over the full temperature range. We define the phase-matched wavelength to be the wavelength at which the modulation depth is maximised, (whereby the modulation depth is defined at the ratio of maximum to minimum intensity when the voltage is swept).

Phase-matched wavelength

The dependence of the phase-matched wavelength on temperature is shown in Fig. 7.4 e). Operation across the whole temperature range was maintained, and as expected, the phase-matched wavelength increases with decreasing temperature. However, the magnitude of the shift, namely 107 nm, is larger than the 94 nm predicted by extrapolating the Sellmeier equations. We also observe a small quantitative offset between the model and the measured value at room temperature, which we attribute to imperfections of the modelling of the titanium diffusion profile of the waveguide. Overall, the extrapolation agrees reasonably well with the phase-matched wavelength down to 150 K, but deviates significantly at lower temperatures. This shows that further corrections to the Sellmeier equations in this temperature range are required. The experimental data also matches the qualitative features of the simulation, in that the dependence of the center wavelength with temperature approaches zero as the temperature approaches 0 K.

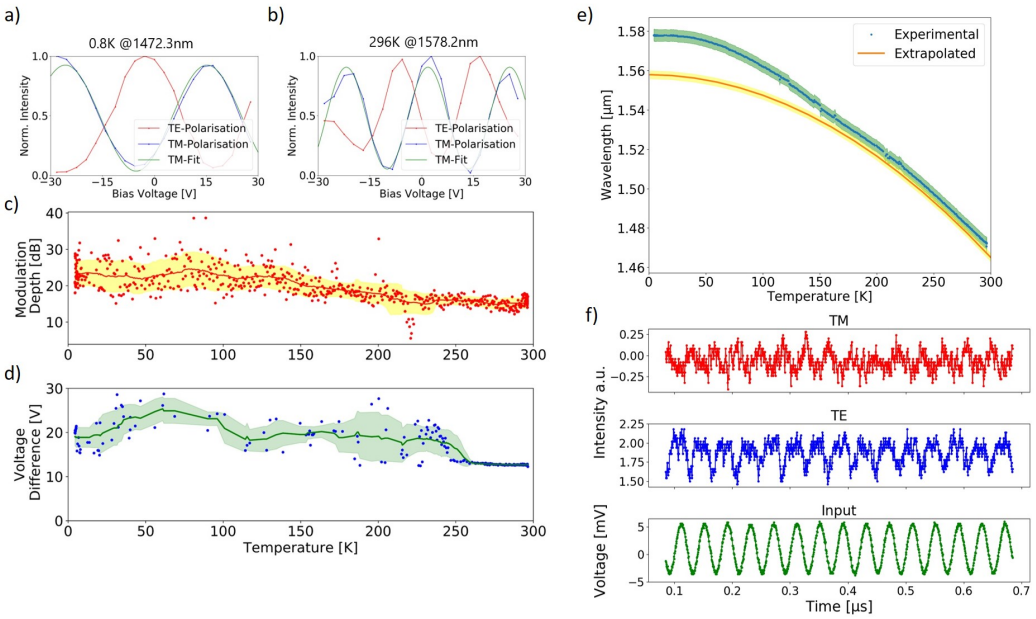

Figure 7.4: a), b): Voltage dependent intensity modulation at 0.8 K for 1578.2 nm and at 296 K for 1472.3 nm, respectively. c): Maximum modulation depth determined across the temperature range. The modulation depth is the ratio of the minimum and maximum intensity in the voltage sweeps, e.g. a) and b). The yellow band indicates a moving average over 15 K. d): Conversion voltage $V_{\pi/2}$ required to convert TE to TM, as a function of temperature. This can be determined by the period of the sine-fit as seen in the voltage sweeps in a), b). The green band is the $V_{\pi/2}$-average in the temperature range of 10 K. e) Phase-matched wavelength as a function of temperature. Blue dots & green region: experimental data and experimental error, respectively. Red line & yellow region: extrapolated wavelength and simulation uncertainty, respectively. f) Time-dependent modulation of the polarisation converter at 0.8 K at 25 MHz. The device is biased by 9 V to be operated at the point of inflection of the voltage sweep.

Modulation depth

In Fig. 7.4 a) and b) we show how the power in each polarisation mode depends on the applied voltage, carried out at a fixed temperature and wavelength. From these plots, we determine the modulation depth as the ratio of the maximum to minimum intensity. Fig. 7.4 c) shows how the modulation depth changes as a function of temperature. Throughout the entire temperature range, a modulation depth of the device was maintained around 15-25 dB, even increasing slightly at lower temperatures. At 0.8 K, we measure a modulation depth of 23.6±3.3 dB, with error bars determined statistically. This demonstrates that polarisation can be manipulated with the precision required for quantum optical experiments, i.e. that polarisation states with a fidelity of 99.6% can be reached.

Modulation Voltage

From Figs. 7.4 a) and b), we determine the modulation voltage at the phase-matched wavelength by the period of a sinusoidal fit to the voltage sweep. The modulation voltage required for a full polarisation conversion is in the range of 12.7±0.1 V at room temperature for the 15 mm long electrodes. This increases to 19.2±2.1 V at 0.8 K during the cooling process as shown in Fig. 7.4 d), which results in a voltage-length switching product of 28.8 Vcm. Further optimisations to electrode geometries would depend on the required application; high-speed applications typically require low conversion voltages while fine polarisation control is achieved with high conversion voltage-length products.

It is also apparent from Fig. 7.4 d) that the switching voltage increases and becomes much more noisy in the temperature range 10 K-250 K, which we again attribute to the accumulation of pyro-electric charge, since the rate of temperature change is maximal in this area. This changes the conversion properties at no externally applied voltage (0 V), but should be relatively straightforward to compensate by an additional D.C. bias voltage.

Modulation speed

For application in a quantum circuit, the operating speed of active components is an important parameter. In principle, the electrode design of our polarisation converter permits fast electro-optic control [45]. In practice, operating speeds are limited by driving electronics as much as the active devices themselves. Moreover, operating inside a low-temperature cryostat adds additional complexity. Nevertheless, in a proof-of-principle experiment to investigate typical operating speeds, we tested our device at 0.8 K when connected to a 25 MHz function generator. This created a sine-signal with an amplitude of 10 mV, which was limited by the high impedance of the electrodes. The voltage signal was biased by about 9 V so that the modulation is incident at the point of inflection of the voltage sweep. The output signal was tracked with an NIR-photodiodes and an oscilloscope. Plots showing the response of the diodes to each polarisation are shown in Fig. 7.4 f). A

modulation depth of around 1.8 dB was achieved, which is strongly limited by the signal-to-noise ratio of the diodes and maximal applied voltage amplitude on the electrode structure. Although a complete crossover in the polarisation was not reached, this experiment shows that MHz modulation is still possible in principle under cryogenic conditions.

Conclusion

In conclusion, we have presented an electro-optic polarisation converter at 0.8 V in titanium in-diffused lithium niobate waveguides. In so doing, we have demonstrated mutual compatibility between active electro-optic components for quantum photonic circuits and the operating conditions required for superconducting detectors. Under these conditions, we have shown a fibre-to-fibre coupling efficiency of 43% and a modulation depth of 23.6±3.3 dB.

When observing the dynamics during the cooling process, the change in temperature shifts the phase-matched wavelength by 107 nm, which is larger than predicted by extrapolating existing Sellmeier equations in combination with our waveguide modelling. Furthermore, we observe an increase in the modulation voltage from 12.7±0.1 V to 19.2±2.1 V, which suggests temperature dependence of the electro-optic coefficient in lithium niobate. The polarisation converter is capable of modulation at 25 MHz at a temperature of 0.8 V. Operation was preserved across the whole temperature range, despite complex dynamics during the cooling process which we attribute to pyro-electric charge accumulation. However, the device operates in a stable manner once at cryogenic temperatures. This functionality shows that polarisation conversion is compatible with other low-temperature technologies required for integrated quantum photonics.

Funding

This project is supported by the German Federal Ministry of Education and Research (BMBF) under the funding program Photonics Research Germany, grant number 13N14911; The Integrated Quantum Optics Group acknowledges funding from the European Commission through the ERC project QuPoPCoRN (Grant No. 725366).

Disclosures

The authors declare no conflicts of interest.

7.2 Cryogenic electro-optic modulation in titanium in-diffused lithium niobate waveguides

Frederik Thiele[1], Felix vom Bruch [2], Julian Brockmeier [1], Maximilian Protte [1], Thomas Hummel [1], Raimund Ricken [2], Victor Quiring [2], Sebastian Lengeling [2], Harald Herrmann [2], Christof Eigner [2], Christine Silberhorn [2], and Tim J. Bartley [1]

[1] Mesoscopic Quantum Optics, Department Physics, Paderborn University, 33098 Paderborn Warburger Str. 100, Germany
[2] Integrated Quantum Optics, Department Physics, Paderborn University, 33098 Paderborn Warburger Str. 100, Germany

Publication:
"Cryogenic electro-optic modulation in titanium in-diffused lithium niobate waveguides," J. Phys. Photonics, vol. 4, no. 3, p. 034004, Jul. 2022.
https://doi.org/10.1088/2515-7647/ac6c63

Abstract

Lithium niobate is a promising platform for integrated quantum optics. In this platform we aim to efficiently manipulate and detect quantum states by combining superconducting single photon detectors and modulators. The cryogenic operation of a superconducting single photon detector dictates the optimisation of the electro-optic modulators under the same operating conditions. To that end, we characterise a phase modulator, directional coupler, and polarisation converter at both ambient and cryogenic temperatures. The operation voltage $V_{\pi/2}$ of these modulators increases due to the decrease of the electro-optic effect by 74% for the phase modulator, 84% for the directional coupler and 35% for the polarisation converter below 8.5 K. The phase modulator preserves its broadband nature and modulates light in the characterised wavelength range. The unbiased bar state of the directional coupler changed by a wavelength shift of 85 nm while cooling the device down to 5 K. The polarisation converter uses periodic poling to phasematch the two orthogonal polarisations. The phasematched wavelength of the used poling changes by 112 nm when cooling to 5 K.

Introduction

Quantum photonics is a promising field since it enables and improves photonic technologies such as secure quantum communication [189], quantum computation [4], and metrology [190, 191]. Significant improvements can be made by integrating multiple photonic elements in a single unit. Integration reduces the footprint, increases circuit complexity,

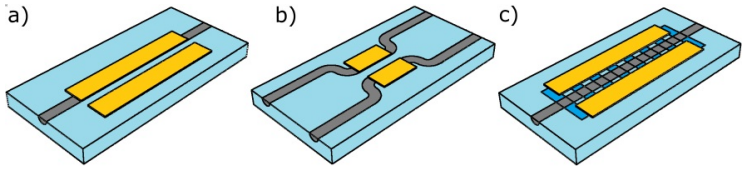

Figure 7.5: Electro-optic modulators in z-cut lithium niobate waveguides. a) polarisation converter b) directional coupler c) polarisation converter

and minimises interface losses and power consumption, thus enhancing scalability [9, 32, 192–195].

Quantum photonics requires the generation, manipulation, and detection of single photons. Scalable integrated quantum optics requires low system loss, nonlinear effects for photon generation and modulation, as well as efficient single-photon detection. Superconducting Nanowire Single Photon Detectors (SNSPDs) are one of the highest performing single photon detectors [90], since they achieve a detection efficiency of above 98% [11], a low timing jitter [13], and low dark count rates [14]. These superconducting detectors require cryogenic operating temperatures and have been integrated in photonic platforms [15].

An optimal photonic platform needs to combine the integrability of modulators and single photon detectors at cryogenic temperatures [51, 58, 193, 194]. Titanium in-diffused lithium niobate is an interesting platform to pursue this goal since it offers a large second order nonlinearity, low propagation loss, butt-coupling with single mode fibres, and integrability of SNSPDs [196, 197]. To generate and manipulate quantum states, spontaneous parametric down-conversion [26] as well as frequency conversion [25] has recently been shown at cryogenic temperatures in this platform. Furthermore, superconducting single photon detectors such as transition edge sensors [61] and SNSPDs have been integrated in lithium niobate [34, 35, 58, 71, 121, 198, 199]. Finally, lithium niobate offers a large electro-optic effect for optical modulation, which is also functional at cryogenic temperatures [36, 43, 83, 188, 200].

Nevertheless, cryogenic operation of modulators in lithium niobate is a understudied research area. Morse et al. and Yoshida et.al. [36, 43], independently demonstrated a directional coupler in lithium niobate at low temperature for the first time. The low-temperature electro-optic properties of bulk lithium niobate have been investigated in Ref. [83]. A cryogenic phase modulator was used in Refs. [58, 200] to read out a superconducting device. Polarisation conversion under cryogenic conditions was recently demonstrated by our group [188]. Building on these initial results, in this paper we investigate the performance metrics of three classes of electro-optic modulators in lithium niobate under cryogenic conditions. Specifically, we fabricate and compare a phase modulator, directional coupler, and polarisation converter below 8.5 K.

These devices are shown schematically in Fig. 7.5. Each device functions by coupling an externally applied electric field to modify the optical field(s) propagating in the waveguide. In Sec. 7.2, we provide a general theory for the operating principle of these electro-optic

devices, and their modifications under cryogenic operation. In Sec. 7.2 we give details on the fabrication of our devices, followed by the general characterisations setup in Sec. 7.2. The results for each modulator are given in Sec. 7.2, before begin compared in Sec. 7.2. Finally, we conclude in Sec. 7.2.

Theory

Optical modulation requires a controlled change of the refractive index. Several effects enable the change of the refractive index for example the electro-optic and acousto-optic effects [37, 44, 45]. To integrate modulators with SNSPDs, the modulators must not only function at cryogenic temperatures, but also be compatible with the cooling power of the cryostat. Acousto-optics [201], thermo-optics [38, 178], carrier injection [40], DC-Kerr [202] and the electro-optic effect [36, 43, 48, 56, 188] have been shown at cryogenic temperatures. Out of these effects, the electro-optic effect has great advantages for cryogenic applications since it only requires the generation of an electric field with electrodes and is preserved at cryogenic temperatures [36, 43, 83, 188]. We need to know how the electro-optic effect changes with a change in the temperature to integrate modulators with other optical components at cryogenic temperatures.

A change in the refractive index Δn_{ij} can be induced by an electric bias field E_{DC} through the electro-optic effect with a given effective refractive index of the waveguide $\tilde{n}_i$ via [18, 37]

$$\Delta\left(\frac{1}{n_i^2}\right) = r_{ij}E_j^{\mathrm{DC}} \tag{7.5}$$

$$\Delta n_i \approx -\frac{\tilde{n_i}^3}{2} r_{ij}E_j^{\mathrm{DC}}. \tag{7.6}$$

The phase modulator uses this retardation to delay the propagation through the waveguide such that the output phase is shifted. Furthermore, the change of the refractive index can be used to couple two optical modes. The interaction of the optical modes is used to couple spatial modes in the directional coupler and polarisation modes in a polarisation converter. The resulting coupling between the optical modes is described by the coupled mode equations [44]. These equations can be reduced to a linear equation with the output state A_{out} for a given input state A_{in} using the transfer matrix M

$$A_{\mathrm{out}} = M \times A_{\mathrm{in}}. \tag{7.7}$$

The input state is given by the input amplitude $a_{m,l}$ either for the spatial channels a_1 and a_2 or the polarisation states a_H and a_V;

$$A = (a_m, a_l)^T. \tag{7.8}$$

The transfer matrix M summarises the conversion from the input to the output depending

on the coupling parameter κ;

$$\kappa = \frac{\pi \tilde{n}_i^3 r_{ij} V \eta}{\lambda G}. \tag{7.9}$$

The coupling parameter scales the interaction between the induced electric field E^{DC} and the supported optical modes $E_{m,l}$ in the waveguide. The overlap η between the applied electric field and spatial modes is given by the overlap integral with a given electrode separation G and applied voltage V;

$$\eta = \frac{G}{V} \frac{\int_A E_m^* E^{\mathrm{DC}} E_l \mathrm{d}A}{\sqrt{\int_A E_m^* E_m \mathrm{d}A \int_A E_l^* E_l \mathrm{d}A}}. \tag{7.10}$$

Electro-optic modulation is additionally scaled by the material parameter r_{ij}. We expect a temperature-dependent change of the coupling since the electro-optic coefficient r_{ij} and the refractive index $\tilde{n}_l$ are temperature dependent [83, 85].

Cryogenic modulation

The coupling parameter κ links the applied electric field and the output state of the modulator. For each modulator, the quantity $\Phi = \kappa L$ can be defined. For the phase modulator, Φ is the phase induced given a bias voltage; $V_\pi/2$ is the voltage required to shift the phase by $\pi/2$. For the directional coupler, Φ describes the "phase" of the power transmission between the two output ports: a change of $\Phi = \pi/2$ is required to modulate the transmission from one output channel to the other. Similarly for the polarisation converter, $\Phi = \pi/2$ is required to transfer power fully from one polarisation mode to the other.

The required voltage for the $\pi/2$-phase shift in each case is determined as the voltage $V_{\pi/2}$. A temperature-dependent decrease of the electro-optic coefficient r_{ij} leads to an increase in the required modulation voltage $V_{\pi/2}$.

The electro-optic tensor element r_{ij} acts with a different magnitude in different orientations of the induced electric field [18, 37]. Different modulator types use different r_{ij} for the modulation in our z-cut lithium niobate waveguides. The induced electric field uses for the modulation for the horizontal polarisation with r_{13}, for the vertical direction with r_{33} and for the coupling from the horizontal to vertical polarisation with r_{24} [45, 197]. The polarisation modulator and the directional coupler use the electro-optic coefficient depending on the incident polarisation. Additionally, the polarisation converter uses the coefficient r_{24} to convert the incident polarisation to the perpendicular polarisation. The electro-optic effect is temperature dependent, and decreases with the decrease of temperature [187]. It is to be determined if the electro-optic coefficient experiences the same change for all three orientations when cooled down from ambient to cryogenic temperatures.

In addition to the temperature change, the coupling parameter κ is inversely proportional to the wavelength λ of operation. To compare a modulator at different operation wavelengths, the operation voltage $V_{\pi/2}$ should be scaled to the operation wavelength.

The thermal contraction is approximately 0.1% in lithium niobate from ambient temperatures to cryogenic temperature [187], therefore, the added change of the output phase Φ due to thermal contraction is negligible with the decrease of temperature.

Temperature-dependent dispersion

All devices depend on modifying the refractive index with an external electric field. Due to dispersion, this refractive index is wavelength and temperature dependent. Understanding this interplay is crucial to build devices that function at a given wavelength under the same operating conditions.

The refractive index of lithium niobate is described by the Sellmeier Equations [85]. We simulated the temperature-dependent dispersion for our waveguide geometry, see Fig. 7.6. To do so, the refractive index profile of the in-diffused titanium is simulated in dependence of the temperature and wavelength with the simulation program RSoft [84]. The refractive index for the vertical polarization TM remains almost unchanged by 0.03% while the refractive index TE changes by 0.3% in a range from 300K to 1K at 1550nm.

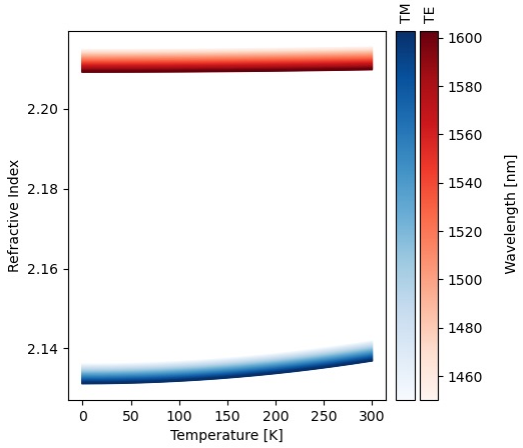

Figure 7.6: Temperature dependent dispersion of the waveguide. The refractive index is extracted from the Sellmeier equations and the simulated titanium diffusion profile is for our in-diffused waveguides.

Fabrication

The modulators are fabricated from congruently grown z-cut lithium niobate wafers and the waveguides are realised by titanium in-diffusion [79]. To do so, a layer of titanium is deposited on the samples top surface. Afterwards, a photoresist is deposited and selectively cured with UV mask lithography or UV laser lithography to structure the sample. Then, the titanium is etched such that a titanium stripe results on the surface along the entire sample length with the values given in figure 7.2. To raise the refractive index in the sample the

titanium stripe is in-diffused. The endfaces of the samples are polished to enable efficient optical coupling. The resulting waveguides achieve losses below 0.15 dB/cm at 1550 nm.

Modulation in the waveguides is induced by an electric field originating from electrodes on the top surface. To fabricate and align the electrodes, a photoresist is structured with UV-lithography. The electrode pairs are separated by a gap G over the full length L of the electrodes with an electrode width w, as given in table 7.1. The direction of the electric field in the waveguide can be chosen by the placement of the electrode either in the vertical direction when placed on the top of the waveguide or in the horizontal direction when placed adjacent to the waveguide [203]. The phase modulator has an electrode placed on the top of the waveguide to generate mainly the electric field vertically in the waveguide and an adjacent ground electrode. The electrodes are placed on top of the waveguides of the coupling region for the directional coupler. The polarisation converter requires a horizontal electric field. Therefore the electrodes are placed symmetrically next to the waveguide. Afterwards the electrode material is sputtered with a buffer layer of SiO_2 to reduce waveguide losses, a Cr layer for adhesion and an Au layer for the electrodes, with the given values in table 7.1. A lift-off process removes the unwanted electrode material and the electrodes are contacted with wirebonds on the top. The chosen fabrication parameters of the modulators are optimised for the operation at ambient temperatures and summarised in table 7.1. The cryogenic operation of these modulators will need additional optimisations in the future since the overlap between the waveguide mode and electric field is likely to change due a temperature dependence in the refractive index and permittivity [83, 85].

The polarisation converter requires an additional periodic poling for phasematching, as described in Sec. 7.2. The waveguides are poled prior to electrode deposition. To do so, a photoresist with the required poling period is structured and liquid electrodes are deposited on the sample surface for biasing. RF voltage pulses invert the material domain under the electrodes, resulting in the required poling period. For our polarisation modulator this period is 19.9 µm.

Type	waveguide		electrode			electrode height		
	Ti width	length	length	gap	width	SiO_2	Cr	Au
unit	µm	mm	mm	µm	µm	nm	nm	nm
Phase modulator	5	22	12	9	100	400	10	300
Directional coupler	7	27	12	6	100	400	10	100
Polarisation converter	6	22	15	15	400	400	10	100

Table 7.1: Summary of the fabrication parameters for the realised modulators.

Electro-Optical Characterisation

We want to determine the voltage, wavelength, and temperature dependence of the three modulators. For the directional coupler and the polarisation modulator we measure the optical intensity in the two different modes while we sweep the bias voltage. These sweeps

are done at different wavelengths of the input laser, and the wavelength sweeps are acquired at ambient and cryogenic temperatures. The phase modulator is characterised with the Sénarmont method [204], where we sweep the voltage at constant wavelengths. This is again done at different wavelengths and at ambient and cryogenic temperatures.

To characterise the modulators, they are placed in a cryostat with windows for in- and outcoupling, as it can be seen in figure 7.7 a), figure 7.8 a), and figure 7.9 a). The light propagates through the sample and is modulated by applying a voltage across the electrodes. For the analysis of the output intensity the light is split by their spatial or polarization modes. The output of the phase modulator and polarisation converter are split with a polarising beam splitter, as it can be seen in figure 7.7 a) and 7.9 a). The output of the directional coupler is collimated and then split spatially with a D-shaped mirror, as it can be seen in figure 7.8 a). The resulting output intensity is then acquired by photodiodes.

The voltage is swept in a range from -60 to 60V. We use a tunable continuous wave laser with a tuning range from 1440 nm to 1640 nm, a linewidth of 1 pm, and an intensity of 1 mW. To avoid changes in the setup, the sample is mounted in the cryostat for the characterisation at both ambient and cryogenic temperatures, as it is summarised in table 7.2.

Type	wavelength [nm]		voltage [V]		temperature [K]	
	range	steps	range	steps	max	min
Phase modulator	1440-1640	2.5	±60	1	296	8.5
Directional coupler	1440-1640	2	±55	0.5	296	5
Polarisation converter	1464-1480	0.2	±60	1	296	
	1578-1590	0.2	±60	1		5

Table 7.2: Parameter range of the wavelength and voltage sweeps. The parameters sweeps are given for all three modulators at ambient and cryogenic temperatures.

Modulators

Phase Modulator

A phase modulator demonstrates the core principle of electro-optic modulation. The modulator changes the refractive index in the waveguide and a tunable propagation delay is induced. This delay can be used to modulate the interference in an integrated Mach-Zehnder-interferometers or the phase between path-entangled states in quantum optics. Electro-optic phase modulators are therefore an essential tool for quantum optic networks [20, 197]. Additionally, a lithium niobate phase modulator has been used to read out superconducting devices at cryogenic temperatures [205].

An electric field induces the change in the refractive index via the electro-optic effect depending on the incident polarisations, as described in section 7.2. The accumulated

phase $\Phi_{(H,V)}$ after the propagation through a waveguide can be described by the transfer matrix for the input in both polarisation modes written in vector form $A_{in} = (a_H, a_V)^T$:

$$M_{\text{Phase}} = \begin{pmatrix} \exp(i\Phi_H) & 0 \\ 0 & \exp(i\Phi_V) \end{pmatrix}. \tag{7.11}$$

The phase at the output of the waveguide due to the electro-optic modulation is then $\Phi_{\text{EO}} = \kappa_{(H,V)}L$, which is described in section 7.2. The coupling parameter is given by the equation 7.9 depending on the polarisation with r_{13} and r_{33} respectively.

The Sénarmont method can read out the phase difference of two polarisation modes by interfering them after the transmission through the sample [206]. Light is coupled equally in the waveguide and modulated by the electric field with an accumulated phase difference

$$\Delta\Phi = \kappa_H L - \kappa_V L. \tag{7.12}$$

The output of both polarisations are then interfered with an quarter waveplate at 45° and a Polarising Beam Splitter (PBS). The intensity I in one arm after the PBS is then described by:

$$I_{1,2} = \frac{1}{2}(1 \pm \sin(\Delta\Phi)). \tag{7.13}$$

The electric field generated by the electrode on the top of the waveguide mainly modulates the phase in the vertical direction and partially in the horizontal direction, due to the horizontal geometry of the electrodes.

A single voltage scan at 1550 nm is shown in figure 7.7 b). We normalised the output of the modulator by the sum of the intensity in both channels of the PBS: $I_{norm} = I_{H,V}/(I_H + I_V)$. The resulting modulation gives the expected *sine*-shape. The modulation voltage $V_{\pi/2}$ is the voltage difference required to modulate the output intensity from a minimum to a maximum. Propagation and coupling losses reduce the intensity of the beams and therefore the visibility of the modulation. Nonetheless, the $V_{\pi/2}$-voltage is unaffected from the induced losses.

The modulation voltage $V_{\pi/2}$ increased from 23.3 V at ambient temperatures to 40 V at cryogenic temperatures. In addition, we extracted the $V_{\pi/2}$ from the wavelength scan at different temperatures as it can be seen in figure 7.7 c). A linear increase of the modulation voltage is observed with the increase of the operation wavelength. A DC-drift in the modulation characteristics was not observed during the characterisation of the modulator over the duration of a day.

The phase modulator was operated successfully at ambient temperatures and at cryogenic temperatures over the full wavelength range from 1440-1640 nm. The modulation voltage $V_{\pi/2}$ increased with the decrease in temperature and increase of the operation wavelength. In this case, the operating temperature was 8.5 K, due to increased electrical heat load in relation to the other tested modulators. We used the Sénarmont method to characterize the phase modulator because this method shows the core principle of the electro-optic

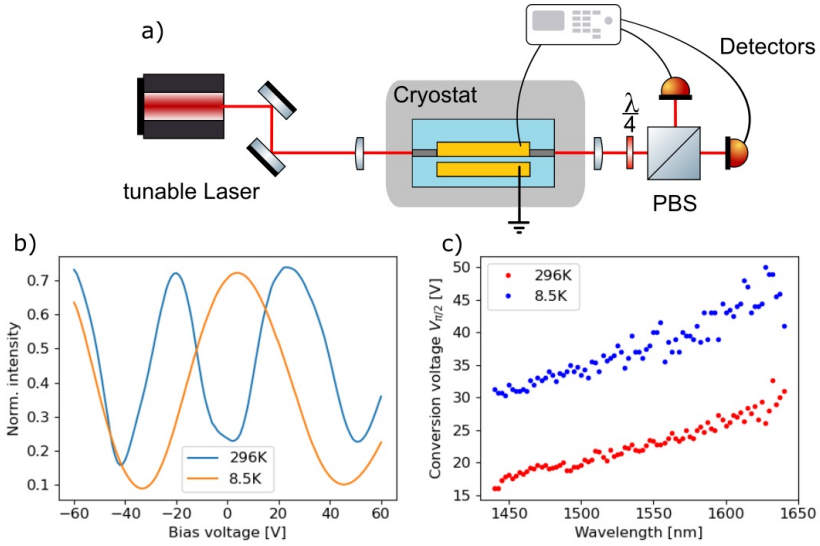

Figure 7.7: a) The electro-optic phase shifter is integrated in a cryostat for optical testing. A tunable laser is coupled in the waveguide. The output characterised with a quarter wave plate and a polarisaing bema splitter (PBS). b) Sweep of the bias bias voltage at 1550 nm. c) Wavelength dependent $V_{\pi/2}$

modulation. Additionally, the method allows us to use only a single input beam. The phase modulator can be used on a single polarisation but a stable reference beam must be used to read out the phase. The resulting modulation voltage will be lower because the phase difference of only one polarisation is read out. Nonetheless, this method for the characterisation shows the principle of the electro-optic modulation at cryogenic temperatures.

Directional coupler

Electro-optic directional couplers are used in integrated photonics to route light between waveguides. This effect is used for the switching of single photons [20] or in macroscopic applications for intensity modulation [207].

Light is guided through a waveguide towards an adjacent waveguide such that the evanescent field of both guided modes overlap. After the interaction, bends divert the waveguides and guide the coupled light apart, as seen in figure 7.8 a). The output of the coupler depends on the propagation in the waveguides, which for symmetric waveguides is described by the propagation constant k.

The electrodes on the top of the waveguides generates a vertical electric field and induces

a phase difference:

$$\beta = \kappa_1 - \kappa_2 = \frac{\pi \tilde{n}_i^3 r_{ij} \eta(+V)}{\lambda G} - \frac{\pi \tilde{n}_i^3 r_{ij} \eta(-V)}{\lambda G} \,. \tag{7.14}$$

Due to the electrode configuration the electric field in both waveguides are orientated in opposing directions. The electro-optic modulation is therefore dependent on the overlap between the spatial mode of the adjacent waveguides $E_{1,2}$ and the induced electric field E^{DC} [203]

$$\eta = 2\frac{G}{V}\frac{\int_A E_1^* E^{DC} E_2 \mathrm{d}A}{\int_A E_1^* E_2 \mathrm{d}A} \tag{7.15}$$

The state of the modulator at a given propagation distance y is described by the transfer matrix for an input state $A_{in} = (a_1, a_2)^T$ for both waveguides [208]

$$M_{\text{directional coupler}} = \begin{pmatrix} \cos(sy) + \frac{i\beta}{2s}\sin(sy) & -\frac{k}{s}\sin(sy) \\ +\frac{k}{s}\sin(sy) & \cos(sy) - \frac{i\beta}{2s}\sin(sy) \end{pmatrix} \tag{7.16}$$

The output state of the directional coupler at $y = L$ is dependent on the switching parameter $s = \sqrt{k^2 + (\beta/2)^2}$. The induced electric field thus changes the propagation in the coupler by changing the switching parameter s.

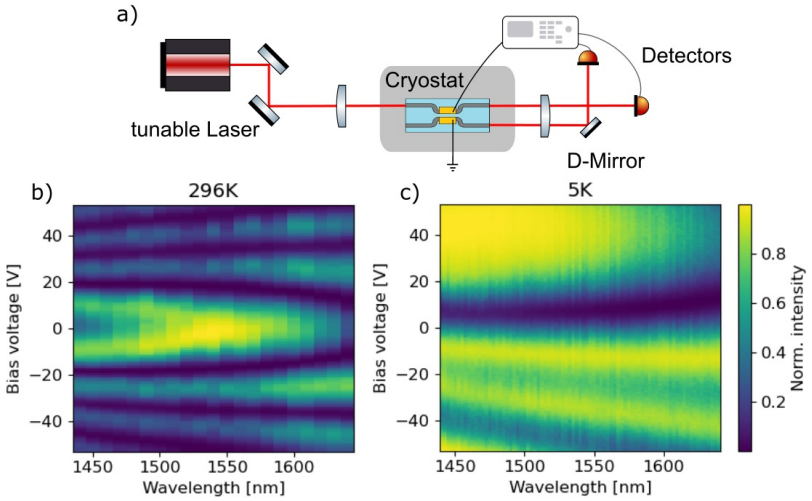

Figure 7.8: a) The coupler is integrated in a cryostat for optical characterisation with a polarized tunable laser and a bias voltage supply. The resulting 2D plot of the wavelength dependent electronic modulation is given at b) room temperature and c) at 5 K. The intensity in the 2D plot is normalized by the sum of both intensities; $I_1/(I_1 + I_2)$

The directional coupler requires a voltage of 18V to couple TM-polarised light from the input waveguide to the adjacent waveguide at 1550nm and ambient temperatures. The $V_{\pi/2}$-voltage increases to about 35V at 1550nm and cryogenic temperatures. The

wavelength-dependent output of the modulator at ambient temperatures resembles the wavelength dependent modulation with a shift of 42V at cryogenic temperatures. This DC-shift could be induced by localised charges in the sample generated during the cooling process due to the pyro-electric effect [37, 187]. The DC-shift remained stationary during the characterisation of the device over the course of more than a day.

Additionally, the comparison of the wavelength-dependent modulation can be determined by comparing the output when the light remains in the same waveguide, known as the bar state. This bar state shifted from 1545 nm at ambient temperatures to 1460 nm at cryogenic temperatures, a shift of 85 nm. The output of the directional coupler is wavelength-dependent since dispersion changes the coupling ratio of the waveguide modes.

Polarisation Converter

Controlling the polarisation on a single photon level is of great interest for quantum optics. Manipulating photonic qubits can be realised by polarisation conversion in combination with frequency conversion [20].

The modulator converts incident light from one polarisation to the orthogonal polarisation using the electro-optic effect. The conversion is inefficient at a given wavelength due to differences in the propagation speeds of the two polarisation modes, since z-cut lithium niobate waveguides are birefringent. The mismatch in propagation speed results in an acquired phase difference $\Delta\beta$. A periodic poling of the crystal axis along the propagation direction can compensate the accumulated phase difference [44, 188]. Therefore, a poling length Λ should be chosen such that

$$\Delta\beta = 2\pi\left(\frac{n_{\mathrm{H}}(\lambda,T) - n_{\mathrm{V}}(\lambda,T)}{\lambda}\right) - \left(\frac{2\pi}{\Lambda}\right) = 0. \tag{7.17}$$

With a designed periodic poling for a given operation wavelength the polarisations couple efficiently. The transfer matrix that describes the polarisation conversion from H to V when operated on a single waveguide with the input $A_{in} = (a_H, a_V)^T$ is given by

$$M_{\mathrm{pol\,conv}} = \begin{pmatrix} \cos(sy) + \frac{i\Delta\beta}{2s}\sin(sy) & -\frac{\kappa}{s}\sin(sy) \\ +\frac{\kappa}{s}\sin(sy) & \cos(sy) - \frac{i\Delta\beta}{2s}\sin(sy) \end{pmatrix} \cdot e^{\frac{i\Delta\beta y}{2}} . \tag{7.18}$$

The coupling strength between the polarisation modes is dependent on the switching parameter $s = \sqrt{\kappa^2 + (\Delta\beta/2)^2}$. Coupling is most efficient at the phasematched wavelength with $\Delta\beta = 0$, such that the switching parameter is equal to electro-optic coupling $s = \kappa$. The coupling parameter κ is given by equation 7.9 with the effective refractive index as the geometric mean $\tilde{n} = (n_H n_V)^{1/2}$ and the electro-optic coefficient r_{24}.

The change of the operation temperatures affects the refractive index of the waveguides such that the phasematched wavelength shifts. The results of the characterisation at 296 K and 5 K can be seen in figure 7.9 b) and c).

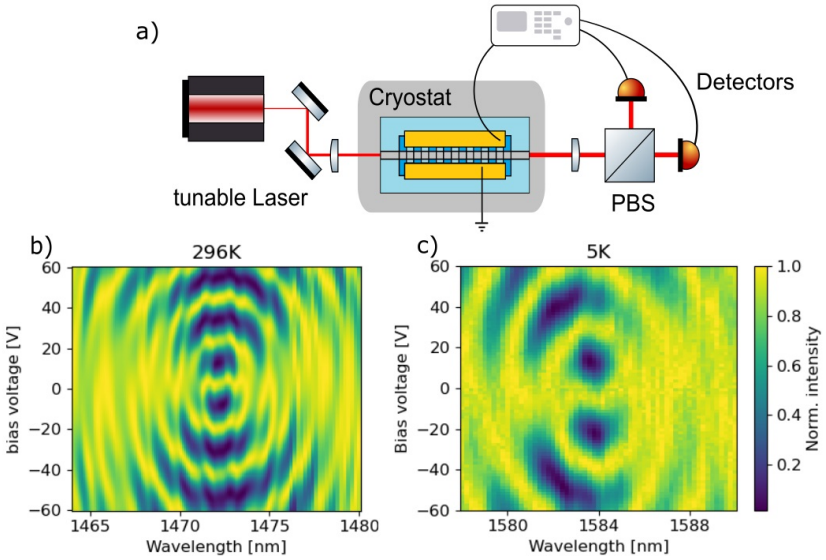

Figure 7.9: a) The coupler is integrated in a cryostat for optical characterisation with an tunable input laser and a bias voltage supply. The resulting 2D-plot of the wavelength dependent electronic modulation is given at room temperature b) and at 5 K c). The intensity is in the plot is normalized by the sum of both intensities. $I_{H,V}/(I_H + I_V)$

The phasematched wavelength of the converter shifted from 1472 nm to 1584 nm for a poling period of 19.9 µm from 295 K to 5 K. The required conversion voltage $V_{\pi/2}$, at the phasematched wavelength, increased from 11.1 V to 16.1 V. The increase in the required conversion voltage is linked to the decrease of the electro-optic coefficient r_{24}. In addition, a DC-offset is present in the range of 2.1 V and remained stationary during the characterisation over more then one day.

The modulation map at cryogenic temperatures resembles closely the shape of the conversion map at ambient temperatures. A wavelength shift of 112 nm, an increase of $V_{\pi/2}$ of 5 V, and a DC-shift of 2.1 V is observed with the decrease of temperature. Additionally, we observed a reduced perturbation of the conversion characteristics in comparison to a previous cryogenic characterisation of a polarisation converter [188].

Device comparison

In summary, we realised three different devices to characterise the electro-optic modulation at cryogenic temperatures. First, a phase modulator inducing a phase difference was characterised with the Sénarmont method. Second, a directional coupler was realised to modulate the routing from one waveguide to the other. Lastly, a polarisation converter was realised to couple light from an incident polarisation to the orthogonal polarisation. This modulator toolbox can be used to realise integrated photonic circuits at cryogenic temper-

atures. We now compare the performance of these modulators at ambient temperatures and cryogenic temperatures.

The required modulation voltage $V_{\pi/2}$ and operation wavelength are summarised in the table 7.3. All modulators showed an increase of the operation voltage $V_{\pi/2}$ at cryogenic temperatures, namely 74% for the phase modulator, 84% for the directional coupler and 35% for the polarisation converter, as shown in table 7.3. Note that the effect of different operating wavelengths and electrode lengths are normalised out in each case. The increase in the modulation voltage can be attributed to the material parameters connected to the modulation strength κ such as the electro-optic coefficient r_{ij} and the mode overlap η. For example, previously the electro-optic coefficient r_{33} has been reported to decrease by ca. 20% for bulk lithium niobate at cryogenic temperatures [83]. This decrease would be equivalent to a voltage increase of 28% for the directional coupler used in this work. The discrepancy with the 85% increase in the $V_{\pi/2}$-voltage which we observe could be due to a reduced overlap between the guided mode and the electric-field at cryogenic temperatures. The overlap can be further optimised by the electrode placement and dimension at cryogenic temperatures. The other modulators use different r_{ij} parameters, however changes to the mode overlap make it difficult to infer changes in this parameters under cryogenic conditions.

	$V_{\pi/2}$ [V]		λ [nm]		$V_{\pi/2}/(\lambda L)$ [$\frac{\mathrm{V}}{\mu\mathrm{m\,cm}}$]	
Type	296K	<8.5K	296K	< 8.5K	296K	< 8.5K
Phase modulator	23.3	40	1440 - 1640		12.4	21.5
Directional coupler	18	35	1460	1545	10.2	18.8
Polarisation converter	11.1	16.1	1472	1584	5	6.73

Table 7.3: Summary of the results from the temperature dependent modulator characterisation. The given wavelengths are the bar state wavelength for the directional coupler and phase matched wavelength for the polarisation converter.

The operation of the directional coupler and polarisation converter showed a DC-shift in the modulation characteristics at cryogenic temperatures. We associate this DC-shift to be generated by pyro-electric charges during the cooling process [37, 187]. These charges are localised in the substrate such that a static electric field is generated. During the cooling process the charges can be discharged and generated, scaled by the charge mobility of the substrate. The charge mobility in lithium niobate decreases at lower temperatures such that the charges are less likely to discharge [187]. The resulting electric field builds up and presents as a DC-shift in the modulation at cryogenic temperatures. This DC-shift remained stable under cryogenic conditions since the charge mobility in the substrate is greatly reduced and additional DC-drifts could be less likely.

The output of the modulators shows a wavelength dependence. To match multiple optical devices the interaction length can be further optimised to achieve the desired output state at cryogenic temperatures. The temperature induced wavelength shift in the unbiased bar state is 84 nm for the directional coupler and 112 nm for the polarisation converter. The

desired operation wavelength can be optimised by either optimising the coupler length and waveguide separation or by optimising the periodic poling. The phase modulator can be operated in the entire wavelength range. Additionally, a wavelength-dependent $V_{\pi/2}$ was determined. The modulation voltage increase is expected to be 14% given the relation: $\kappa \approx 1/\lambda$. However an additional increase by 31% is observed at ambient temperatures and at cryogenic temperatures. The wavelength dependent increase could be linked to a reduced overlap between the optical mode and induced electric field.

Conclusion

We successfully realised a toolbox for light manipulation for integrated optics at cryogenic temperatures. The modulators are fabricated with titanium in-diffused z-cut lithium niobate waveguides. We fabricated and characterised a phase modulator, directional coupler and polarisation converter and investigated changes in the electro-optic effect at cryogenic temperatures. The modulation voltage $V_{\pi/2}$ increases with the decrease of temperature for all three modulators, and can be optimised further for these devices by optimising the overlap between the optical modes and induced electric field. Future characterisation can focus on a reduction of pyro-electricity during the cooling process.

The future goal for the cryogenic modulators is the integration with SNSPDs. Integrated SNSPDs have been shown before with system detection efficiencies of about 1% for in-diffused waveguides and thin lithium niobate at 46 % [34, 35, 58, 61, 121]. The evanescent coupling from the waveguides to the detectors may need further improvements depending on the desired application. Additionally, feed-forward applications could be realised by the combined integration. An impinging on the SNSPD generates an electronic signal which modulates light in the integrated electro-optic modulator. The amplitude of the detection signals is in the range of a few millivolts while the modulation voltage $V_{\pi/2}$ is above 16 V at cryogenic temperatures. Additional amplifiers are then needed to generate a strong optical modulation based on a single photon click. This characterisation of the electro-optic modulator is a step forwards towards the combined operation of integrated detectors and modulators at cryogenic temperatures.

Funding

Bundesministerium für Bildung und Forschung (13N14911); European Research Council (725366)

7.3 Opto-electronic bias of a superconducting nanowire single photon detector using a cryogenic photodiode

Frederik Thiele[1], Thomas Hummel[1], Maximilian Protte[1] and Tim J. Bartley[1]

[1] Physics Department, Paderborn University, Paderborn 33098, Germany

Publication:
"Opto-electronic bias of a superconducting nanowire single photon detector using a cryogenic photodiode," APL Photonics, vol. 7, no. 8, p. 081303, Aug. 2022.
https://doi.org/10.1063/5.0097506

Abstract

Superconducting Nanowire Single Photon Detectors (SNSPDs) have become an integral part of quantum optics in recent years because of their high performance in single photon detection. We present a method to replace the electrical input by supplying the required bias current via the photocurrent of a photodiode situated on the cold stage of the cryostat. Light is guided to the bias photodiode through an optical fibre, which enables a lower thermal conduction and galvanic isolation between room temperature and the cold stage. We show that an off-the-shelf InGaAs-InP photodiode exhibits a responsivity of at least 0.55 A/W at 0.8 K. Using this device to bias an SNSPD, we characterise the count rate dependent on the optical power incident on the photodiode. This configuration of the SNSPD and photodiode shows an expected plateau in the single photon count rate with an optical bias power on the photodiode above 6.8 µW. Furthermore, we compare the same detector under both optical and electrical bias, and show there is no significant changes in performance. This has the advantage of avoiding an electrical input cable, which reduces the latent heat load by a factor of 100, and in principle allows for low loss RF current supply at the cold stage.

Exploiting the nonclassical properties of light can enable and improve various tasks in communication [189], computing [4], and metrology [190, 191]. These applications require high detection efficiencies for the carefully generated and manipulated quantum states of light [32]. Superconducting Nanowire Single Photon Detectors (SNSPDs) are state-of-the-art single photon detectors, achieving efficiencies above 98% [11], low timing jitter [177], and low dark count rates [14].

As the size and complexity of quantum optics experiments increases, so does the need for ever more detectors. One of the limits of scaling superconducting detector systems is the heat load and electrical noise of the in- and output connections from ambient temperatures to the SNSPDs in a cryostat [90, 209]. This problem is not limited to SNSPDs: many quantum technologies require electronic control in a cryogenic environment [123]. Providing the electrical bias, control and readout through an optical connection could reduce these restrictions significantly [123, 131]. Recently, optical readout of a superconducting detector

has been shown with an integrated electro-optic modulator [51, 58, 59, 147]. However, a complete optical operation, namely bias and readout, of an SNSPD still lacks an optically driven current source.

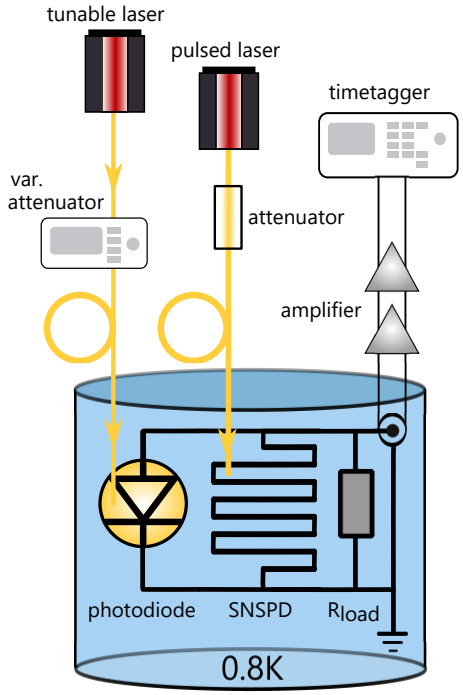

Figure 7.10: A photodiode is illuminated by the tunable laser and provides the current for a superconducting nanowire single photon detector (SNSPD). A second laser triggers the SNSPD with attenuated optical pulses and the signal is transmitted electronically through the amplifiers to the timetagger.

The state of the art for the bias of an SNSPD is a regulated current source with a coaxial cable connection. Optical connections with a photodiode can be more heat efficient than a coaxial cable between ambient temperatures and the cold stage of the cryostat if the required optical power is lower than the induced heat load from the coaxial cable [59, 123]. The fibre connection also enables a galvanic isolation towards the cold stage [123], independent of the heat load of the photodiode. The isolation yields the benefit of an intrinsic RF-noise decoupling, isolation from ground loops within the cryostat and decoupling from thermal input noise.

Critical to this approach are functional photodiodes at cryogenic temperatures. Previously, the characterisation of photodiodes has been reported at temperatures around 4 K [118, 129, 130]. In particular, InGaAs-InP photodiodes have been operated in conjunction with superconducting circuits such as Josephson Junctions [28, 128–130] and transmon qubits [131].

In this paper we present the optical bias of an SNSPD with the photocurrent of a cryogenic photodiode. The photodiode acts as an optical to electronic power converter and can be

regarded as a local current source at the cold stage of the cryostat. The paper is organised as follows. First, we characterise an off-the-shelf InGaAs-InP photodiode to determine its performance as a cryogenic current source. The photodiode converts the optical power of a laser through an optical fibre at the cold stage of the cryostat, as it can be seen in figure 7.10. Second, we show how this can be used to bias the SNSPD, and compare the performance with a standard electrical bias connection. Finally, we give an outlook on future improvements and applications.

Cryogenic current source

The principle of operation of an SNSPD is based on the photon-induced breakdown of superconductivity in a thin and narrow wire. The wire is electrically biased close to its critical current, such that the absorption of at least one photon is sufficient to make the wire normally conductive and a voltage pulse can be read out. Depending on their material and geometry, SNSPDs typically require a bias current in the range 1-50 µA [16]. In our implementation, this is provided by the photocurrent of an off-the-shelf photodiode from Marktech (MTPD1346D-010). To that end, we first characterize the performance of the photodiode under cryogenic conditions. For a photodiode in shunted operation, the conversion ratio from an optical input power P to a photocurrent I is described by the responsivity $\mathcal{R}(\lambda) = I/P(\lambda)$. The conversion depends on the active material and operation wavelength λ. We characterise the responsivity of an off-the-shelf InGaAs-InP photodiode depending on the wavelength and temperature. To do so, the photodiode is mounted in a cryostat and a single mode fibre illuminates it from above. A tunable contiuous-wave laser provides a power of 1 mW into the fibre and an ampere meter reads out the photocurrent generated by the photodiode through a coaxial cable, as it can be seen in figure 7.11. While cooling down the photodiode from ambient temperatures to 0.8K, the illumination wavelength is swept in a range from 1440-1640 nm in 2 nm steps and the generated photocurrent is measured. The acquired responsivity is displayed in figure 7.11 b).

The photodiode achieves a responsivity of about 0.65 A/W at ambient temperatures at 1540 nm, as it can be seen in figure 7.11 b). Over the entire temperature range, the responsivity is maintained over a wavelength range of 1440 nm to 1540 nm. A responsivity of 0.55 A/W is measured at 1540 nm at a stable operation temperature of 0.8 K. In contrast, the responsivity of the photodiode is reduced over a wavelength range of 1540-1640 nm below a temperature of 150 K. This is explained by the temperature-dependent bandgap of InGaAs-InP with the Varshni model [132] and has been reported previously [129]. The temperature dependence of the band gap cannot be directly extracted from this data set because the temperature sensors for the cold stage of the cryostat are not precisely calibrated in the range from 270-20 K.

The bias current for an SNSPD needs to be adjusted to generate photocurrents below the critical current. Therefore, we need to determine the photocurrent depending on the input power over a sufficient range to accurately set the desired bias current. To do this we insert

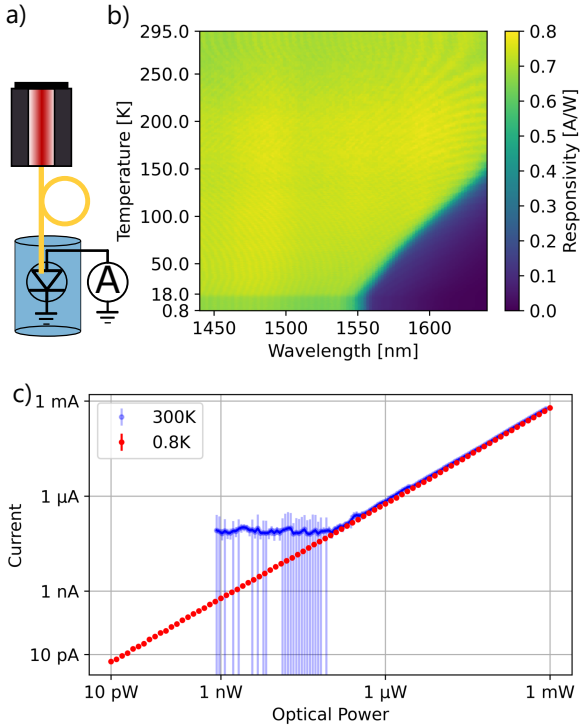

Figure 7.11: a) A tunable laser illuminates the photodiode in the cryostat and the photocurrent is read out with an ammeter. b) The responsivity of the photodiode depends on the wavelength and temperature. c) The photocurrent is read out dependent on the optical power. Error bars are plotted for both measurements and become smaller than the marker of the data point at higher powers. At room temperature and low optical power, the uncertainty is dominated by dark current with an average of 75 nA, which can take negative values and therefore results in large lower error bars on the log scale.

a variable attenuator to limit the optical power on the photodiode while the laser is operated at stable power output at 2 mW with a wavelength of 1540 nm. The illumination power of the photodiode is varied in 0.25 dB steps, the current is read out with a picoammeter and the results are shown in figure 7.11 c). The photodiode shows a linear dependence in the responsivity in the range from 1 mW to 100 nW at room temperature and 1 mW to 10 pW at cryogenic temperatures. The photodiode is not responsive for lower input powers because the dark current is larger then the generated photocurrent. The photodiode has a significantly larger dynamic range at cryogenic temperatures since the dark current is reduced with the decrease in temperature. The upper limit of the characterization is 1 mW so as not to exceed the heat load limit of the cryostat, given by the manufacturer.

In summary, the responsivity of the photodiode decreases slightly to 0.55 A/W at cryogenic temperatures, however the linear dependence between the input power and photocurrent is maintained. The photodiode can provide the bias current for an SNSPD of about 5 µA

with 8 µW of input power, which does not surpass the heat load limit of the cryostat of about 1 mW at 0.8 K. The photodiode is characterised in shunted operation, since the superconducting meander of the SNSPD shunts the circuit. We additionally characterised the load capabilities of the photodiode at 0.8 K in section 7.3, in which we show that the generated photocurrent is not suppressed by the typical circuit loads with these optical input intensities at 0.8 K.

Comparison between photocurrent bias and conventional bias

We realise the current bias of the SNSPD with a photocurrent generated by a photodiode located at the cold stage of the cryostat to show the proof of principle of the the concept. We compare the performance with a conventional bias via a current source at ambient temperatures. Both biasing methods are realised with the same SNSPD, during separate cooldowns of the cryostat. The fabrication parameters of the SNSPD follow those from Marsili et al. [210]. We specifically, compare the voltage response of the click signal, the count rate dependent on the bias, the derived System Detection Efficiency (SDE) and the timing jitter.

The photocurrent bias is realised by connecting the photodiode, SNSPD and a 50 Ω resistor in parallel at the cold stage of the cryostat, as schematically shown in figure 7.10. The photodiode is illuminated through an optical fibre with a laser emitting at 1530 nm. An optical power of 6.7 µW is transmitted onto photodiode, resulting in a bias current of 5 µA. The cold stage of the cryostat reached a stable temperature at 0.8 K. The SNSPD generates click signals which are transmitted through coaxial cables and amplified further with two room temperature amplifiers (Mini-Circuit ZKL-2R5+). The resulting signal is displayed in figure 7.12 (blue) with an amplitude of 50 mV, a rise time of 2.5 ns, and a fall time of 100 ns. The detected click events show the proof-of-principle for optically biasing an SNSPD.

The conventional bias is realised with the same SNSPD using a single commercial biasing and readout circuit at room temperature (Photonspot) consisting of a constant current source, integrated amplifier, and a 50 Ω shunt resistor. The resulting click signal of the current bias is depicted in figure 7.12 (orange) with a bias current of 5 µA, an amplitude of 120 mV and a fall time of 100 ns. Both click signals have a similar shape and only deviate in their amplitude due to the use of different amplifiers. For further performance analysis, the click signals are acquired with a timetagger with a threshold height at 50% of the maximum peak height.

The bias-dependent count rate of the SNSPD is investigated to compare the detection efficiency of both biasing methods. To do so, the timetagger detects the click signals of the SNSPD and acquires a count rate for both biasing methods. A pulsed laser with a repetition rate of 400 kHz, wavelength of 1550 nm, and attenuated to a mean photon number of approximately 2 photons per pulse is used to illuminate the SNSPD. The resulting bias dependent count rate is given in figure 7.13 a) for the photocurrent bias and b) the conventional bias. Both biasing methods show a similar dependence between the count

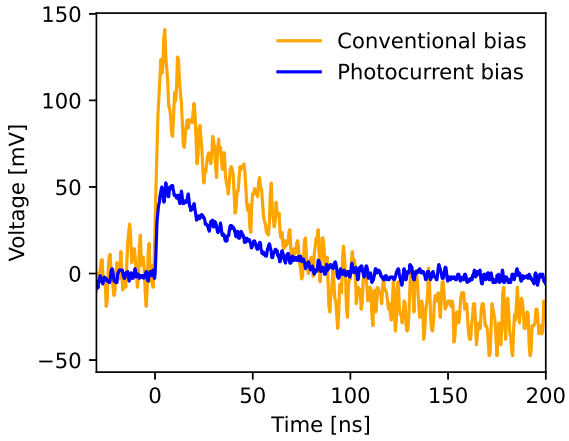

Figure 7.12: Oscilloscope traces of the amplified click signals with a photocurrent bias (blue) and a conventional bias (orange).

rate and the applied bias, following a sigmoidal function. To compare the response of each device, the click rate of the SNSPD is compared at the point of inflection in the System Detection Efficiency (SDE) which is common in both bias dependent count rate distributions and highlighted in figure 7.13. At this point of inflection the photocurrent bias reached a Photon Count Rate (PCR) of 256 kcps and a Dark Count Rate (DCR) of 12.2 kcps. In comparison, the conventional bias reached a PCR of 251 kcps and a DCR of below 1 kcps. Both biasing methods reach a similar signal count rate but the DCR increases under the photocurrent bias.

The increase in the DCR can be attributed to additional photons from the photodiode illumination being scattered onto the SNSPD. To investigate the scattering, we illuminate the photodiode with a power equal to the 90% of the critical bias at 6.8 µA, but we bias the SNSPD with the conventional bias. The dark count rate is investigated here at the 90% of the maximum bias because this is closer to the point of typical operation. The resulting DCR with this conventional current bias reaches a count rate of 31 kcps. This is higher than the DCR at the point of inflection of the SDE due to the increased bias.

The bias dependent count rate shows different behaviour for each biasing method beyond the count rate plateau, as it can be seen in figure 7.13. Under the conventional bias of the SNSPD, no counts beyond a bias current of 5.6 µA are measured, which is indicative of latching. At bias currents beyond this point, absorbed photons generate a hotspot from which the SNSPD cannot reset, therefore no additional click signals are registered.

However, under photocurrent bias, the count rate increases significantly for an optical bias power of 7.6 µW, see figure 7.13 a). Individual traces are generated in the range from 7.6-11.6 µW which are acquired by the time tagger. We attribute this to latching and self-resetting dynamics [101, 211]: The provided photocurrent in the SNSPD could surpass the critical current in the meander in this regime and therefore induce a hotspot. The

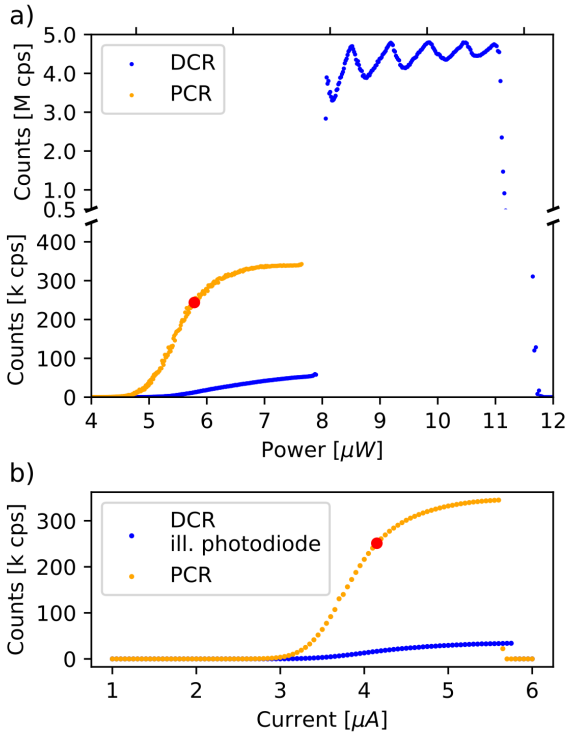

Figure 7.13: Bias dependent Photon Count Rate (PCR) and Dark Count Rate (DCR) of the SNSPD with pulse laser with repetition rate of 400 kHz. a) The bias power on the photodiode is varied with a variable attenuator. The click signals are distinguishable from self oscillation up to 7.6 µW. The y-axis is broken to depict the acquired high count rates from the self oscillation beyond a bias of 7.6 µW. b) The bias for the SNSPD is provided with a constant current source. The SNSPD latches beyond 5.6 µA. The point of inflection of the SDE is highlighted in a) and b) by a red dot.

50 Ω shunt resistor placed directly at the SNSPD redirects the current such that hotspot resets. This process then repeats. In contrast, in the conventional bias method, the added coaxial connection to the shunt resistor at room temperature delays the current redirection, meaning the hotspot cannot reset and the meander remains resistive. In other words, the propagation delay of the coaxial cable alters the resetting behaviour and the SNSPD latches.

The count rate of the SNSPD reaches a plateau for the optical and electrical biasing method above a bias with 90% of the maximal bias. We derive the system detection efficiency (SDE) by comparing the count rate of the SNSPD with a calibrated detector with the same input of the mean photon number. The mean photon number $\bar{n}$ is calculated by the Photon Count Rate (PCR) for a given repetition rate RR of the attenuated excitement laser with a detection efficiency η of the click detector [212];

$$\bar{n} = -\log\left(1 - \frac{\mathrm{PCR}}{\mathrm{RR}}\right)\frac{1}{\eta}. \tag{7.19}$$

A calibrated detector with a detection efficiency of 83±5% is used to set a mean photon number of 2.2 ± 0.13 for the photocurrent bias and 2.4 ± 0.14 for the conventional bias. The resulting SDE dependent on the bias is shown in figure 7.14. The SDE should be independent of the current source since only a constant current is supplied to the SNSPD. To compare biasing methods in respect to their SDE, we normalise the bias to the point of inflection of a sigmoidal function. The point of inflection for the conventional bias is at 4.2 µA, and at 5.8 µW for the photocurrent bias while having a maximum SDE of 79.3±5% and 82.5±5% respectively.

An additional potential difference between the cold stage of the cryostat and the ambient temperature is measured without any applied bias. The offset current is in the order of 700±100 nA which must be accounted for when calculating the bias current. This potential difference could be induced by thermo-electric voltage induced by different temperatures and connections as well as noise pickup of the coldstage [122]. In contrast, the photodiode bias is immune to the potential difference since the load resistor and SNSPD are on the same potential. Nonetheless, the normalised system detection efficiency overlap for both biasing schemes with the offset current compensated as shown in figure 7.14.

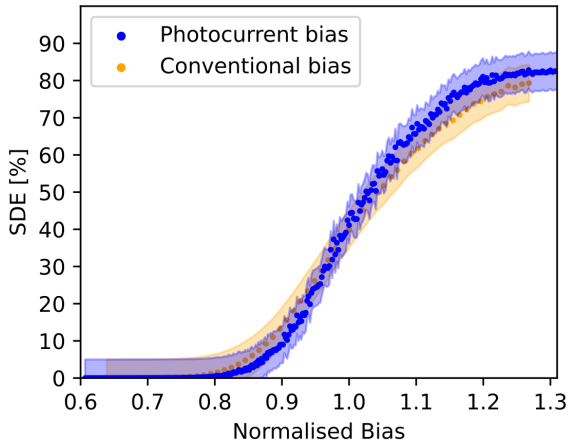

Figure 7.14: System Detection Efficinecy (SDE) dependent on the photocurrent bias (blue) and conventional bias (orange). The bias is normalised to the point of inflection of the SDE. The point of inflection is at 4.2 µA and 5.8 µW, respectively. An additional offset-current is present in the system of about 700±100 nA. The orange and blue band show the error due to this offset compensation and the error in the detection efficiency. The SDE is here derived for a given mean photon number with equation 7.19.

The plateau in the detection efficiency for the photocurrent bias is extended in comparison to the conventional bias. The increased plateau length could originate from an improved current stability with the photocurrent bias. The photodiode generates the bias current in close proximity to the SNSPD and could be more immune to noise pickup of the cables in the cryostat.

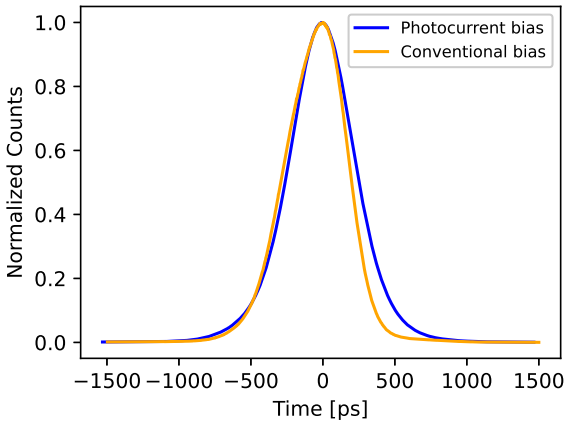

Figure 7.15: Timing jitter of the of the SNSPD with a 50 ps pulsed laser. The SNSPD is biased with a photocurrent bias (blue) and a conventional bias (orange).

One of the many benefits of SNSPDs is their low timing jitter of the detection signal. The jitter should not be influenced by the biasing method as long as a constant current is supplied to the SNSPD. To verify this, we compare the system timing jitter in both biasing regimes. To do so, we use an attenuated pulsed laser with a repetition rate of 625 kHz and a pulse width below 1 ps at a centre wavelength 1545 nm to excite the SNSPD. In the characterisation a bias point at 90% of the maximum bias (6.8 µW and 5 µA) is chosen. The resulting histogram of the photocurrent bias (blue) and conventional current bias (orange) shows in figure 7.15 the jitter in the timing delay between a trigger signal of the optical input pulse and a generated click signal of the SNSPD. The distribution of the timing delay for the photocurrent bias has a Full Width Half Maximum (FWHM) of 513±3 ps. In comparison, the conventional current bias has a FWHM of 495±3 ps. The FWHM of the timing jitter of both methods agree within a few percent relative error. A small difference can arise from a difference in the bias set point. The SNSPD was biased at 90% of the maximum bias which deviates from comparison of the point of inflection because of the difference in the plateau length. Hence, the jitter was acquired at different relative bias points. This mismatch in the relative bias leads to a change in the bias dependent width in the jitter distribution which has been previously reported [177, 213–215]. Additionally, the conventional bias and the photocurrent bias schemes use different amplifiers to detect the click signals. A single commercial amplifier is used in the conventional bias scheme and two chained amplifiers are used in the photocurrent bias scheme. The chained amplifiers can introduce and amplify additional thermal noise such that additional jitter is added in the system. Nevertheless, both methods show no significant deviation in the overall system jitter.

Conclusion and Outlook

We successfully biased an SNSPD with the photocurrent of a photodiode at cryogenic temperatures. This method enables us to optically bias an SNSPD and replace the electrical input connection with a light source, photodiode, and optical fibre. The used photodiode was characterized at cryogenic temperatures and showed a responsivity of at least 0.55 A/W. The optical bias with the photodiode reached a plateau at a bias power of 6.8 µW. In comparison to a constant current bias no significant reduction in the detector performance was observed in terms of the system detection efficiency and timing jitter. The dark counts increased slightly, which is wholly attributable to photons leaking from the optical bias.

Connecting an SNSPD directly from room temperature to a cold stage, the thermal heat load is in the few miliwatt range [122, 123]. Thermal anchors can reduce the effective heat load for the coldstage by absorbing the heat at intermediate stages. In comparison, a single mode fibre can be added from ambient temperatures to the coldstage directly since minimal heat is conducted through the fibre. This reduces the latent heatload by a factor of 100 compared with coaxial cable [51, 59].

The optical bias of the SNSPD shows further possibilities of improvements and applications. The dark count rate of the SNSPD can be decreased by improved shielding of the bias light. The optical input of the SNSPD can be also combined with an electro-optical modulator[51, 58, 59, 147] to achieve pure optical operation of an SNSPD. This removes the constraint of using any coaxial cable between room temperature and the cryogenic environment reducing the heat load further [59, 123] and achieve galvanic isolation [123]. Extending this scheme, an optically pulsed photodiode would enable a simple method for bias current pulsing. Since the bandwidth would be limited by the photodiode, bandwidths exceeding 10 GHz [118] under cryogenic conditions are feasible. This method can be investigated further to gate the detection of an SNSPD.

Supplementary Material

See supplementary material for the load characterisation of the photodiode at 0.8 K.

Acknowledgements

Bundesministerium für Bildung und Forschung (13N14911); We thank Varun Verma (NIST) for providing the superconducting films for the Superconducting Nanowire Single Photon Detectors.

7.4 All optical operation of a superconducting photonic interface

Frederik Thiele[1], Thomas Hummel[1], Adam N. McCaughan[1], Julian Brockmeier[1], Maximilian Protte[1], Victor Quiring[1], Sebastian Lengeling[1], Christof Eigner[1], Christine Silberhorn[1] and Tim J. Bartley[1]

[1]Institute for Photonic Quantum Systems, Paderborn University, Warburger Str. 100, Paderborn, Germany
[2]National Institute of Standards and Technology, 325 Broadway, Boulder, CO, USA, 80305

Publication:
"All optical operation of a superconducting photonic interface," arxiv:2302.12123, Feb. 2023.
`https://arxiv.org/abs/2302.12123`

Abstract

Quantum photonic processing via electro-optic components typically requires electronic links across different operation environments, especially when interfacing cryogenic components such as superconducting single photon detectors with room-temperature control and readout electronics. However, readout and driving electronics can introduce detrimental parasitic effects. Here we show an all-optical control and readout of a superconducting nanowire single photon detector (SNSPD), completely electrically decoupled from room temperature electronics. We provide the operation power for the superconducting detector via a cryogenic photodiode, and readout single photon detection signals via a cryogenic electro-optic modulator in the same cryostat. This method opens the possibility for control and readout of superconducting circuits, and feedforward for photonic quantum computing.

Introduction

Integrated quantum photonics offers great benefits for quantum information processing and communication [9, 10, 216]. With an increasing complexity of quantum photonic applications, a plurality of electro-optic components must be operated on a single chip [32, 90, 217]. These electro-optic components, such as modulators and single photon detectors, require additional ancillary electronic components for biasing, amplification, and signal transmission. Intermediate electric components will degrade the performance of the entire photonic setup by introducing noise, heatload, or bandwidth limitations [123]. To circumvent this, it may be highly beneficial to replace the intermediate electronic connections with optical links, which electrically decouple the photonic processor and the driving electronics.

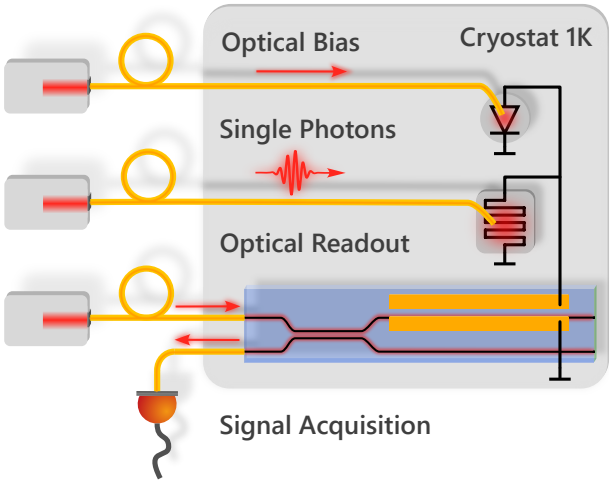

Figure 7.16: Layout of the all-optical operation of a Superconducting Nanowire Single Photon Detector (SNSPD). The cryogenic photodiode is illuminated and generates a photocurrent. When a photon impinges on the SNSPD it becomes resistive and voltage is created. To readout the detection signal, the voltage pulse is transmitted onto the cryogenic modulator. An intensity modulation is then readout at room temperature by a photodiode and timetagger.

Superconducting nanowire single photon detectors (SNSPDs) are a key enabling technology for quantum optical applications due to their near unity detection efficiencies [11, 12], low timing jitter [13], and low dark count rates [14]. Integrating these detectors in advanced photonic circuits is non-trivial since SNSPDs require operation temperatures below 4 K [88]. The cryogenic environment introduces additional challenges when interfacing the detectors with other electro-optic components. The output voltage of the SNSPD is around 1 mV [88] in the typical configuration with a 50 Ω shunt resistor. Therefore, additional electrical components are needed to amplify and transmit the SNSPD signal to the readout electronics. In the typical configuration the readout and bias electronics are outside the cryostat, requiring electrical interconnects between the cryogenic and room temperature environments. Replacing these electrical interconnects with electro-optic components and optical fibers enables electronic decoupling of the cryogenic electro-photonics from the external environment. An all-optical interconnect for superconducting photonics must therefore deliver the operation power and transmit signals to and from the decoupled circuit.

In recent years, cryogenic electro-optic modulation has been investigated for photonic circuits across a variety of platforms [48, 51, 55, 58, 218, 219]. In particular, the electro-optic readout of superconducting single photon detectors both with and without intermediate amplifiers have been investigated [51, 59, 147]. In these applications, the click signal of an SNSPD detection event is delivered to an electro-optic modulator, modulating an optical throughput which is subsequently read out at room temperature. The operation voltage for intensity modulators have been reported to be in a range from 100 mV to 10 V at cryogenic

temperatures [48, 51, 58, 219]. Bridging the gap between the low amplitude output of the superconducting detector to these voltages is non-trivial in a cryogenic environment.

In this paper, we present an alternative method to generate larger detection signals from an SNSPD, which drives an electro-optic modulator directly, to achieve an all-optical readout. The SNSPD works on the principle that a bias current is converted to a voltage signal through a resistive load. This resistive load is created by an impinging photon which breaks the superconductive state in the nanowire, followed by Joule heating creating a so-called hotspot. In a typical operation, a shunt resistor is introduced to redirect the bias current following a detection event. This prevents further Joule heating, allowing the nanowire to dissipate the heat from the hotspot and return to the superconductive state. In our configuration, shown in Fig. 7.16, we omit the shunt resistor allowing the resistive hotspot to grow to larger resistances due to self-heating. This method can generate resistances in the order of a few tens of kΩ such that a signal voltage of 30 mV is created. This is a significant increase compared to the 1 mVsignal from the conventional method. Nevertheless, in our configuration, the SNSPD remains "latched" in its normally resistive state, i.e. the hotspot does not have the ability to reset itself. Indeed, the latching dynamics and resulting output voltage of a nanowire is a largely unexploited effect [159, 220].

A key aspect of our method is the ability to actively reset the hotspot, ideally with a cryogenic current source. We achieve this by modulating the bias current optically with a current generated by a photodiode [221]. We have previously shown that this method shows no significant deviation from conventional biasing [131, 221]. Thus the photodiode power delivery approach combines the key aspects of providing a bias current for the SNSPD and generating the electrical driving power of the modulator. This versatility in generating the SNSPD bias, sustaining the hotspot, and supplying the supply for the electro-optical modulation enables all-optical operation of the SNSPD.

Methods

Once a photon impinges on the nanowire, a hotspot is formed and the electrical power is converted to heat by the resistive nanowire through Joule heating, as depicted schematically in Fig. 7.17 a). This Joule heating results in heating of adjacent superconductive regions, increasing the hotspot size. The resistive region of the nanowire grows until the electrical power provided is equal to the power dissipated due to the temperature difference between the nanowire and the substrate [99, 101]. At the power equilibrium the maximum output voltage is reached, generated by the current flowing trough the resistive nanowire. The output voltage of the latched SNSPD is therefore dependent on the power dissipation of the SNSPD and the electrical power provided by the photodiode. The key to achieve the photodiode bias is to use a diode material which is still responsive at cryogenic temperature which has been investigated for our off-the-shelf photodiodes by [118, 130, 221]. In addition to these investigation in the conventional optical bias of an SNSPD, we characterise the power conversion capabilities and the output voltage of the photodiode in combination with the SNSPD.

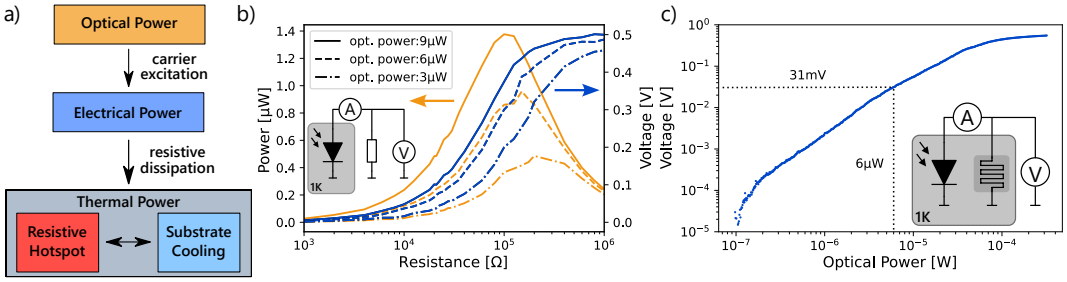

Figure 7.17: a) The optical input power is converted by the photodiode to an electrical power which is then converted to heat by Joule heating. b) Voltage and power output of the cryogenic photodiode under different illumination powers and load resistances. The photodiode is illuminated with a cw-laser at 1530 nmand operated at 1 K. c) Voltage output of the combined operation of the SNSPD and bias photodiode, under different illumination powers to the bias photodiode at 1530 nm.

Optical power supply

The optical to electrical conversion efficiency of the photodiode depends on the load resistance, in our case the SNSPD. The Superconducting detector is fabricated from a tungsten silicide nanowire (WSi) thin-film [222] and has been characterised in the bias dependent detection efficiency to up to 83% ± 5% by Thiele et al. [221]. The SNSPD resistance can vary from no resistance when superconducting to a normal resistance of 5.5 MΩ when the entire nanowire is normally resistive. To determine the generated voltages and dissipated powers, we cooled the photodiode down to 1 Kand attached different load resistors at room temperature according to the inset in Fig. 7.17 b). The photodiode is illuminated through a single mode fibre. To do so, we aligned the fibre perpendicular to the active area of the photodiode. The fibres position is optimised by maximising the converted current while light is transmitted through the fibre. The fibres position is then permanently fixed in place by a UV-adhesive. The photodiode is then operated at an optical input power of about 6 µW. At this input power, a nominal bias current of 4 µA for the SNSPD is generated in shunted operation, given that the responsivity of the photodiode is approximately 0.65 A/W [221].

In our characterisation, we keep the input power stable and vary the load resistor in a range from 10 Ω to 1 MΩ, while measuring the current through and voltage over the resistor. As a result, we generate increasing output voltages by increasing the load resistors, until the output voltage saturates at approximately 500 mV, as can be seen in Fig. 7.17 b). The generated electrical power reaches a maximum power point at a resistance around 100 kΩ, before reducing again for higher loads due to a reduction in the generated current. This maximum power point shifts to lower resistances when the optical power on the photodiode is increased. This load characterisation shows that the cryogenic photodiode can provide a bias current in the shunted operation when the nanowire is superconductive and a voltage beyond 500 mVwhen a resistive hotspot is created.

The hotspot in the nanowire is not a static resistor and is expected to change in size depending on the electrical supply power. Therefore, the output voltage will depend on the optical input power of the photodiode. However, we cannot increase the input power to the photodiode indefinitely to generate a maximal optical response because the SNSPD must be operated at a nominal bias current of 4 µA. Therefore, we need to determine the voltage at this operation point when combining the SNSPD directly with the photodiode. To characterize the devices before the all-optical demonstration, we combined both devices on a single stage in the cryostat at 1K and read out the output voltage at different input powers the photodiode, as shown in the inset of Fig. 7.17 c). Both devices are connected with a coax cable to measure the voltages at room temperature. Fig. 7.17 c) shows that voltages with the photodiode and SNSPD are generated and saturate above approximately 550 mVwhen we sweep the input power from 0.1 µW to 700 µW. In the all-optical operation of the SNSPD, we provide an input power of 6 µWto generate the nominal bias current for the SNSPD. At this power level a output voltage of 31 mVis reached, generated by a 40 kΩ nanowire resistance. This output voltage is a significant increase in relation to a click signal of below 1 mVin the conventional method.

Electro-optic readout

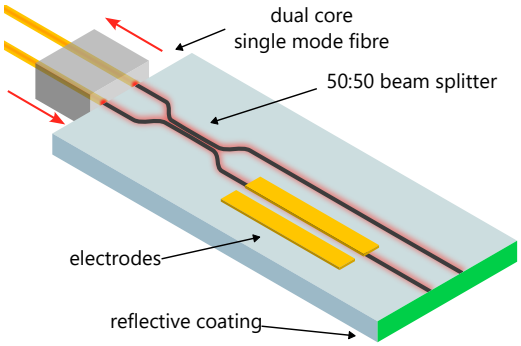

Figure 7.18: Layout of the Michelson-interferometer realised in a photonic circuit. A dual core single mode fibre pigtail couples light into the waveguides and returns the reflected light for the readout. These waveguides are fabricated by titanium indiffusion in z-cut lithium niobate. An integrated beam splitter splits the input light into two paths which are then reflected at the endface to interfere again at the beamsplitter. Electrodes on the surface of one beam arm introduce a phase difference when a voltage is applied. b) Voltage sweeps of the modulators at 1530 nm. The measured intensities are normalised to the maximal out power per sweep. The V_π voltage voltages are 5.9 Vat 1 Kand 6.6 Vat 300 K. The V_π voltage is acquired by fitting a sin-function to the acquired data.

The readout of the generated click signal is realised by modulating the intensity with an electro-optic modulator operated at cryogenic temperatures. We choose a titanium in-diffused lithium niobate electro-optic modulator because of its proven operation at cryogenic temperatures [218, 219]. Furthermore, we can achieve fibre-to-fibre optical

coupling up to 43% with single mode fibres even at 1 K [218]. We implement an integrated Michelson interferometer consisting of a directional coupler, a reflective endface coating, and electrodes placed on one channel for the modulation, as it can be seen in Fig. 7.19 a).

To achieve high-efficiency optical access to our photonic readout circuit, we use a dual-core fibre ferrule with a core separation of 127 µm, to match the waveguide separation at the endface. To attach the fibre ferrule to the lithium niobate sample, the fibre position is optimised by maximising the reflected power through the fibres and waveguides. Subsequently, the fibres are permanently fixed by a UV-adhesive (NOA81) at the fibre-to-sample interface. The sample and attached fibres are then placed on a mounting block for mechanical stability, whereby the lithium niobate is fixed to the surface with vacuum grease (Apiezon N) and the dual core single mode fibre is fixed with UV-cured adhesive to the holder.

We achieve a fibre-to-fibre efficiency of about 45% at 1530nm at room temperature, which reduces to 27% at cryogenic temperatures. The change in the coupling efficiency can be mainly attributed to mechanical changes in the adhesive bond during the cooling process. The supported optical mode in our waveguide have a large mode overlap with standard single mode fibres in the TM polarisation of 85% and with the TE polarisation of 92% [62]. We can expect an overall coupling efficiency between the waveguides and single mode fibre of 51% given a maximum mode overlap of 85%, a linear loss of 0.1 dB/cm, a coating reflectivity of 96% and a fibre to waveguide reflectivity of 97%. In summary, we achieve an overall device insertion loss of 3.5 dB at room temperature and 5.6 dB under cryogenic conditions.

The voltage signal generated by the photodiode and SNSPD is transmitted to the electrodes of the lithium niobate modulator. The voltage induces an electric field in the waveguide and changes the refractive index via the electro-optic effect. The electro-optic modulator is placed in an integrated Michelson interferometer such that the refractive index change will induce a relative phase change with the second beam splitter arm. Both beams interfere again after the reflection at the reflection coated endface. As a result, the reflected power of the Michelson interferometer is modulated dependent on the applied voltage which is used for the optical readout. The Michelson-interferometer layout is chosen to reduce the required voltage to introduce a phase shift because the phase shift is accumulated in both the forward and backward propagation through the modulator. The integrated Michelson interferometer is realised by titanium indiffused waveguides in z-cut lithium niobate. The endface reflector is realised by a dielectric reflective coating matched to the waveguides refractive index with a reflectivity of 96% [223]. More details on the fabrication and waveguide characterisation are given in the supplementary material. We characterised the electro-optic modulator by acquiring the intensity of the output by sweeping the voltage, as shown in Fig. 7.19 b). The modulation voltage required to switch the intensity from maximum to minimum is extracted to be 5.9 V at room temperature at an operation wavelength of 1530 nm. The V_π-voltage increases to 6.6 V at 1 K due to the temperature-dependent electro-optic coefficient which has been investigated previously [83, 219].

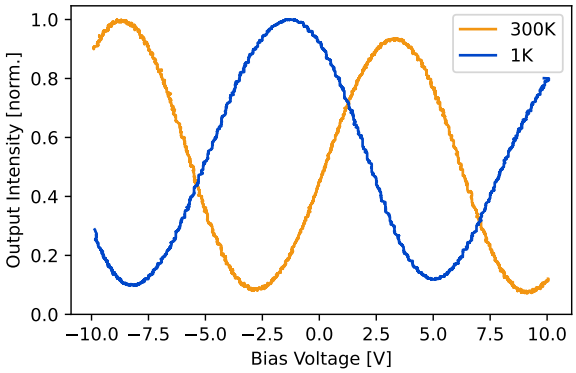

Figure 7.19: Voltage sweeps of the modulators at 1530 nm. The measured intensities are normalised to the maximal out power per sweep. The V_π voltage voltages are 5.9 Vat 1 Kand 6.6 Vat 300 K. The V_π voltage is acquired by fitting a sin-function to the acquired data.

Results

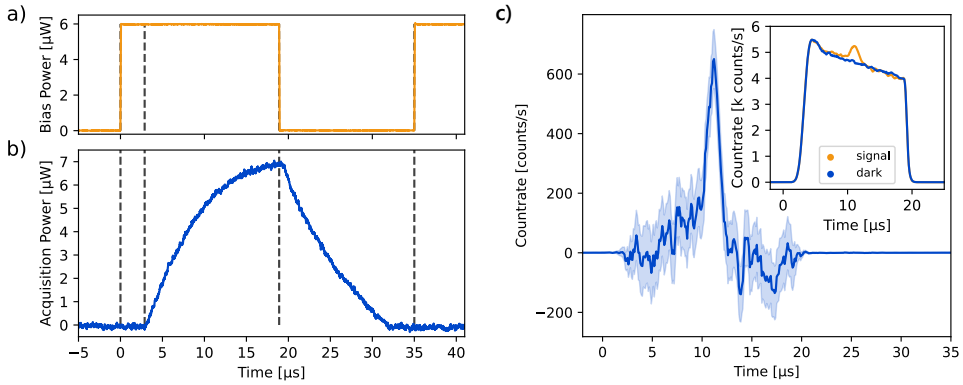

Figure 7.20: a) Optical modulation of the bias power for the cryogenic photodiode to operate the SNSPD. The modulation period is 35 µs. b) The optical response of the readout photodiode after the electro-optic modulator placed at room temperature. A photon impinges on the SNSPD at 2.9 µs, a voltage is generated and switches the electro-optic modulator. To reset the SNSPD, the optical power to the cryogenic photodiode is switched off after 18.9 µs. The nanowire becomes superconducting such that the generated voltage over nanowire resistance is reduced to zero. c) Histogram of the acquired countrate of the all-optical SNSPD operation. This is the difference in the countrate of the signal photons and measured dark counts. The error bars are determined by the counting errors of the count rates. The inset shows the total countrate of the measurement with and without a single photon input to the SNSPD. The mean photon number per pulse is 1.17±0.06.

We combine the operation of an opto-electronic bias of the SNSPD with an electro-optic readout. To do so, the photodiode, SNSPD, and lithium niobate modulator are connected

on a single cold stage of the cryostat and cooled down to a base temperature of 1 K. For the operation of the SNSPD a 6 µW cw-laser is externally on-off pulsed with a duty cycle of 35 µs, as illustrated in Fig. 7.20 a). A detection event occurs 2.9 µs after the illumination of the photodiode. As a result, a hotspot starts to grow, resulting in an increasing voltage delivered to the modulator. To read out the generated detection signal, light is transmitted through the modulator and the optical response is measured at room temperature. A typical measurement trace is shown in Fig. 7.20b). The resulting optical response signal has a 90% rise time of 11 µs. Once a photon is detected the superconductor becomes resistive and no subsequent photons can be detected, because the current through the nanowire is strongly reduced. The SNSPD is reset by switching off the light to the biasing photodiode after 18.9 µs, which results in an optical response with a fall time of 11 µs. To maximise the optical response, we tuned the operation wavelength of the modulator to 1530 nm and optimised the input polarisation with a fibre polarisation controller while a power of 3.5 mW is transmitted through the modulator. The optical response is read out with a photodiode at room temperature, resulting in a signal with an amplitude of 6.9 µW, given that the photodiode has a responsivity of 0.4 mV/µW and the readout amplitude is 2.76 mV, as shown in Fig. 7.20. In comparison, we expect an optical response of about 7.0 µW, given a click signal amplitude of 31 mV, a V_π of the modulator of 6.6 V and a fibre-to-fibre efficiency of the modulator of 27%. This shows the core principle that we can all-optically bias an SNSPD and read out the detection signal.

As a next step, we characterise the single photon response of the superconducting detector. To do so, we operated the SNSPD with our all-optical biasing method and acquired the countrate of the SNSPD with a single photon level input. To do so, we used a pulsed laser with a pulse width below 1 ps at 1545 nm. These pulses transmitted onto a calibrated reference detector and attenuated. The pulse are then attenuated and a mean photon number of 1.17±0.06 photons per pulse result. This optical input is then pulsed synchronously with the optical bias operated with a 35 µs on-off period. The timing delay of the generated click signals are then recorded in relation to the on-off signal.

Based on these results, we seek to reduce the optical throughput of the modulator to reduce both heatload and scatter. This depends on the minimal acquisition power of the detectors used to acquire the click signals. Small Formfactor Pluggable modules (SFP) are ideal candidates to measure small changes in intensity. The nominal minimal input pulse power of the SFP module is about −25 dBm at 1550 nm, which will generate an electrical output pulse of above 100 mV (Finisar FWLF-1519-7D-59). In our experiment we reduced the input power to the modulator to about 68 µW (∼−12 dBm) such that the click signal has an amplitude of about 125 nW(∼−39 dBm). When acquiring these signals with the SFP-module, the generated output signal of the module was reduced to about 20 mV. Additional high frequency noise in the output signal is also introduced at these low input powers, which we reduced with a 1 MHz low-pass filter. This added noise is negligible at higher input powers and higher signal count rates.

The click signals with a single photon input are then acquired with a time tagger and displayed as a histogram in Fig. 7.20 c). During the measurement, signal photons as well

as scattered light from the electro-optic modulator are detected. To extract the single photon events we performed a background measurement without a single photon input. By subtracting this background from the results with a single-photon input, a clear peak in the countrate at a delay of 11.3 µs with a full width half maximum of 1.5 µs can be seen, as shown in Fig. 7.20 c). The countrate in this histogram is negative after the main peak because the previous signal photons decrease the detection probability for subsequent background photons due to the SNSPD latching. The peak shows clearly that the SNSPD is sensitive to a single photon input in our all-optical operation method.

Discussion

The proof-of-principle devices presented here show promise for interfacing superconducting photonics in new performance regimes and application spaces, however there are still some non-idealities that can be improved in future work. A strong background of dark counts is present, mainly generated by scattered light introduced by the optical bias and readout of the SNSPD. Due to the lack of a self-reset, the detector clicks on the first photon that it measures, and none after that. Therefore, reducing the number of premature latching clicks from noise is necessary. In the present configuration, the components are mounted in the cryostat without intermediate shielding, the application of which would reduce the dark count rates significantly. Furthermore, one could exploit differences in the spectral sensitivity between the bias photodiode and the SNSPD to further reduce noise.

The SNSPD was operated with a repetition rate around 28 kHz, limited by the rise and fall time of the click signals. We attribute this to the charging dynamics of the capacitance of the electro-optic modulator and the growth of the resistive hotspot. Faster rise times can be achieved by introducing a parallel resistance to reduce the hotspot size. Introducing a parallel resistance also reduces the output voltage and hence the intensity modulation. Therefore, there exists a trade-off between the output voltage and the resulting rise time.

This bias and readout method has no effect on the internal detection efficiency of the SNSPD. We have previously shown that an optical bias and a conventional bias method achieve the same detection efficiencies [221]. Nevertheless, the lack of a self reset means that “true” counts may be lost if the detector has previously been triggered by a dark count, therefore reducing the noise also plays an important role in increasing the system efficiency. This could be further optimised by careful synchronisation of bias and readout light sources with respect to the expected arrival time of the single photons.

Independent of optical biasing and readout, exploiting the latched state of an SNSPD is an important method to step up the click signal. For example, amplitudes of 10 mV could be used to drive a Schmitt-trigger, which can enable feedforward modulation with electronic amplifiers. With this technique, the initial click signal is significantly increased, such that cryogenic low noise amplifiers can be avoided. The key to this method is to integrate a current source which can reset the latched SNSPD after the detection.

By connecting the output of the detector to a modulator, this method is an important step towards all-optical feedforward modulation [93] at cryogenic temperatures, which is integral to quantum photonic one-way computing [29]. This can be achieved by a direct matching of the generated output voltage of the SNSPD signal and the switching voltage of the modulator. In this technique, a photon can be detected by the single photon detector switching the electro-optic modulator from one state to the other. Future work is needed to match the detector output and modulation voltages at cryogenic temperatures. In addition, the rise time of the click signal must be improved to minimise optical delays when using feedforward modulation with low latency processes.

Since optical fibres inherently have a lower thermal conductivity than coaxial cables, this can significantly reduce the heatload on the cryostat [51, 131]. The passive heatload of coaxial cables can be mitigated by thermal anchoring in the cryostat but are a major contributor to the thermal load on a cryostat [123]. In our operation of the SNSPD, three independent optical fibres are directly connected from room temperature to the photodiode and electro-optical modulator without the need of intermediate thermal anchoring. The active heatload of these electro-optic devices are 6 µW for the photodiode and 68 µW for the electro-optic modulator. The active heatload of the modulator can be reduced further to a few µW by reducing the modulation voltage V_π and increasing the detection signal voltage, such that the full throughput intensity is modulated. In addition, wavelength-division multiplexing can also be used for the bias and readout to operate multiple SNSPDs in parallel to reduce the passive heatload even further [131].

Conclusion

In summary, we have realised an all-optical interface for quantum photonic applications. The interface provides the operation power for a superconducting single photon detector via a cryogenic photodiode. In addition, the detection signals are readout optically via an electro-optic modulator at cryogenic temperatures. The all-optical operation shows promising techniques for the combined operation of superconducting electronics and photonics circuits, which are electrically isolated from their driving circuitry. Increasing the signal amplitudes and modulation capabilities of the opto-electronic components enables further applications such as feed-forward. Furthermore, the all-optical operation of the SNSPD achieves a low power operation of the SNSPD by providing only a total operation power of 75 µW.

Funding

This work was supported by the Bundesministerium für Bildung und Forschung (Grant No. 13N14911) and co-funded by the European Union (ERC, QuESADILLA, 101042399). Views and opinions expressed are however those of the author(s) only and do not necessarily reflect those of the European Union or the European Research Council. Neither the European Union nor the granting authority can be held responsible for them.

Acknowledgments

We thank Varun Verma (NIST) for providing the superconducting films for the Superconducting Nanowire Single Photon Detectors.

Disclosures

The authors declare no conflicts of interest.

7.5 All optical operation of a superconducting photonic interface: supplementary material

In this setup, the cryogenic readout of the detection signals is realised through an electro-optic modulation. We choose titanium indiffused lithium niobate as a material platform to realise an integrated intensity modulator. In this platform we can use the electro-optic effect even at cryogenic temperatures as well as achieve a high coupling efficiency between a single mode fibre and the waveguide. The electro-optic modulation is realised in a Michelson-interferometer in which a beamsplitter, phase modulator and endface reflector are integrated with waveguides, as illustrated in Fig. 3 a). Light is coupled into the chip and split into two paths by the 50:50 beamsplitter. On one arm of the beamsplitter light is modulated by the electro-optic phase shifter. Both beams are then reflected at the endface of the chips with an endface coating. The reflected light is propagating in the reverse direction and interfere on the beamsplitter again. As a result, an intensity modulation can be read out when the voltage on the electro-optic modulator is varied because the relative phase between the beams is changed. The Michelson-interferometer layout is chosen to reduce the required voltage to introduce the phase shift because the phase shift is accumulated in both the forward and backward propagation through the modulator.

The waveguides are realised in this lithium niobate platform by a titanium in-diffusion process. To do so, titanium is deposited on top of the sample and patterned with laser photo-lithography and wet-etching. A resulting 7 µm wide titanium stripe is then diffused into the sample in an oven. The in-diffused titanium increases the reflective index such that wave guiding is achieved. The optical loss in the waveguides are characterised with the Fabry-Pérot method with a straight waveguides next to the Michelson-interferometer before the reflective coating is applied [148]. The resulting losses are about 0.1dB/cm at a wavelength of 1550 nm in the TE polarisation.

The integrated 50:50 beamsplitter is realised by an evanescent coupler consisting of two parallel waveguides, as illustrated in Fig. 3 a). The waveguides separation distance is reduced from 127 µm to 13 µm by S-bends to interfere on 8.3 mm long distance and then separated again. This coupling length is chosen such that a splitting ratio of 50:50 is reached

between the optical path in both polarisations TE and TM. The total length of the sample is 56 mm, including the beam splitter and modulator.

A phase shift in the Michelson-interferometer is realised by an electro-optic modulator. An electric field in the waveguide is introduced when a voltage is applied to electrodes on the surface of the sample. This electric field introduces a refractive index change in the waveguide, which induces a relative phase shift between the beamsplitter arms, as it can be seen in Fig. 3 a). The modulator's electrodes are placed behind the beam splitter with respect to the input facet. The electrode pair is positioned parallel to the waveguide such that the inner edge of one electrode overlaps the waveguide to induce a vertical electric field. The second electrode is placed next to the waveguide and is separated distance of 9 µm from the first electrode. The electrode pair has a length of 20 mm and overlaps the waveguide over the full length. The electrode stack consisting of a 400 nm SiO_2 bottom layer, 10 nm titanium adhesion-layer and 100 nm gold layer which is selectively deposited with photo-lithography and lift-off process.

The reflector in the Michelson setup is realised by an endface coating on the endfacet at opposite side to the fibre input. To do so, the endface is polished using a CMP method. Afterwards a dielectric coating is deposited by evaporating titanium oxide and silicon oxide using an oxigen ion assisted electron beam evaporation method [223]. The dielectric-stack is designed such that a high reflectivity is reached in a range from 1500 nm to 1600 nm. The reflectivity is characterised by measuring the transmission through a reference lithium niobate sample with the same dielectric stack. A reflectivity of 96% is achieved at the operation wavelength of our experiment, namely 1530 nm.

The integrated Michelson-interferometer achieves the strongest intensity modulation when a splitting ratio of 50:50 is reached for the beamsplitter. To characterise the intensity modulation we coupled light into the waveguide and swept the bias voltage at the electrodes. A relative phase difference of π between the modulated and unmodulated path is needed to switch the intensity from a minimum to a maximum. The bias voltage dependent intensity follows a sin-function such that we can fit this function to extract the V_π-voltage, compare Fig. Fig. 3 b). This modulation voltage is characterised to be 5.9 V at room temperature and increases to 6.6 V when cooled down to an operation temperature of 1 K. The increase in the V_π-voltage is due to the temperature-dependent electro-optic coefficient which has been investigated previously [83, 219]. In summary, our electro-optic modulator reaches a modulation strength of 23.6 Vcm at an operation wavelength of 1530 nm.

7.6 Pyroelectric Influence on Lithium Niobate During the Thermal Transition for Cryogenic Integrated Photonics

Frederik Thiele[1], Thomas Hummel[1], Nina Amelie Lange[1], Felix Dreher[1], Maximilian Protte[1], Felix vom Bruch[1], Sebastian Lengeling[1], Harald Herrmann[1], Christof Eigner[1], Christine Silberhorn[1], and Tim J. Bartley[1] [1] Department of Physics & Institute for Photonic Quantum Systems, Paderborn University, Warburger Str. 100, Paderborn, Germany

[1]Institute for Photonic Quantum Systems, Paderborn University, Warburger Str. 100, Paderborn, Germany

Publication:
"Pyroelectric Influence on Lithium Niobate During the Thermal Transition for Cryogenic Integrated Photonics," arxiv:2306.12123, Jun. 2023.
`http://arxiv.org/abs/2306.12123`

Abstract

Lithium niobate has emerged as a promising platform for integrated quantum optics, enabling efficient generation, manipulation, and detection of quantum states of light. However, integrating single-photon detectors requires cryogenic operating temperatures, since the best performing detectors are based on narrow superconducting wires. While previous studies have demonstrated the operation of quantum light sources and electro-optic modulators in $LiNbO_3$ at cryogenic temperatures, the thermal transition between room temperature and cryogenic conditions introduces additional effects that can significantly influence device performance. In this paper, we investigate the generation of pyroelectric charges and their impact on the optical properties of lithium niobate waveguides when changing from room temperature to 25 K, and vice versa. We measure the generated pyroelectric charge flow and correlate this with fast changes in the birefringence acquired through the Sénarmont-method. Both electrical and optical influence of the pyroelectric effect occur predominantly at temperatures above 100 K.

Introduction

The aim of integrated quantum photonics is to combine multiple optical devices on a single chip to profit from their interplay in a stable and scalable experimental setup [10, 224]. Components for quantum light generation, manipulation, and detection can be combined to realize a multitude of complex integrated circuits for various applications [32, 194]. A careful selection of the integrated components and material platform is required since the devices must be compatible in their optical characteristics and operation conditions [9]. While most devices are optimized for room temperature operation, superconducting single-photon detectors and solid-state quantum emitters require cryogenic temperatures [193]. When combining cryogenic integrated components, these devices dictate the operation

temperature for integrated chips. To that end, it is indispensable to develop all-integrated components for the cryogenic temperature application.

Lithium niobate is a well established nonlinear platform for integrated quantum photonics. In recent years, this platform has shown great cryogenic compatibility by the realization of integrated components for generation, manipulation, and detection of quantum states of light [26, 36, 121, 146, 218, 219]. Cryogenic single-photon sources in lithium niobate are realized through the integration of quantum dots [70], and via spontaneous parametric down-conversion in quasi-phase-matched waveguides [26, 60]. The first cryogenic electro-optic modulators were demonstrated in the 90s [28, 36, 43, 146, 179]. Nowadays three main modulator schemes exist for cryogenic operation, such as phase-shifter, directional coupler, and polarization converter [218, 219]. Integrated superconducting single-photon detectors are successfully shown for weakly confined waveguide structures [34, 61], and as well on thin film lithium niobate [121, 199]. Electro-optic modulators can be used to read out superconducting devices [59, 225], and are integrated together with superconducting detectors [121]. In addition, nonlinear frequency conversion processes have been established at cryogenic temperatures, such as second harmonic generation in periodically poled waveguides [25], and cryogenic transducers for terahertz generation by optical rectification [226–228]

The listed integrated devices in lithium niobate have demonstrated their functionality when operated at a stable cryogenic temperature. However, in previous work unpredictable changes in the electrical and optical properties were observed during the thermal transition between room temperature and cryogenic temperatures [25, 64, 218]. These changes range from sudden jumps to slower shifts in the optical properties on different time scales. The cryogenic operation of nonlinear interactions and electro-optic modulation induces a shift of the operation characteristics such as the phasematched wavelength, when compared to room temperature applications [25, 26, 218]. The variation can be attributed to thermal stress and pyroelectric charges which build up inside the ferroelectric lithium niobate crystal when the temperature changes [229, 230]. The unbound charge carriers induce localized electric fields, causing microscopic refractive index perturbations, due to the electro-optic effect [18]. In addition, the unbound carriers can flow through the sample and accumulate at the surface. Electrodes placed on top of the sample can collect the charges such that a macroscopic current can be measured with a sensitive current meter. When operating the chip under ambient conditions, charges at the surface can be neutralized by charges in the air. However, when operating lithium niobate in an evacuated cryostat chamber, they cannot be so easily neutralized. As a consequence, pyroelectric charges can disturb the device performance during a temperature transition [25, 218], or even damage integrated structures, such as superconducting detectors [35].

In this paper, we investigate the origin of perturbations, which appear in the thermal transition. Characterizing and understanding the temperature dependent changes are necessary to optimize photonic circuits and to chose the optimal parameters such as the bias voltage for electro-optical modulators for cryogenic operation. Moreover, refractive index perturbations can influence the operation wavelength for phase-matched processes

such as nonlinear frequency conversion [25]. Low temperature investigations of the pyroelectric behavior of lithium niobate were performed at a stable temperature, as well as during a thermal transition [25, 64, 65, 83, 218, 231]. We report to the best of our knowledge the first simultaneous measurement of electric discharges inside an electro-optic modulator and variations in the optical throughput, when changing the operation temperature. We observe the discharges by measuring the current between electrodes on the surface of the modulator, and use the Sénarmont-method to visualize localised changes in the refractive index, manifesting as phase shifts in the transmitted light [206]. The device under test is cooled down from room temperature to cryogenic temperatures and warmed up again to obtain data for a whole cool-down and warm-up, covering a temperature range from 25 K to 285 K.

Pyroelectric refractive index variations

Lithium niobate is used for integrated photonic circuits due to its large nonlinear properties, wide transparency range, and electro-optic properties [8, 18]. In this material the refractive index can be varied by applying a constant electric field E_j^{DC}, inducing a refractive index in a correlated i-direction [18]. Since this material is birefringent, the amplitude of the refractive index change Δn_i depends on the direction of the DC-electric field following [18, 37, 232],

$$\Delta n_i \sim r_{ij} E_j^{DC}, \tag{7.20}$$

where r_{ij} is the electro-optic tensor for lithium niobate. An electric field applied in the vertical orientation modulates the refractive index according to the electro-optic field tensor r_{33}, and an applied horizontal field by r_{13} [18, 233].

We realize an electro-optic modulator in z-cut lithium niobate by fabricating titanium in-diffused waveguides with electrodes placed around the waveguide, see Fig. 7.21. These electrodes allow us to apply the external electric field E_j^{DC} to change the refractive index. In this paper we use a phase modulator where one of the electrodes is placed on top of the waveguide to induce a vertical electric field, as depicted in Fig. 7.21.

In a thermal transition, lithium niobate generates unbound carriers in the material domain [37, 206], resulting in electric fields in the material due to these pyroelectric charges. The induced fields changes the refractive index independent of the applied voltage at the electrodes of the modulator. In z-cut lithium niobate, the unbound charge carriers can flow along the grain boundaries towards the top surface and recombine at the top surface [234]. The redistribution and discharge of the carriers will follow a capacitive discharge with an associated resistance R and capacity C [235]

$$I(t) = I_0 e^{-t/\tau_{RC}}, \tag{7.21}$$

where $\tau_{RC} = RC$ is the time constant related to the discharge. The charges accumulate in a confined space and therefore the resulting effect is a microscopic effect. In addition, we expect the pyroelectric charges to be generated at various locations in the lithium niobate.

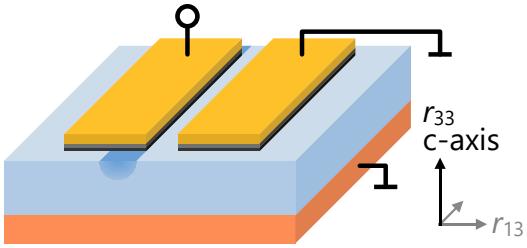

Figure 7.21: Schematic of the device under test to investigate electrical and optical changes in the thermal transition in a cryostat. The sample consists of a Ti-in-diffused z-cut lithium niobate waveguide with electrodes in a phase modulator configuration. The modulator is mounted on a copper plate, connecting the backplane of the sample to the case-ground of the cryostat. The electrodes are connected to a break out board via aluminium wirebonds and coaxial cables which transmit the signal to a room temperature current meter.

The charge relaxation time, or discharge time constant τ_{RC} can thus be derived dependant on the microscopic geometry of lithium niobate, and not on the macroscopic design of the electrodes. Electrodes along the waveguide can collect the charge carriers. The electrodes are than connected to a current meter which average the charge flow. In a macroscopic perspective this is known as the pyroelectric effect which is described as a current between two domain surfaces while the temperature changes [37, 206].

Methods

We investigate the correlation between changes in the refractive index and generated pyroelectric discharges in lithium niobate while changing the operation temperature from room temperature to cryogenic temperatures and back to room temperature. To measure changes in the refractive index, we use the birefringence. Light is coupled into orthogonal polarization modes (TE and TM) of the waveguide and subsequently interfered, such that a change in the relative phase between two modes can be extracted. Simultaneously, the generated pyroelectric charges are measured as a current flowing through the electrodes on the surface of the sample. The simultaneous measurement of changes in the refractive index and generated charges may be correlated, since induced electric fields should result in refractive index changes.

Sénarmont-method with electro-optic waveguides

The Sénarmont-method measures the birefringence between TE and TM polarization modes of light in a waveguide [206]. Both transmitted modes will accumulate a change in their optical path length and thus phase, due to the temperature dependent change in the refractive index [85, 233]. The relative phase between these modes is extracted by measuring the power ratio between the two polarization outputs after they are interfered. Since this is a relative measure, it is independent of coupling losses. Varying the temperature results in a change of optical coupling into the waveguide due to thermal contraction and expansion

of the mounting stages. However, crucially the Sénarmont-method is independent of the coupling efficiency.

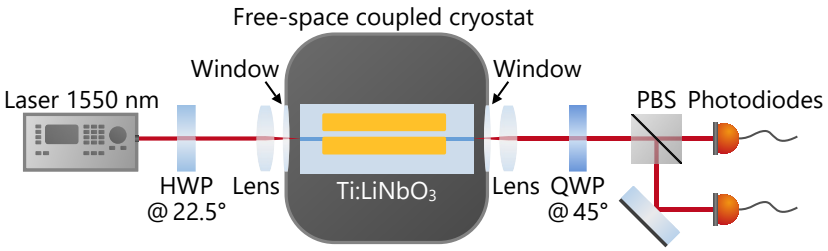

Figure 7.22: Schematic of the setup to measure the optical changes in the lithium niobate sample during the thermal transitions. The sample is mounted in a free-space accessible cryostat whereby light is coupled through the windows. Changes in birefringence in the waveguide are measured using the Sénarmont-method. The optical input comes from a 1550 nm wavelength laser with 2.2 mW of optical power. To measure the generated pyroelectric charges, the gold electrodes on the surface of the sample are wire bonded and connected to a current meter at room temperature.

We mount our lithium niobate waveguides in a free-space accessible cryostat and couple light into the waveguides, as it can be seen in Fig. 7.22. The input light is polarized at 45 ° such that light is coupled equally into the two polarizations. After the transmission through the waveguide with the length L, a relative phase

$$\Phi_{\mathrm{H,V}} = 2\pi n_{\mathrm{H,V}} L/\lambda \tag{7.22}$$

is accumulated for the horizontal and vertical polarization, where $n_{\mathrm{H,V}}$ is the refractive index for either polarization, and λ is the wavelength.

To acquire the relative phase difference $\Delta\Phi = \Phi_{\mathrm{H}} - \Phi_{\mathrm{V}}$, the two polarizations are interfered with a quarter-wave plate aligned at 45 ° and a polarizing beam splitter (PBS). The intensities after both output channels of the PBS $I_{1,2}$ are acquired and depend on $\Delta\Phi$ via

$$I_{1,2} = I_0 \cdot \frac{1}{2}\left(1 \pm \sin(\Delta\Phi)\right) \ . \tag{7.23}$$

In the experiment, the relative phase can be directly extracted from the intensity of one output of the PBS if the total in-coupled power I_0 is known. However, thermal contraction and expansion of the mounting stages change the coupling efficiency resulting in a time-dependant I_0. To extract changes in the refractive index, the intensity of one output arm of the PBS is normalized by the sum of both outputs

$$\tilde{I}_{1,2} = \frac{I_{1,2}}{I_0} = \frac{I_{1,2}}{I_1 + I_2}\,, \tag{7.24}$$

which allows us to extract $\Delta\Phi$ independent of the coupling efficiency.

We change the sample temperature in the cryostat from 280 K to 25 K and back to 280 K with a constant rate of 1 K/min. The relative phase changes due to the temperature dependence of the refractive index. As a result, we expect to see an oscillation in the normalized output intensity with an oscillation time of 3 –10 min/oscillation. In addition, recombination of the pyroelectric charges can generate sudden changes in the refractive index due to the aforementioned electro-optic effect causing an abrupt change in the phase $\Delta\Phi$.

To measure the change in the generated pyroelectric charges we connect a current meter between the electrodes placed around the waveguide of the lithium niobate sample. The current meter has a sensitivity of 0.05 pA when acquiring currents in a range up to ± 2 nA. To correlate changes in the optical throughput and generated current, we measure both simultaneously with a sample rate of 1.7 samples/s.

Our input light comes from a CW-laser at a wavelength of 1550 nm with (2.2 ± 0.1) mW of optical power. Lenses outside the cryostat couple the light into the waveguide. At room temperature, the transmitted power through the waveguide is (1.2 ± 0.1) mW. The coupling efficiency changes during the thermal transition due to thermal contraction and expansion, dominated by height variations of the mounting stack. For that reason, we reoptimize the vertical alignment of the sample during the thermal transition to ensure the transmitted power does not drop below 6 µW. These brief optimizations allow the transmitted power to exceed at least 300 µW after every reoptimization, while the measurement is interrupted for approximately only one minute for eight optimizations during the cooling process.

Sample fabrication

The device under test is a z-cut lithium niobate sample with a titanium in-diffused waveguide and electrodes in a phase-modulator configuration [219]. To fabricate the waveguide, titanium is selectively deposited on the surface with a photo-lithography and lift-off process, resulting in 5 µm wide titanium stripes. These stripes are in-diffused in the sample via heating in an oven, resulting in a localized change of the refractive index, allowing the guiding of light. The linear losses of the waveguide are determined to be about 0.15 dB/cm [219], with a Fabry-Pérot method [148]. A second photo-lithography and lift-off process are used to fabricate electrodes on the sample. The electrodes consist of a stack of 400 nm silicon dioxide as a buffer layer, 10 nm chromium for adhesion, and 300 nm gold as our electrode. The electrodes are placed in a phase modulator configuration to induce a primarily vertical electric field component in the waveguide. To do so, one electrode is placed on the top of the waveguide such that one inner electrode edge is aligned to the outer waveguide edge. The second electrode is placed at a distance of 9 µm from the first electrode, as can be seen in Fig. 7.21. The waveguides length is 22 mm with 12 mm long electrodes on the top surface. The total thickness of the lithium niobate sample is 500 µm. Initial characterisations of the phase modulator with the Sénarmont-method show a modulation voltage of 23.3 V at room temperature and 40 V at cryogenic temperatures. The modulation voltage is the required voltage to switch from a maximum to a minimum in the intensity output.

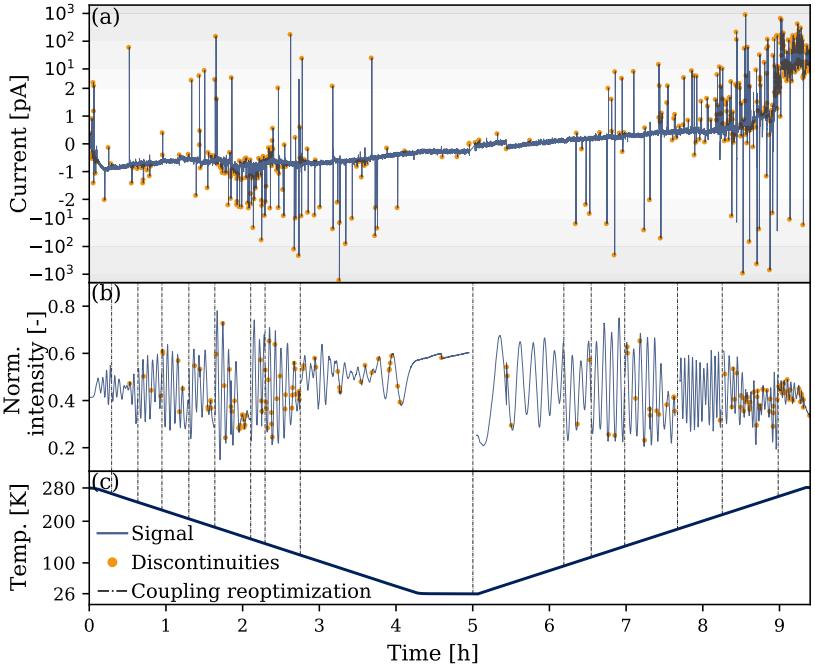

Figure 7.23: Measurement data of (a) the measured current between the electrodes of the phase modulator, (b) the normalized intensity $\tilde{I}_1$ in a single PBS port, and (c) the temperature of the sample stage on which the sample is mounted. The acquired signals are represented in the blue lines, and every extracted discontinuity in the electrical or optical signal is marked with an orange dot. The vertical lines indicate the time periods where the optical power through the sample is reoptimized with the vertical alignment.

Results

The lithium niobate sample is cooled down and warmed up in the cryostat while the generated current and optical transmission are acquired. These two signals and the temperature are shown in Fig. 7.23. In addition, the time intervals where the optical coupling is reoptimized are marked with a vertical dashed line. In Fig. 7.23 (a) shows the corresponding electrical current measured through the electrodes. The normalized optical power of channel 1 is shown in Fig. 7.23 (b), and the expected $3 - 10\,\mathrm{min/oscillation}$ due to the thermal change of the refractive index can be seen.

Discontinuities in the optical and electrical signal can be extracted using a signal processing algorithm to minimize the human bias. Our extraction method uses the SciPy package in our algorithm written in Python [236]. Since a discontinuity in the optical signal is a rapid change of the phase, we can extract this with a derivative. We use an averaged derivative implemented as a convolution of the dataset with the matrix $\frac{1}{6}\,[1, 1, 1, -1, -1, -1]$. The slow oscillation is then still present, but this is filtered out with a 4^{th} order high-pass Butterworth filter with a cut-off frequency $f_c = 36\,\mathrm{mHz}$. The discontinuities are then extracted with the SciPy peakfinding algorithm with a prominence of > 0.006, which indicates the minimum height of the peak compared to the base of the signal. Fine-tuning of the analysis parameters was challenging because the height of the peaks varies in many orders of magnitude. It was impossible to discriminate between optical changes and noise in the optical signal at constant cryogenic temperatures. For this reason, the optical discontinuities at constant cryogenic temperatures are selected by hand. The electrical signal only requires a high-pass filter to remove the DC-drift current. After that, the discontinuities are extracted by the peakfinder algorithm. We used a 4^{th} order Butterworth filter with a cut-off frequency $f_c = 0.27\,\mathrm{mHz}$, and a minimum prominence of 0.2 in the peak-finder. All extracted discontinuities are shown as orange dots in Fig. 7.23 (a) and (b).

The displayed data range in Fig. 7.23 (a) highlights the lower current region to show the drift in the current. Only discontinuities up to 2 pA are thus shown, however, these discontinuities can go as high as 2 nA in the measurement. The background current can be attributed to an averaged pyroelectric charge generation over the sample. Since the pyroelectric charge generation is proportional to the time derivative of the temperature, the current should change direction between the cooling process and heating process. The temperature of the sample is shown in Fig. 7.23 (c), showing that the temperature is changed from 280 K to 25 K and back with a constant rate of temperature change. After the sample reaches 25 K, it remains at this temperature for 43 min.

We analyze the correlation between the electrical and optical discontinuities, which results in three different types of possibilities:

- Purely optical discontinuity;
- Purely electrical discontinuity;
- Correlated discontinuities.

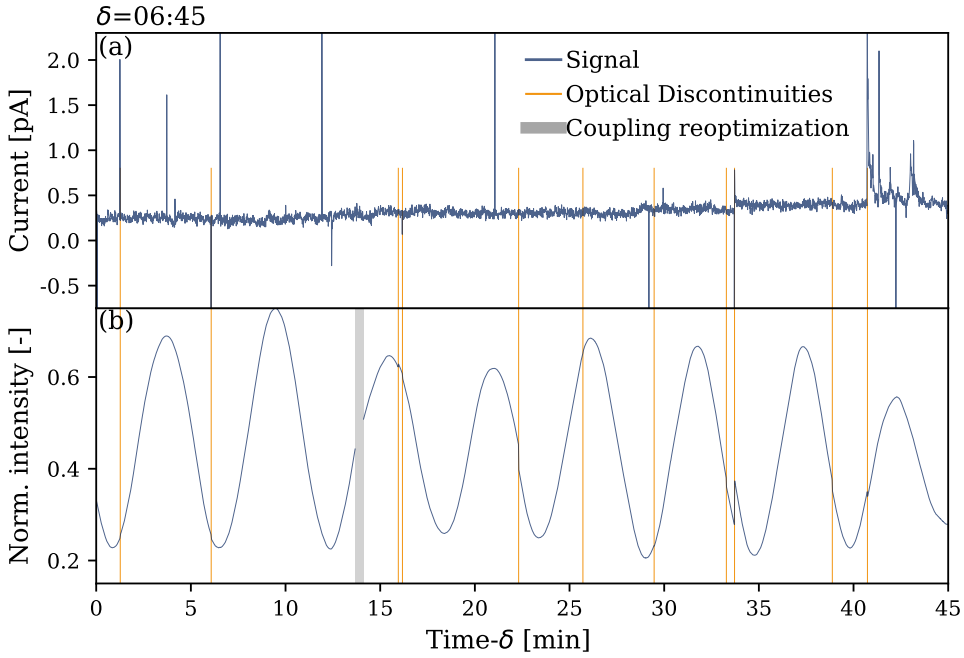

Figure 7.24: Cutout of the data set in Fig. 7.23 starting at 127 K during the warming process. (a) The electrical current measured by the current meter. The spikes are electrical discontinuities and indicate the recombination of charges. (b) Normalized optical intensity $\tilde{I}_1$. The gray shaded area marks the time interval where the optical power was reoptimized, and the orange vertical lines mark all optical discontinuities extracted by the algorithm.

All three possibilities can be found in Fig. 7.24, showing a cutout of the dataset starting at $\delta = 06{:}45$h and has a length of 45 min, spanning the temperature range from 127 K to 172 K. The grey shaded area (at 15 minutes) marks a time interval where the optical power is reoptimized, and the vertical orange lines mark the times where an optical discontinuity is extracted. Electrical discontinuities are visible from the signal itself as spikes in the electrical signal, and multiple datapoints exceed the vertical limit of the figure. This figure shows clearly that there are individual discontinuities in the electrical signal (e.g. 12 min) and optical signal (e.g. 22 min), as well as correlated discontinuities (e.g. 33 min). The electrical discontinuities after 40 minutes show an exponential decay, indicating relaxation of electrical charges.

Figure 7.23 indicates that there are temperature intervals with higher and lower densities of discontinuities. For this we investigate the occurrence of discontinuities over the different temperature intervals, with a binning width of 30 K and bin centres from 30 K to 270 K. This range is chosen since these binwidths cover the full temperature range with a significant number of steps. In addition, a significant number of occurrences are maintained in most bins. Figure 7.25 shows the occurrences of optical and electrical discontinuities, as well as the correlated discontinuities. Due to the data acquisition and signal analysis, electrical

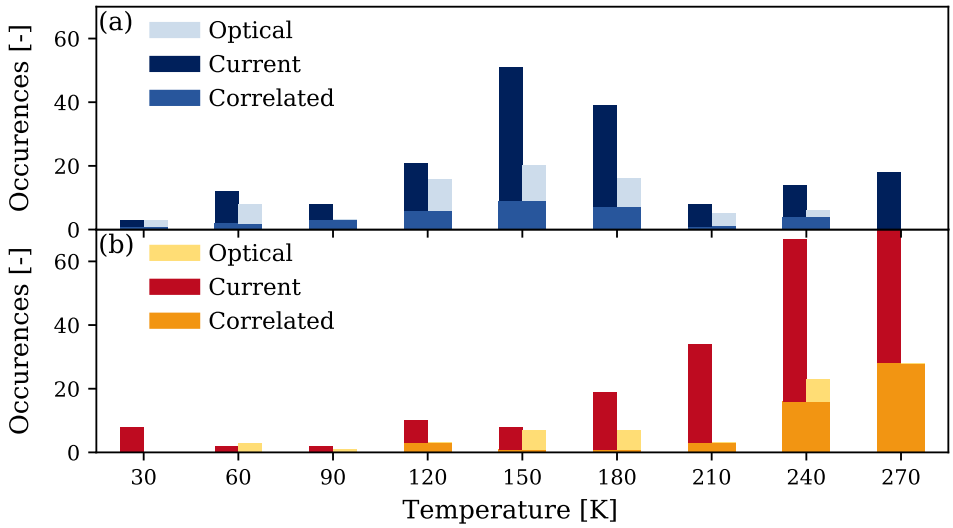

Figure 7.25: Histogram of the number of discontinuities (occurrences) for the electrical and optical signal, as well as for correlated discontinuities. The binning is chosen with bin centres from 30 K to 270 K with binwidths of 30 K, spanning the full temperature range of our measurement. (a) shows the number of occurrences during the cooling process, and (b) during the warming process. They show different temperature ranges where the number of discontinuities reaches a local maximum. In (b) we truncated the number of electrical discharges at 270 K reaching 200 occurrences, for an improved visibility. However, both show that the number of discontinuities almost disappears below 115 K.

and optical discontinuities within 6 s of each other are considered correlated. Histograms are made for both the cooling process (Fig. 7.25 (a)) and the warming process (Fig. 7.25 (b)). During the sample cooling, a clear increase in the number of discontinuities between 195 K and 115 K is present. In this range, the electrical occurrences dominate over the occurrences of optical discontinuities. Below 115 K discontinuities are less frequent, indicating a reduced pyroelectric effect resulting in higher stability compared to the temperatures above 115 K. Warming up the sample shows an increase of the number of discontinuities with the temperature starting from 115 K. These two histograms imply that the temperature at which most discontinuities occur, depends on whether the sample is warmed up or cooled down. However, in both cases they almost disappear below 115 K. The reduction of the pyroelectric charge recombination can be explained by the reduced pyroelectric coefficient [237], and reduced charge mobility [233, 238], at cryogenic temperatures.

We assume that almost no unbound charge carriers are present in the sample when we start the experiment at room temperature. During the cooling process, pyroelectric charges are generated and accumulate within the material domain until the charge density reaches a threshold and the charges recombine. Lower temperatures should result in a lower probability generating pyroelectric charges due to the reduced pyroelectric coefficient. In addition, the charge mobility is reduced, increasing the threshold for the required

discharge to warrant a recombination. These two effects cause a reduction of charge recombinations at cryogenic temperatures, which can be seen from the reduced number of electrical discontinuities below 115 K. This results in a reduced number of discharges while the sample is at a stable cryogenic temperature. When the sample is warmed up again, the charge mobility increases, and more pyroelectric charges are generated again which results in electrical discharges [233, 237]. As a result, the probability of charge relaxation will increase with temperature, resulting in an ever increasing number of electrical discontinuities at our highest measured temperature.

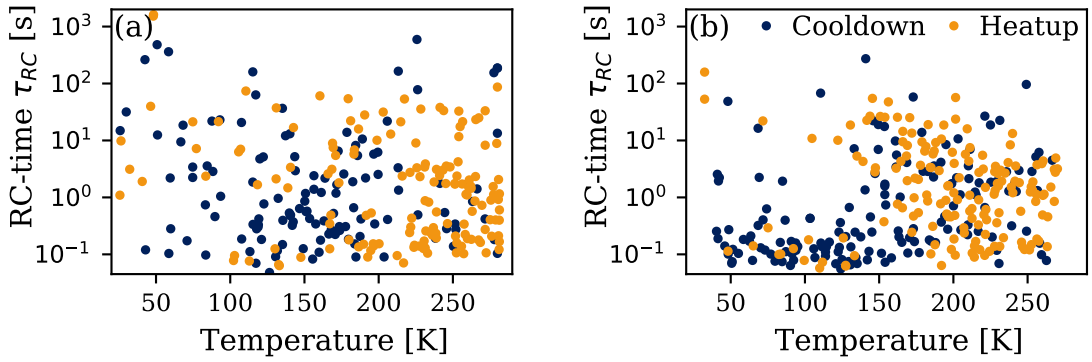

Figure 7.26: Decay times of the identified current fluctuations for the measurement (a) with light, and (b) without light coupled through the waveguide. Current fluctuations with only a single data point are excluded since no decay rate can be fitted to these.

Our method allows us to extract current fluctuations in the sample. Furthermore, we analyse these discontinuities upon their decaying dynamics in the charge recombination. The recombination of the charges depends on the effective resistance and capacitance from the point of origin to the recombination. As a result, we can connect an RC-time (τ_{RC}) to every discharge by fitting an exponential decay [235]. Fluctuations with only a single point decay are excluded since they are too fast to be discriminated with our set sampling rate. The RC-time of all other decays is shown in Fig. 7.26 (a), where it is plotted versus the temperature, and separated by cool down (blue dots) and heat up (orange dots). The extracted decays show that the decay rates are independent on the temperature and vary over multiple orders of magnitude. Additionally, the decay rates are independent of direction in the temperature change, however, the decay density depends on the temperature as was shown in Fig. 7.25. This is expected since carriers are generated at various points in the material domain and redistribute in different directions, resulting in different RC-times.

Unbound charges can also be generated by the transmitted light, the so called photorefractive effect [232]. These unbound carriers could be another source to induce electric fields in the vicinity of the lithium niobate waveguide. To investigate this influence, we additionally cooled down and heated up the sample without light going through the waveguide and with the same temperature rates (1 K/min), while we measured the current through the electrodes. In the thermal transition, fluctuations in the current are visible similar to the

measurements with light through the waveguide. The number of occurrences and the related RC-times are similar to the optical measurement, as it can be seen in Fig. 7.26 (b). This data hints that the measurement without light shows more fast decays at cryogenic temperature, thus less discontinuities when light is coupled through the waveguide. However, due to the sparsity of the data, no hard conclusion can be drawn.

Conclusion

Lithium niobate has proven to be a valuable material system for integrated quantum optics, expanding into cryogenic temperature regimes [25, 26, 35, 61, 121, 218, 219]. In this photonic platform, cryogenic frequency conversion sources [25, 26] and electro-optic modulators [218, 219] were implemented, revealing optical changes in the operation characteristics. Furthermore, the integration of superconducting single photon detectors poses challenges due to the destructive nature of pyroelectric charges during the cooling process [35].

To address this issue and create a more reliable platform for integrated quantum photonics, we investigated the optical changes and pyroelectric discharges in lithium niobate. We utilize the Sénarmont-method to measure changes in waveguide birefringence and correlate these changes with acquired pyroelectric discharges. The occurrence of electronic and optical perturbations show a correlation during the entire temperature range.

During the cooling process, the occurrences of pyroelectric discharges and optical changes increase until a temperature of approximately 150 K is reached, afterwards they reduce significantly and almost vanishes below 100 K. At stable cryogenic temperatures, minimal optical or current perturbations are observed. During the heating process, the rate of occurrences is constant until 100 K and increases for higher temperatures.

To further investigate the phenomenon, we conducted control measurements without any input light. The comparison between the control and Sénarmont measurements shows no significant variations in the generated pyroelectric charges, excluding the significant influence of photo-refraction. This confirms that pyroelectric charge generation during a temperature transition is the predominant effect.

The decay rates of the electrical discharges were found to span several orders of magnitude, regardless of the temperature. This suggests that there is no specific capacitive geometry within the sample where all the discharges occur. Future investigations can explore the impact of different types and designs of electro-optic modulators, as well as the effect of the temperature rate during thermal transitions. By understanding these effects, introduction of partial conductive layers on the lithium niobate structures to minimize the influence of pyroelectric charges can be investigated.

By studying these optical changes and pyroelectric discharges in lithium niobate, we aim to enable the integration of superconducting single photon detectors with modulators and

frequency conversion sources. This integration is crucial for achieving a scalable photonic platform in the field of integrated quantum photonics.

Data Availability

The data is openly available under the following link:

`https://physik.uni-paderborn.de/bartley/permalinks/thielehummel2023`

Acknowledgements

This work was supported by the Bundesministerium für Bildung und Forschung (Grant No. 13N14911) and the Deutsche Forschungsgemeinschaft (231447078–TRR 142).

Bibliography

8

[1] LIGOcollaboration, Enhanced sensitivity of the LIGO gravitational wave detector by using squeezed states of light, Nature Photonics **7**, 613–619 (2013).

[2] H.-K. Lo, M. Curty, and K. Tamaki, Secure quantum key distribution, Nature Photonics **8**, 595–604 (2014).

[3] L. S. Madsen et al., Quantum computational advantage with a programmable photonic processor, Nature **606**, 75–81 (2022).

[4] H. S. Zhong et al., Quantum computational advantage using photons, Science **370**, 1460–1463 (2020).

[5] U. Chabaud and M. Walschaers, Resources for Bosonic Quantum Computational Advantage, Physical Review Letters **130**, 90602 (2023).

[6] M. Saffman, Quantum computing with atomic qubits and Rydberg interactions: progress and challenges, Journal of Physics B: Atomic, Molecular and Optical Physics **49**, 202001 (2016).

[7] S. Bravyi, O. Dial, J. M. Gambetta, D. Gil, and Z. Nazario, The future of quantum computing with superconducting qubits, Journal of Applied Physics **132**, 160902 (2022).

[8] P. R. Sharapova, K. H. Luo, H. Herrmann, M. Reichelt, T. Meier, and C. Silberhorn, Toolbox for the design of LiNbO 3 -based passive and active integrated quantum circuits, New Journal of Physics **19**, 123009 (2017).

[9] J. Wang, F. Sciarrino, A. Laing, and M. G. Thompson, Integrated photonic quantum technologies, Nature Photonics **14**, 273–284 (2020).

[10] E. Pelucchi et al., The potential and global outlook of integrated photonics for quantum technologies, Nature Reviews Physics **4**, 194–208 (2021).

[11] D. V. Reddy, R. R. Nerem, S. W. Nam, R. P. Mirin, and V. B. Verma, Superconducting nanowire single-photon detectors with 98% system detection efficiency at 1550 nm, Optica **7**, 1649 (2020).

[12] J. Chang et al., Detecting telecom single photons with 99.5-2.07+0.5% system detection efficiency and high time resolution, APL Photonics **6**, 036114 (2021).

[13] B. Korzh et al., Demonstration of sub-3 ps temporal resolution with a superconducting nanowire single-photon detector, Nature Photonics **14**, 250–255 (2020).

[14] Y. Hochberg, I. Charaev, S. W. Nam, V. Verma, M. Colangelo, and K. K. Berggren, Detecting Sub-GeV Dark Matter with Superconducting Nanowires, Physical Review Letters **123**, 151802 (2019).

[15] S. Ferrari, C. Schuck, and W. Pernice, Waveguide-integrated superconducting nanowire single-photon detectors, Nanophotonics **7**, 1725–1758 (2018).

[16] C. M. Natarajan, M. G. Tanner, and R. H. Hadfield, Superconducting nanowire single-photon detectors: Physics and applications, Superconductor Science and Technology **25**, 10.1088/0953-2048/25/6/063001 (2012).

[17] D. Zhu et al., Integrated photonics on thin-film lithium niobate, Advances in Optics and Photonics **13**, 242 (2021).

[18] R. Weis and T. Gaylord, Lithium Niobate: Summary of Physical Properties and Crystal Structure, Appl. Phys. A **37**, 191–203 (1985).

[19] R. C. Alferness, Electrooptic Guided-Wave Device for General Polarization Transformations, IEEE Journal of Quantum Electronics **17**, 965–969 (1981).

[20] K. H. Luo, S. Brauner, C. Eigner, P. R. Sharapova, R. Ricken, T. Meier, H. Herrmann, and C. Silberhorn, Nonlinear integrated quantum electro-optic circuits, Science Advances **5**, 1–8 (2019).

[21] S. Babel et al., Demonstration of Hong-Ou-Mandel interference in an LNOI directional coupler, Optics Express **31**, 23140 (2023).

[22] P. I. Sund et al., High-speed thin-film lithium niobate quantum processor driven by a solid-state quantum emitter, Science Advances **9**, 1–9 (2023).

[23] C. M. Natarajan, M. G. Tanner, and R. H. Hadfield, Superconducting nanowire single-photon detectors: Physics and applications, Superconductor Science and Technology **25**, 10.1088/0953-2048/25/6/063001 (2012).

[24] A. Migdall, S. Polyakov, J. Fan, and J. Bienfang, "Single-Photon Generation and Detection", in *Single-photon generation and detection*, edited by T. Lucatorto, A. C. Parr, and K. Baldwin, 45th ed. (Elsevier, 2013), pp. 25–68.

[25] M. Bartnick, M. Santandrea, J. P. Höpker, F. Thiele, R. Ricken, V. Quiring, C. Eigner, H. Herrmann, C. Silberhorn, and T. J. Bartley, Cryogenic Second-Harmonic Generation in Periodically Poled Lithium Niobate Waveguides, Physical Review Applied **15**, 024028 (2021).

[26] N. A. Lange, J. P. Höpker, R. Ricken, V. Quiring, C. Eigner, C. Silberhorn, and T. J. Bartley, Cryogenic integrated spontaneous parametric down-conversion, Optica **9**, 108 (2022).

[27] K. Yoshida, Y. Kanda, and S. Kohjiro, A traveling-wave-type LiNbOs optical modulator with superconducting electrodes, IEEE Transactions on Microwave Theory and Techniques **47**, 1201–1205 (1999).

[28] K. McCammon, J.Morse, D. Masquelier, C. McConaghey, H. Garrett, K. Hugenberg, and M. Lowry, Fibre Optic Transceiver for Interfacing Digital Superconducting Electronics, DOD Fibre Optics and Photonics Conference (1994).

[29] R. Raussendorf and H. J. Briegel, A One-Way Quantum Computer, Physical Review Letters **86**, 5188–5191 (2001).

[30] J. L. O'Brien, Optical Quantum Computing, Science **318**, 1567–1570 (2007).

[31] S. Barz, Quantum computing with photons: introduction to the circuit model, the one-way quantum computer, and the fundamental principles of photonic experiments, Journal of Physics B: Atomic, Molecular and Optical Physics **48**, 083001 (2015).

[32] G. Moody et al., 2022 Roadmap on integrated quantum photonics, Journal of Physics: Photonics **4**, 012501 (2022).

[33] S. Ferrari, C. Schuck, and W. Pernice, Waveguide-integrated superconducting nanowire single-photon detectors, Nanophotonics **7**, 1725–1758 (2018).

[34] M. G. Tanner, L. S. E. Alvarez, W. Jiang, R. J. Warburton, Z. H. Barber, and R. H. Hadfield, A superconducting nanowire single photon detector on lithium niobate, Nanotechnology **23**, 505201 (2012).

[35] J. P. Höpker et al., Integrated superconducting nanowire single-photon detectors on titanium in-diffused lithium niobate waveguides, JPhys Photonics **3**, 10.1088/2515-7647/ac105b (2021).

[36] K. Yoshida, K. Ikeda, and Y. Kanda, LiNbO3 Optical Modulator with Superconducting Electrodes, IEICE TRANSACTIONS on Electronics **E75-C**, 894–899 (1992).

[37] J. Nye, *Physical Properties of Crystals* (Oxford University Press, 1957).

[38] J. Komma, C. Schwarz, G. Hofmann, D. Heinert, and R. Nawrodt, Thermo-optic coefficient of silicon at 1550 nm and cryogenic temperatures, Applied Physics Letters **101**, 041905 (2012).

[39] A. W. Elshaari, I. E. Zadeh, K. D. Jöns, and V. Zwiller, Thermo-Optic Characterization of Silicon Nitride Resonators for Cryogenic Photonic Circuits, IEEE Photonics Journal **8**, 10.1109/JPHOT.2016.2561622 (2016).

[40] M. Gehl, C. Long, D. Trotter, A. Starbuck, A. Pomerene, J. B. Wright, S. Melgaard, J. Siirola, A. L. Lentine, and C. DeRose, Operation of high-speed silicon photonic micro-disk modulators at cryogenic temperatures, Optica **4**, 374 (2017).

[41] P. Pintus et al., An integrated magneto-optic modulator for cryogenic applications, Nature Electronics **5**, 604–610 (2022).

[42] P. Pintus, A. Singh, W. Xie, L. Ranzani, M. V. Gustafsson, M. A. Tran, C. Xiang, J. Peters, J. E. Bowers, and M. Soltani, Ultralow voltage, high-speed, and energy-efficient cryogenic electro-optic modulator, Optica **9**, 1176 (2022).

[43] J. D. Morse, K. G. McCammon, C. F. McConaghy, D. A. Masquelier, H. E. Garrett, and M. E. Lowry, "Characterization of Lithium Niobate Electro-Optic Modulators at Cryogenic Temperatures", in Proc. spie, edited by M. N. Armenise (1994), pp. 283–291.

[44] A. Yariv, Coupled-mode theory for guided-wave optics, IEEE Journal of Quantum Electronics **9**, 919–933 (1973).

[45] R. C. Alferness, Waveguide Electrooptic Modulators, IEEE Transactions on Microwave Theory and Techniques **30**, 1121–1137 (1982).

[46] A. Honardoost, R. Safian, A. Rao, and S. Fathpour, High-speed modeling of ultracompact electrooptic modulators, Journal of Lightwave Technology **36**, 5893–5902 (2018).

[47] V. Narayanan, M. M. Frank, and A. A. Demkov, *Thin Films on Silicon*, Vol. 8, Materials and Energy (WORLD SCIENTIFIC, 2016).

[48] F. Eltes et al., An integrated optical modulator operating at cryogenic temperatures, Nature Materials **19**, 1164–1168 (2020).

[49] H. Gevorgyan, A. Khilo, D. Van Orden, D. Onural, B. Yin, M. T. Wade, V. M. Stojanović, and M. A. Popović, "Cryo-Compatible, Silicon Spoked-Ring Modulator in a 45nm CMOS Platform for 4K-to-Room-Temperature Optical Links", in Optical fiber communication conference (ofc) 2021, M3B (2021), M3B.3.

[50] B. Yin, H. Gevorgyan, D. Onural, A. Khilo, M. A. Popovic, and V. M. Stojanovic, "Electronic-Photonic Cryogenic Egress Link", in Essderc 2021 - ieee 51st european solid-state device research conference (essderc), Vol. 2021-Septe (2021), pp. 51–54.

[51] M. de Cea, E. E. Wollman, A. H. Atabaki, D. J. Gray, M. D. Shaw, and R. J. Ram, Photonic Readout of Superconducting Nanowire Single Photon Counting Detectors, Scientific Reports **10**, 9470 (2020).

[52] P. R. Stanfield, A. J. Leenheer, C. P. Michael, R. Sims, and M. Eichenfield, CMOS-compatible, piezo-optomechanically tunable photonics for visible wavelengths and cryogenic temperatures, Optics Express **27**, 28588 (2019).

[53] M. Dong, G. Clark, A. J. Leenheer, M. Zimmermann, D. Dominguez, A. J. Menssen, D. Heim, G. Gilbert, D. Englund, and M. Eichenfield, High-speed programmable photonic circuits in a cryogenically compatible, visible–near-infrared 200 mm CMOS architecture, Nature Photonics **16**, 59–65 (2022).

[54] F. Beutel, T. Grottke, M. A. Wolff, C. Schuck, and W. H. P. Pernice, Cryo-compatible opto-mechanical low-voltage phase-modulator integrated with superconducting single-photon detectors, Optics Express **30**, 30066 (2022).

[55] S. Gyger, J. Zichi, L. Schweickert, A. W. Elshaari, S. Steinhauer, S. F. Covre da Silva, A. Rastelli, V. Zwiller, K. D. Jöns, and C. Errando-Herranz, Reconfigurable photonics with on-chip single-photon detectors, Nature Communications **12**, 1–8 (2021).

[56] B. S. Lee, B. Kim, A. P. Freitas, A. Mohanty, Y. Zhu, G. R. Bhatt, J. Hone, and M. Lipson, High-performance integrated graphene electro-optic modulator at cryogenic temperature, Nanophotonics **10**, 99–104 (2020).

[57] A. Schwarzenberger et al., Cryogenic Operation of a Silicon-Organic Hybrid (SOH) Modulator at 50 Gbit/s and 4 K Ambient Temperature, 2022 European Conference on Optical Communication, ECOC 2022 **2** (2022).

[58] E. Lomonte, M. A. Wolff, F. Beutel, S. Ferrari, C. Schuck, W. H. P. Pernice, and F. Lenzini, Single-photon detection and cryogenic reconfigurability in lithium niobate nanophotonic circuits, Nature Communications **12**, 6847 (2021).

[59] A. Youssefi, I. Shomroni, Y. J. Joshi, N. Bernier, A. Lukashchuk, P. Uhrich, L. Qiu, and T. J. Kippenberg, Cryogenic electro-optic interconnect for superconducting devices, Nature Communications, 1–8 (2020).

[60] N. A. Lange, T. Schapeler, J. P. Höpker, M. Protte, and T. J. Bartley, Degenerate Photons from a Cryogenic Spontaneous Parametric Down-Conversion Source, arxive, 2303.17428 (2023).

[61] J. P. Höpker et al., Integrated transition edge sensors on titanium in-diffused lithium niobate waveguides, APL Photonics **4**, 10.1063/1.5086276 (2019).

[62] N. Montaut, L. Sansoni, E. Meyer-Scott, R. Ricken, V. Quiring, H. Herrmann, and C. Silberhorn, High-Efficiency Plug-and-Play Source of Heralded Single Photons, Physical Review Applied **8**, 024021 (2017).

[63] S. L. Bravina and N. V. Morozovsky, Pyroelectricity in some ferroelectric semiconductors and its applications, Ferroelectrics **118**, 217–224 (1991).

[64] S. L. Bravina, A. N. Morozovska, N. V. Morozovsky, and Y. A. Skryshevsky, Low-temperature pyroelectric phenomena in lithium niobate single crystals, Ferroelectrics **298**, 31–42 (2004).

[65] S. L. Bravina, N. V. Morozovsky, A. N. Morozovska, S. Gille, J. P. Salvestrini, and M. D. Fontana, Investigations of LiNbO3 and LiTaO3 single crystals for pyroelectric applications in the wide temperature range, Ferroelectrics **353**, 202–211 (2007).

[66] G. Chen, N. Li, J. D. Ng, H. L. Lin, Y. Zhou, Y. H. Fu, L. Y. T. Lee, Y. Yu, A. Q. Liu, and A. J. Danner, Advances in lithium niobate photonics: development status and perspectives, Advanced Photonics **4**, 1–43 (2022).

[67] A. N. R. Ahmed, S. Nelan, S. Shi, P. Yao, A. Mercante, and D. W. Prather, Subvolt electro-optical modulator on thin-film lithium niobate and silicon nitride hybrid platform, Optics Letters **45**, 1112 (2020).

[68] L. Chang, Y. Li, N. Volet, L. Wang, J. Peters, and J. E. Bowers, Thin film wavelength converters for photonic integrated circuits, Optica **3**, 531 (2016).

[69] L. Ledezma, R. Sekine, Q. Guo, R. Nehra, S. Jahani, and A. Marandi, Intense optical parametric amplification in dispersion-engineered nanophotonic lithium niobate waveguides, Optica **9**, 303 (2022).

[70] S. Aghaeimeibodi, B. Desiatov, J. H. Kim, C. M. Lee, M. A. Buyukkaya, A. Karasahin, C. J. Richardson, R. P. Leavitt, M. Lončar, and E. Waks, Integration of quantum dots with lithium niobate photonics, Applied Physics Letters **113**, 10.1063/1.5054865 (2018).

[71] A. A. Sayem, R. Cheng, S. Wang, and H. X. Tang, Lithium-niobate-on-insulator waveguide-integrated superconducting nanowire single-photon detectors, Applied Physics Letters **116**, 10.1063/1.5142852 (2020).

[72] E. Lomonte, F. Lenzini, and W. H. P. Pernice, Efficient self-imaging grating couplers on a lithium-niobate-on-insulator platform at near-visible and telecom wavelengths, Optics Express **29**, 20205 (2021).

[73] J. W. Silverstone et al., On-chip quantum interference between silicon photon-pair sources, Nature Photonics **8**, 104–108 (2014).

[74] S. Hepp, M. Jetter, S. L. Portalupi, and P. Michler, Semiconductor Quantum Dots for Integrated Quantum Photonics, Advanced Quantum Technologies **2**, 1900020 (2019).

[75] P. Pintus et al., An integrated magneto-optic modulator for cryogenic applications, Nature Electronics **5**, 604–610 (2022).

[76] I. Marinković, M. Drimmer, B. Hensen, and S. Gröblacher, Hybrid Integration of Silicon Photonic Devices on Lithium Niobate for Optomechanical Wavelength Conversion, Nano Letters **21**, 529–535 (2021).

[77] S. Mookherjea, V. Mere, and F. Valdez, Thin-film lithium niobate electro-optic modulators: To etch or not to etch, Applied Physics Letters **122**, 120501 (2023).

[78] R. Marchetti, C. Lacava, L. Carroll, K. Gradkowski, and P. Minzioni, Coupling strategies for silicon photonics integrated chips [Invited], Photonics Research **7**, 201 (2019).

[79] W. Sohler et al., Integrated Optical Devices in Lithium Niobate, Optics and Photonics News **19**, 24 (2008).

[80] Norland, *Norland Optical Adhesive 81*, 2023.

[81] W. W. Wasserman, R. A. Harrison, G. I. Harris, A. Sawadsky, Y. L. Sfendla, W. P. Bowen, and C. G. Baker, Cryogenic and hermetically sealed packaging of photonic chips for optomechanics, Optics Express **30**, 30822 (2022).

[82] Apiezon, *Apiezon N Grease*, 2023.

[83] C. Herzog, G. Poberaj, and P. Günter, Electro-optic behavior of lithium niobate at cryogenic temperatures, Optics Communications **281**, 793–796 (2008).

[84] Rsoft, *BeamPROP: BPM Software for Waveguide and Circuit Design*, 2019.

[85] D. H. Jundt, Temperature-dependent Sellmeier equation for the index of refraction, n_e, in congruent lithium niobate, Optics Letters **22**, 1553 (1997).

[86] S. Dello Russo, A. Elefante, D. Dequal, D. K. Pallotti, L. Santamaria Amato, F. Sgobba, and M. Siciliani de Cumis, Advances in Mid-Infrared Single-Photon Detection, Photonics **9**, 470 (2022).

[87] F. Ceccarelli, G. Acconcia, A. Gulinatti, M. Ghioni, I. Rech, and R. Osellame, Recent Advances and Future Perspectives of Single-Photon Avalanche Diodes for Quantum

Photonics Applications, Advanced Quantum Technologies **4**, 10.1002/qute.202000102 (2021).

[88] R. H. Hadfield and G. Johansson, eds., *Superconducting Devices in Quantum Optics*, Quantum Science and Technology (Springer International Publishing, Cham, 2016), pp. 3–30.

[89] I. Holzman and Y. Ivry, Superconducting Nanowires for Single-Photon Detection: Progress, Challenges, and Opportunities, Advanced Quantum Technologies **2**, 1–28 (2019).

[90] I. Esmaeil Zadeh, J. Chang, J. W. N. Los, S. Gyger, A. W. Elshaari, S. Steinhauer, S. N. Dorenbos, and V. Zwiller, Superconducting nanowire single-photon detectors: A perspective on evolution, state-of-the-art, future developments, and applications, Applied Physics Letters **118**, 190502 (2021).

[91] Z. L. Yuan, J. F. Dynes, and A. J. Shields, Resilience of gated avalanche photodiodes against bright illumination attacks in quantum cryptography, Applied Physics Letters **98**, 231104 (2011).

[92] M. Barbieri, Optical Quantum Metrology, PRX Quantum **3**, 010202 (2022).

[93] R. Prevedel, P. Walther, F. Tiefenbacher, P. Böhi, R. Kaltenbaek, T. Jennewein, and A. Zeilinger, High-speed linear optics quantum computing using active feed-forward, Nature **445**, 65–69 (2007).

[94] E. A. Webster, L. A. Grant, and R. K. Henderson, A high-performance single-photon avalanche diode in 130-nm CMOS imaging technology, IEEE Electron Device Letters **33**, 1589–1591 (2012).

[95] M. Sanzaro, P. Gattari, F. Villa, A. Tosi, G. Croce, and F. Zappa, Single-Photon Avalanche Diodes in a 0.16 μm BCD Technology With Sharp Timing Response and Red-Enhanced Sensitivity, IEEE Journal of Selected Topics in Quantum Electronics **24**, 1–9 (2018).

[96] J. Zhang et al., Hybrid and heterogeneous photonic integrated near-infrared InGaAs/InAlAs single-photon avalanche diode, Quantum Science and Technology **8**, 10.1088/2058-9565/acb730 (2023).

[97] G. N. Gol'tsman, O. Okunev, G. Chulkova, A. Lipatov, A. Semenov, K. Smirnov, B. Voronov, A. Dzardanov, C. Williams, and R. Sobolewski, Picosecond superconducting single-photon optical detector, Applied Physics Letters **79**, 705–707 (2001).

[98] A. D. Semenov, G. N. Gol'tsman, and A. A. Korneev, Quantum detection by current carrying superconducting film, Physica C: Superconductivity **351**, 349–356 (2001).

[99] J. K. Yang, A. J. Kerman, E. A. Dauler, V. Anant, K. M. Rosfjord, and K. K. Berggren, Modeling the electrical and thermal response of superconducting nanowire single-photon detectors, IEEE Transactions on Applied Superconductivity **17**, 581–585 (2007).

[100] A. J. Kerman, J. K. Yang, R. J. Molnar, E. A. Dauler, and K. K. Berggren, Electrothermal feedback in superconducting nanowire single-photon detectors, Physical Review B - Condensed Matter and Materials Physics **79**, 10.1103/PhysRevB.79.100509 (2009).

[101] K. K. Berggren, Q.-Y. Zhao, N. Abebe, M. Chen, P. Ravindran, A. McCaughan, and J. C. Bardin, A superconducting nanowire can be modeled by using SPICE, Superconductor Science and Technology **31**, 055010 (2018).

[102] M. Häußler, M. Y. Mikhailov, M. A. Wolff, and C. Schuck, Amorphous superconducting nanowire single-photon detectors integrated with nanophotonic waveguides, APL Photonics **5**, 076106 (2020).

[103] M. A. Wolff, F. Beutel, J. Schütte, H. Gehring, M. Häußler, W. Pernice, and C. Schuck, Broadband waveguide-integrated superconducting single-photon detectors with high system detection efficiency, Applied Physics Letters **118**, 10.1063/5.0046057 (2021).

[104] M. Sidorova, A. Semenov, H.-w. Hübers, I. Charaev, A. Kuzmin, S. Doerner, and M. Siegel, Physical mechanisms of timing jitter in photon detection by current-carrying superconducting nanowires, Physical Review B **96**, 184504 (2017).

[105] J. Münzberg, A. Vetter, F. Beutel, W. Hartmann, S. Ferrari, W. H. P. Pernice, and C. Rockstuhl, Superconducting nanowire single-photon detector implemented in a 2D photonic crystal cavity, Optica **5**, 658 (2018).

[106] F. Najafi et al., On-chip detection of non-classical light by scalable integration of single-photon detectors, Nature Communications **6**, 10.1038/ncomms6873 (2015).

[107] S. Chen et al., Stacking two superconducting nanowire single-photon detectors via membrane microchip transfer, Applied Physics Letters **121**, 112601 (2022).

[108] C. Cahall, K. L. Nicolich, N. T. Islam, G. P. Lafyatis, A. J. Miller, D. J. Gauthier, and J. Kim, Multi-photon detection using a conventional superconducting nanowire single-photon detector, Optica **4**, 1534 (2017).

[109] D. Zhu, M. Colangelo, C. Chen, B. A. Korzh, F. N. C. Wong, M. D. Shaw, and K. K. Berggren, Resolving Photon Numbers Using a Superconducting Nanowire with Impedance-Matching Taper, Nano Letters **20**, 3858–3863 (2020).

[110] T. Schapeler and T. J. Bartley, Information extraction in photon-counting experiments, Physical Review A **106**, 013701 (2022).

[111] E. E. Wollman, V. B. Verma, A. E. Lita, W. H. Farr, M. D. Shaw, R. P. Mirin, and S. Woo Nam, Kilopixel array of superconducting nanowire single-photon detectors, Optics Express **27**, 35279 (2019).

[112] B. G. Oripov, D. S. Rampini, J. Allmaras, M. D. Shaw, S. W. Nam, B. Korzh, and A. N. McCaughan, A superconducting-nanowire single-photon camera with 400,000 pixels, **arxive**, 1–19 (2023).

[113] M. Ejrnaes, A. Casaburi, O. Quaranta, S. Marchetti, A. Gaggero, F. Mattioli, R. Leoni, S. Pagano, and R. Cristiano, Large Signal Amplitude and Bias Range of Cascade Switch Superconducting Nanowire Single Photon Detectors, IEEE Transactions on Applied Superconductivity **19**, 323–326 (2009).

[114] R. Arpaia, M. Ejrnaes, L. Parlato, F. Tafuri, R. Cristiano, D. Golubev, R. Sobolewski, T. Bauch, F. Lombardi, and G. Pepe, High-temperature superconducting nanowires for photon detection, Physica C: Superconductivity and its Applications **509**, 16–21 (2015).

[115] I. Charaev et al., Single-photon detection using high-temperature superconductors, Nature Nanotechnology **18**, 343–349 (2023).

[116] R. L. Merino, P. Seifert, J. D. Retamal, R. K. Mech, T. Taniguchi, K. Watanabe, K. Kadowaki, R. H. Hadfield, and D. K. Efetov, Two-dimensional cuprate nanodetector with single telecom photon sensitivity at T = 20 K, 2D Materials **10**, 021001 (2023).

[117] T. Hummel, A. Widhalm, J. P. Höpker, K. D. Jöns, J. Chang, A. Fognini, S. Steinhauer, V. Zwiller, A. Zrenner, and T. J. Bartley, Nanosecond gating of superconducting nanowire single-photon detectors using cryogenic bias circuitry, Optics Express **31**, 610 (2023).

[118] E. Bardalen, B. Karlsen, H. Malmbekk, M. N. Akram, and P. Ohlckers, Evaluation of InGaAs/InP photodiode for high-speed operation at 4 K, International Journal of Metrology and Quality Engineering **9**, 13–17 (2018).

[119] C. M. Gentry et al., "Monolithic Source of Entangled Photons with Integrated Pump Rejection", in Conference on lasers and electro-optics (2018), JTh4C.3.

[120] F. Dreher, *Overcoming pyroelectric damage to integrated superconducting detectors on lithium niobate waveguides*, 2022.

[121] E. Lomonte, F. Lenzini, S. Ferrari, M. Wolff, C. Schuck, and W. Pernice, On-chip manipulation and detection of single photons in lithium niobate nanophotonic

circuits, International Conference on Transparent Optical Networks **2020-July**, 1–4 (2020).

[122] J. Ekin, *Experimental Techniques for Low-Temperature Measurements: Cryostat Design, Material Properties and Superconductor Critical-Current Testing* (Oxford University Press, 2006).

[123] S. Krinner, S. Storz, P. Kurpiers, P. Magnard, J. Heinsoo, R. Keller, J. Lütolf, C. Eichler, and A. Wallraff, Engineering cryogenic setups for 100-qubit scale superconducting circuit systems, EPJ Quantum Technology **6**, 2 (2019).

[124] Lakeshore, *Lakeshore SMA cables*, 2023.

[125] R. Franz and G. Wiedemann, Ueber die Wärme-Leitungsfähigkeit der Metalle, Annalen der Physik und Chemie **165**, 497–531 (1853).

[126] V. Anant, *Photonspot*, 2023.

[127] R. Sobolewski, Ultrafast optoelectronic interface for digital superconducting electronics, Superconductor Science and Technology **14**, 994–1000 (2001).

[128] B. Karlsen, O. Kieler, R. Behr, T. A. Tuan Nguyen, H. Malmbekk, M. N. Akram, and P. Ohlckers, Pulsation of InGaAs Photodiodes in Liquid Helium for Driving Josephson Arrays in AC Voltage Realization, IEEE Transactions on Applied Superconductivity **29**, 10.1109/TASC.2019.2901573 (2019).

[129] J.-W. Shi, *Photodiodes - Communications, Bio-Sensings, Measurements and High-Energy Physics*, edited by J.-W. Shi (InTech, 2011).

[130] Y. Zhang, V. Borzenets, N. Dubash, T. Reynolds, Y. Wey, and J. Bowers, Cryogenic performance of a high-speed GaInAs/InP p-i-n photodiode, Journal of Lightwave Technology **15**, 529–533 (1997).

[131] F. Lecocq, F. Quinlan, K. Cicak, J. Aumentado, S. A. Diddams, and J. D. Teufel, Control and readout of a superconducting qubit using a photonic link, Nature **591**, 575–579 (2021).

[132] A. M. Hennel, Temperature dependence of the energy gap in GaAs, Physica Status Solidi (a) **8**, K111–K113 (1971).

[133] M. K. Akhlaghi and A. H. Majedi, Gated mode superconducting nanowire single photon detectors, Optics Express **20**, 1608 (2012).

[134] S. Doerner, A. Kuzmin, S. Wuensch, K. Ilin, and M. Siegel, Operation of Superconducting Nanowire Single-Photon Detectors Embedded in Lumped-Element Resonant

Circuits, IEEE Transactions on Applied Superconductivity **26**, 10.1109/TASC.2016.2525995 (2016).

[135] S. Doerner, A. Kuzmin, S. Wuensch, and M. Siegel, Comparison of snspds biased with microwave and direct currents, IEEE Transactions on Applied Superconductivity **29**, 2019–2022 (2019).

[136] E. Knehr, A. Kuzmin, S. Doerner, S. Wuensch, K. Ilin, H. Schmidt, and M. Siegel, Synchronous single-photon detection with self-resetting, GHz-gated superconducting NbN nanowires, Applied Physics Letters **117**, 132602 (2020).

[137] F. Liu, M. S. Jiang, Y. F. Lu, Y. Wang, and W. S. Bao, Pulse-gated mode of commercial superconducting nanowire single photon detectors, Chinese Physics B **30**, 40302 (2021).

[138] C. Schuck, W. H. Pernice, X. Ma, and H. X. Tang, Optical time domain reflectometry with low noise waveguide-coupled superconducting nanowire single-photon detectors, Applied Physics Letters **102**, 191104 (2013).

[139] L. Zhang, S. Zhang, X. Tao, G. Zhu, L. Kang, J. Chen, and P. Wu, Quasi-Gated Superconducting Nanowire Single-Photon Detector, IEEE Transactions on Applied Superconductivity **27**, 2201206 (2017).

[140] SPICE, *LT SPICE*, 2023.

[141] K. Kennerud, Analysis of Performance Degradation in CdS Solar Cells, IEEE Transactions on Aerospace and Electronic Systems **AES-5**, 912–917 (1969).

[142] J. Cubas, S. Pindado, and C. de Manuel, "New Method for Analytical Photovoltaic Parameters Identification: Meeting Manufacturer's Datasheet for Different Ambient Conditions", in *Springer proceedings in physics*, Vol. 155 (2014), pp. 161–169.

[143] K. N'Detigma, D. Djicknoum, M. S. Y., D. Arouna, and S. M. Amadou, Module parameter extraction and simulation with LTSpice software model in sub-Saharan outdoor conditions, African Journal of Environmental Science and Technology **12**, 523–531 (2018).

[144] Bo Lu, Yin-Chen Lu, J. Cheng, R. Schneider, J. Zolper, and G. Goncher, Gigabit-per-second cryogenic optical link using optimized low-temperature AlGaAs-GaAs vertical-cavity surface-emitting lasers, IEEE Journal of Quantum Electronics **32**, 1347–1359 (1996).

[145] W. Fu, H. Wu, D. Wu, M. Feng, and D. Deppe, Cryogenic Oxide-VCSEL for PAM-4 Optical Data Transmission Over 50 Gb/s at 77 K, IEEE Photonics Technology Letters **33**, 816–819 (2021).

[146] R. Sahu, W. Hease, A. Rueda, G. Arnold, L. Qiu, and J. M. Fink, Quantum-enabled operation of a microwave-optical interface, Nature Communications **13**, 1276 (2022).

[147] F. Thiele, T. Hummel, F. vom Bruch, V. Quiring, R. Ricken, H. Herrmann, C. Eigner, C. Silberhorn, and T. J. Bartley, "Optical readout of a superconducting single photon detector with a cryogenic modulator", in 2021 conference on lasers and electro-optics europe and european quantum electronics conference (2021), eb_2_5.

[148] R. Regener and W. Sohler, Loss in low-finesse Ti:LiNbO3 optical waveguide resonators, Applied Physics B Photophysics and Laser Chemistry **36**, 143–147 (1985).

[149] J. Schleeh, G. Alestig, J. Halonen, A. Malmros, B. Nilsson, P. A. Nilsson, J. P. Starski, N. Wadefalk, H. Zirath, and J. Grahn, Ultralow-power cryogenic InP HEMT with minimum noise temperature of 1 K at 6 GHz, IEEE Electron Device Letters **33**, 664–666 (2012).

[150] A. H. Akgiray, S. Weinreb, R. Leblanc, M. Renvoise, P. Frijlink, R. Lai, and S. Sarkozy, Noise measurements of discrete HEMT transistors and application to wideband very low-noise amplifiers, IEEE Transactions on Microwave Theory and Techniques **61**, 3285–3297 (2013).

[151] E. Cha, N. Wadefalk, G. Moschetti, A. Pourkabirian, J. Stenarson, and J. Grahn, InP HEMTs for Sub-mW Cryogenic Low-Noise Amplifiers, IEEE Electron Device Letters **41**, 1005–1008 (2020).

[152] R. Krithivasan, Y. Lu, L. Najafizadeh, C. Zhu, J. D. Cressler, S. Chen, C. Ulaganathan, and B. J. Blalock, A high-slew rate SiGe BiCMOS operational amplifier for operation down to deep cryogenic temperatures, Proceedings of the IEEE Bipolar/BiCMOS Circuits and Technology Meeting, 6–9 (2006).

[153] W. Ramírez, H. Forstén, M. Varonen, R. Reeves, M. Kantanen, K. Mehmet, and S. Torres, Cryogenic Operation of a Millimeter-Wave SiGe BiCMOS Low-Noise Amplifier, IEEE Microwave and Wireless Components Letters **29**, 403–405 (2019).

[154] M. Varonen, N. Sheikhipoor, B. Gabritchidze, K. Cleary, H. Forsten, H. Rucker, and M. Kaynak, Cryogenic W-Band SiGe BiCMOS low-noise amplifier, IEEE MTT-S International Microwave Symposium Digest **2020-Augus**, 185–188 (2020).

[155] E. Wolf, A. Gerald, M. Gurvitch, and J. Zasadzinski, *Josephson Junctions History, Devices, and Application*, edited by E. Wolf, G. Arnold, M. Gurvitch, and J. Zasadzinski (Jenny Stanford Publishing, 2017), pp. 1–23.

[156] A. Kirste, A. Semenov, H. W. Hiibers, D. Drung, M. Peters, T. Schurig, K. S. Il'in, and M. Siegel, SQUID-readout for the superconducting nanowire single-photon detector, IEEE Transactions on Applied Superconductivity **19**, 313–317 (2009).

[157] A. N. McCaughan, V. B. Verma, S. M. Buckley, J. P. Allmaras, A. G. Kozorezov, A. N. Tait, S. W. Nam, and J. M. Shainline, A superconducting thermal switch with ultrahigh impedance for interfacing superconductors to semiconductors, Nature Electronics **2**, 451–456 (2019).

[158] V. B. Verma, A. E. Lita, M. J. Stevens, R. P. Mirin, and S. W. Nam, Athermal avalanche in bilayer superconducting nanowire single-photon detectors, Applied Physics Letters **108**, 10.1063/1.4945595 (2016).

[159] R. Baghdadi, J. P. Allmaras, B. A. Butters, A. E. Dane, S. Iqbal, A. N. McCaughan, E. A. Toomey, Q. Y. Zhao, A. G. Kozorezov, and K. K. Berggren, Multilayered Heater Nanocryotron: A Superconducting-Nanowire-Based Thermal Switch, Physical Review Applied **14**, 1 (2020).

[160] A. N. McCaughan and K. K. Berggren, A Superconducting-Nanowire Three-Terminal Electrothermal Device, Nano Letters **14**, 5748–5753 (2014).

[161] S. Pagano, N. Martucciello, R. Cristiano, M. Ejrnaes, A. Casaburi, R. Leoni, A. Gaggero, F. Mattioli, J. C. Villegier, and P. Cavalier, Nano-strip three-terminal superconducting device for cryogenic detector readout, IEEE Transactions on Applied Superconductivity **21**, 717–720 (2011).

[162] K. Zheng et al., Characterize the switching performance of a superconducting nanowire cryotron for reading superconducting nanowire single photon detectors, Scientific Reports **9**, 1–8 (2019).

[163] Q.-Y. Zhao, A. N. McCaughan, A. E. Dane, K. K. Berggren, and T. Ortlepp, A nanocryotron comparator can connect single-flux-quantum circuits to conventional electronics, Superconductor Science and Technology **30**, 044002 (2017).

[164] M. Castellani, O. Medeiros, R. A. Foster, A. Buzzi, M. Colangelo, J. C. Bienfang, A. Restelli, and K. K. Berggren, A Nanocryotron Ripple Counter Integrated with a Superconducting Nanowire Single-Photon Detector for Megapixel Arrays, arxive **2304.11700**, 1 (2023).

[165] H. S. Zhong et al., Quantum computational advantage using photons, Science **370**, 1460–1463 (2020).

[166] P. Walther, K. J. Resch, T. Rudolph, E. Schenck, H. Weinfurter, V. Vedral, M. Aspelmeyer, and A. Zeilinger, Experimental one-way quantum computing, Nature **434**, 169–176 (2005).

[167] R. Schiek, I. Baumann, W. Sohler, Y. Baek, G. Krijnen, and G. I. Stegeman, All-optical switching in lithium niobate directional couplers with cascaded nonlinearity, Optics Letters **21**, 940 (1996).

[168] V. Sasikala and K. Chitra, All optical switching and associated technologies: a review, Journal of Optics **47**, 307–317 (2018).

[169] M. Grimau Puigibert, G. H. Aguilar, Q. Zhou, F. Marsili, M. D. Shaw, V. B. Verma, S. W. Nam, D. Oblak, and W. Tittel, Heralded Single Photons Based on Spectral Multiplexing and Feed-Forward Control, Physical Review Letters **119**, 083601 (2017).

[170] E. Meyer-Scott, N. Prasannan, I. Dhand, C. Eigner, V. Quiring, S. Barkhofen, B. Brecht, M. B. Plenio, and C. Silberhorn, Scalable Generation of Multiphoton Entangled States by Active Feed-Forward and Multiplexing, Physical Review Letters **129**, 150501 (2022).

[171] T. B. Pittman, B. C. Jacobs, and J. D. Franson, Demonstration of feed-forward control for linear optics quantum computation, Physical Review A - Atomic, Molecular, and Optical Physics **66**, 7 (2002).

[172] M. Miková, H. Fikerová, I. Straka, M. Mičuda, J. Fiurášek, M. Ježek, and M. Dušek, Increasing efficiency of a linear-optical quantum gate using electronic feed-forward, Physical Review A - Atomic, Molecular, and Optical Physics **85**, 1–4 (2012).

[173] J. Zeuner, A. N. Sharma, M. Tillmann, R. Heilmann, M. Gräfe, A. Moqanaki, A. Szameit, and P. Walther, Integrated-optics heralded controlled-NOT gate for polarization-encoded qubits, npj Quantum Information **4**, 10.1038/s41534-018-0068-0 (2018).

[174] G. Luiz Zanin, M. J. Jacquet, M. Spagnolo, P. Schiansky, I. A. Calafell, L. A. Rozema, and P. Walther, Fiber-compatible photonic feed-forward with 99% fidelity, Optics Express **29**, 3425 (2021).

[175] P. Kharel, C. Reimer, K. Luke, L. He, and M. Zhang, Breaking voltage-bandwidth limits in integrated lithium niobate modulators using micro-structured electrodes: erratum, Optica **8**, 1218 (2021).

[176] F. Marsili et al., Detecting single infrared photons with 93% system efficiency, Nature Photonics **7**, 210–214 (2013).

[177] B. A. Korzh, Q.-y. Zhao, S. Frasca, J. P. Allmaras, T. M. Autry, and E. A. Bersin, *Demonstrating sub-3 ps temporal resolution in a superconducting nanowire single-photon detector*, 2018.

[178] N. C. Harris, Y. Ma, J. Mower, T. Baehr-Jones, D. Englund, M. Hochberg, and C. Galland, Efficient, compact and low loss thermo-optic phase shifter in silicon, Optics Express **22**, 10487 (2014).

[179] C. McConaghy, M. Lowry, R. A. Becker, and B. E. Kincaid, The performance of pigtailed annealed proton exchange LiNbO3 modulators at cryogenic temperatures, IEEE Photonics Technology Letters **8**, 1480–1482 (1996).

[180] R. C. Alferness, Efficient waveguide electro-optic TE TM mode converter/wavelength filter, Applied Physics Letters **36**, 513–515 (1980).

[181] S. Thaniyavarn, Wavelength independent, optical damage immune Z -propagation LiNbO3 waveguide polarization converter, Applied Physics Letters **47**, 674–677 (1985).

[182] Y.-Q. Lu, Z.-L. Wan, Q. Wang, Y.-X. Xi, and N.-B. Ming, Electro-optic effect of periodically poled optical superlattice LiNbO3 and its applications, Applied Physics Letters **77**, 3719–3721 (2000).

[183] C. Y. Huang, C. H. Lin, Y. H. Chen, and Y. C. Huang, Electro-optic Ti:PPLN waveguide as efficient optical wavelength filter and polarization mode converter, Optics Express **15**, 2548 (2007).

[184] N. Moeini, H. Herrmann, R. Ricken, V. Quiring, and W. Sohler, Electro-Optic Polarization Controller With Ti : PPLN Channel Waveguides, Ecio, 3–4 (2010).

[185] T. Izuhara, R. Roth, R. Osgood, S. Bakhru, and H. Bakhru, Low-voltage tunable TE/TM converter on ion-sliced lithium niobate thin film, Electronics Letters **39**, 1118 (2003).

[186] T. Ding, Y. Zheng, and X. Chen, On-Chip Solc-Type Polarization Control and Wavelength Filtering Utilizing Periodically Poled Lithium Niobate on Insulator Ridge Waveguide, Journal of Lightwave Technology **37**, 1296–1300 (2019).

[187] G. Kötitz, *Properties of lithium niobate*, 1st ed., Vol. 25, 6 (INSPEC, The Institution of Electrical Engineering, 1990), pp. 720–720.

[188] F. Thiele, *Supplementary material Video*, 2020.

[189] N. Gisin and R. Thew, Quantum communication, Nature Photonics **1**, 165–171 (2007).

[190] E. Polino, M. Valeri, N. Spagnolo, and F. Sciarrino, Photonic quantum metrology, AVS Quantum Science **2**, 024703 (2020).

[191] C. You et al., Scalable multiphoton quantum metrology with neither pre- nor post-selected measurements, Applied Physics Reviews **8**, 041406 (2021).

[192] S. Bogdanov, M. Y. Shalaginov, A. Boltasseva, and V. M. Shalaev, Material platforms for integrated quantum photonics, Optical Materials Express **7**, 111 (2017).

[193] A. W. Elshaari, W. Pernice, K. Srinivasan, O. Benson, and V. Zwiller, Hybrid integrated quantum photonic circuits, Nature Photonics **14**, 285–298 (2020).

[194] J.-H. Kim, S. Aghaeimeibodi, J. Carolan, D. Englund, and E. Waks, Hybrid integration methods for on-chip quantum photonics, Optica **7**, 291 (2020).

[195] M. Zhang, C. Wang, P. Kharel, D. Zhu, and M. Loncar, Integrated lithium niobate electro-optic modulators: when performance meets scalability, Optica **8**, 10.1364/optica.415762 (2021).

[196] O. Alibart, V. D'Auria, M. D. Micheli, F. Doutre, F. Kaiser, L. Labonté, T. Lunghi, É. Picholle, and S. Tanzilli, Quantum photonics at telecom wavelengths based on lithium niobate waveguides, Journal of Optics **18**, 104001 (2016).

[197] P. R. Sharapova, K. H. Luo, H. Herrmann, M. Reichelt, T. Meier, and C. Silberhorn, Toolbox for the design of LiNbO3-based passive and active integrated quantum circuits, New Journal of Physics **19**, 123009 (2017).

[198] E. Smirnov, A. Golikov, P. Zolotov, V. Kovalyuk, M. Lobino, B. Voronov, A. Korneev, and G. Goltsman, "Superconducting nanowire single-photon detector on lithium niobate", in Journal of physics: conference series, Vol. 1124 (2018), p. 051025.

[199] M. Colangelo, B. Desiatov, D. Zhu, J. Holzgrafe, O. Medeiros, M. Loncar, and K. K. Berggren, Superconducting nanowire single-photon detector on thin-film lithium niobate photonic waveguide, Conference on Lasers and Electro-Optics 2020 **SM4O.4** (2020).

[200] A. Youssefi, I. Shomroni, Y. J. Joshi, N. R. Bernier, A. Lukashchuk, P. Uhrich, L. Qiu, and T. J. Kippenberg, A cryogenic electro-optic interconnect for superconducting devices, Nature Electronics **4**, 326–332 (2021).

[201] T. P. McKenna, J. D. Witmer, R. N. Patel, W. Jiang, R. Van Laer, P. Arrangoiz-Arriola, E. A. Wollack, J. F. Herrmann, and A. H. Safavi-Naeini, Cryogenic microwave-to-optical conversion using a triply resonant lithium-niobate-on-sapphire transducer, Optica **7**, 1737 (2020).

[202] U. Chakraborty, J. Carolan, G. Clark, D. Bunandar, G. Gilbert, J. Notaros, M. R. Watts, and D. R. Englund, Cryogenic operation of silicon photonic modulators based on the DC Kerr effect, Optica **7**, 1385 (2020).

[203] C. Kim and R. Ramaswamy, Overlap integral factors in integrated optic modulators and switches, Journal of Lightwave Technology **7**, 1063–1070 (1989).

[204] M. Aillerie, F. Abdi, M. D. Fontana, N. Théofanous, and E. Abarkan, Accurate measurements of the electro-optic coefficients and birefringence changes using an external modulation signal, Review of Scientific Instruments **71**, 1627–1634 (2000).

[205] A. Youssefi, I. Shomroni, Y. J. Joshi, N. R. Bernier, A. Lukashchuk, P. Uhrich, L. Qiu, and T. J. Kippenberg, A cryogenic electro-optic interconnect for superconducting devices, Nature Electronics 2021 4:5 **4**, 326–332 (2021).

[206] J. Parravicini, J. Safioui, V. Degiorgio, P. Minzioni, and M. Chauvet, All-optical technique to measure the pyroelectric coefficient in electro-optic crystals, Journal of Applied Physics **109**, 10.1063/1.3544069 (2011).

[207] R. Schmidt and R. Alferness, Directional coupler switches, modulators, and filters using alternating $\Delta\beta$ techniques (Invited Paper), IEEE Transactions on Circuits and Systems **26**, 1099–1108 (2004).

[208] H. Kogelnik and R. V. Schmidt, Switched Directional Couplers with Alternating dB, IEEE Journal of Quantum Electronics **12**, 396–401 (1976).

[209] E. E. Wollman, V. B. Verma, A. E. Lita, W. H. Farr, M. D. Shaw, R. P. Mirin, and S. Woo Nam, Kilopixel array of superconducting nanowire single-photon detectors, Optics Express **27**, 35279 (2019).

[210] F. Marsili et al., Detecting single infrared photons with 93% system efficiency, Nature Photonics **7**, 210–214 (2013).

[211] A. J. Kerman, J. K. W. Yang, R. J. Molnar, E. A. Dauler, and K. K. Berggren, Electrothermal feedback in superconducting nanowire single-photon detectors, Physical Review B **79**, 100509 (2009).

[212] T. Schapeler, J. Philipp Höpker, and T. J. Bartley, Quantum detector tomography of a 2×2 multi-pixel array of superconducting nanowire single photon detectors, Optics Express **28**, 33035 (2020).

[213] A. G. Kozorezov, C. Lambert, F. Marsili, M. J. Stevens, V. B. Verma, J. P. Allmaras, M. D. Shaw, R. P. Mirin, and S. W. Nam, Fano fluctuations in superconducting-nanowire single-photon detectors, Physical Review B **96**, 1–13 (2017).

[214] M. Caloz, M. Perrenoud, C. Autebert, B. Korzh, M. Weiss, C. Schönenberger, R. J. Warburton, H. Zbinden, and F. Bussières, High-detection efficiency and low-timing jitter with amorphous superconducting nanowire single-photon detectors, Applied Physics Letters **112**, 061103 (2018).

[215] M. Caloz, B. Korzh, E. Ramirez, C. Schönenberger, R. J. Warburton, H. Zbinden, M. D. Shaw, and F. Bussières, Intrinsically-limited timing jitter in molybdenum silicide

superconducting nanowire single-photon detectors, Journal of Applied Physics **126**, 10.1063/1.5113748 (2019).

[216] S. Bogdanov, M. Y. Shalaginov, A. Boltasseva, and V. M. Shalaev, Material platforms for integrated quantum photonics, Optical Materials Express **7**, 111 (2017).

[217] J.-H. Kim, S. Aghaeimeibodi, J. Carolan, D. Englund, and E. Waks, Hybrid integration methods for on-chip quantum photonics, Optica **7**, 291 (2020).

[218] F. Thiele, F. vom Bruch, V. Quiring, R. Ricken, H. Herrmann, C. Eigner, C. Silberhorn, and T. J. Bartley, Cryogenic electro-optic polarisation conversion in titanium in-diffused lithium niobate waveguides, Optics Express **28**, 28961 (2020).

[219] F. Thiele et al., Cryogenic electro-optic modulation in titanium in-diffused lithium niobate waveguides, Journal of Physics: Photonics **4**, 034004 (2022).

[220] A. N. McCaughan, V. B. Verma, S. M. Buckley, J. P. Allmaras, A. G. Kozorezov, A. N. Tait, S. W. Nam, and J. M. Shainline, A superconducting thermal switch with ultrahigh impedance for interfacing superconductors to semiconductors, Nature Electronics **2**, 451–456 (2019).

[221] F. Thiele, T. Hummel, M. Protte, and T. J. Bartley, Opto-electronic bias of a superconducting nanowire single photon detector using a cryogenic photodiode, APL Photonics **7**, 081303 (2022).

[222] S. Krapick, M. Hesselberg, V. B. Verma, I. Vayshenker, S. W. Nam, and R. P. Mirin, Superconducting Single-Photon Detectors with Enhanced High-Effciency Bandwidth, arXiv, 1–25 (2017).

[223] M. Stefszky, M. Santandrea, F. vom Bruch, S. Krapick, C. Eigner, R. Ricken, V. Quiring, H. Herrmann, and C. Silberhorn, Waveguide resonator with an integrated phase modulator for second harmonic generation, Optics Express **29**, 1991 (2021).

[224] J. L. O'Brien, A. Furusawa, and J. Vučković, Photonic quantum technologies, Nature Photonics **3**, 687–695 (2009).

[225] F. Thiele, T. Hummel, A. N. McCaughan, J. Brockmeier, M. Protte, V. Quiring, S. Lengeling, C. Eigner, C. Silberhorn, and T. J. Bartley, All optical operation of a superconducting photonic interface, (2023).

[226] S.-W. Huang, E. Granados, W. R. Huang, K.-H. Hong, L. E. Zapata, and F. X. Kärtner, High conversion efficiency, high energy terahertz pulses by optical rectification in cryogenically cooled lithium niobate, Optics Letters **38**, 796 (2013).

[227] S. Carbajo, J. Schulte, X. Wu, K. Ravi, D. N. Schimpf, and F. X. Kärtner, Efficient narrowband terahertz generation in cryogenically cooled periodically poled lithium niobate, Optics Letters **40**, 5762 (2015).

[228] W. R. Huang, S.-W. Huang, E. Granados, K. Ravi, K.-H. Hong, L. E. Zapata, and F. X. Kärtner, Highly efficient terahertz pulse generation by optical rectification in stoichiometric and cryo-cooled congruent lithium niobate, Journal of Modern Optics **62**, 1486–1493 (2015).

[229] S. B. Lang, *Sourcebook of pyroelectricity*, Vol. 2 (CRC Press, 1974).

[230] S. Jachalke, E. Mehner, H. Stöcker, J. Hanzig, M. Sonntag, T. Weigel, T. Leisegang, and D. C. Meyer, How to measure the pyroelectric coefficient?, Applied Physics Reviews **4**, 10.1063/1.4983118 (2017).

[231] J. D. Brownridge and S. Raboy, Saturation of Spontaneous Polarization Charge in Pyroelectric Crystals of LiNbO3, LiTaO3 and CsNO3 at Low Temperature Above 4.2 K, (2002).

[232] R. W. Boyd, A. L. Gaeta, and E. Giese, "Nonlinear Optics", in (Academic Press Inc., Rochester, Ney York, 2023), pp. 1097–1110.

[233] G. Kötitz, Properties of lithium niobate, EMIS,The Institution of Electrical Engineers, London and New York 1989 **25**, 720–720 (1989).

[234] S. Sanna and W. G. Schmidt, LiNbO 3 surfaces from a microscopic perspective, Journal of Physics: Condensed Matter **29**, 413001 (2017).

[235] S. Korotky and J. Veselka, An RC network analysis of long term Ti:LiNbO3 bias stability, Journal of Lightwave Technology **14**, 2687–2697 (1996).

[236] E. Jones, T. Oliphant, P. Peterson, et al., *SciPy: open source scientific tools for Python*, 2001.

[237] Y. V. Shaldin, V. T. Gabriélyan, and S. Matyjasik, Pyroelectric properties of real LiNbO3 single crystals grown from a congruent melt, Crystallography Reports **53**, 847–852 (2008).

[238] I. S. Akhmadullin, V. A. Golenishchev-Kutuzov, S. A. Migachev, and S. P. Mironov, Low-temperature electrical conductivity of congruent lithium niobate crystals, Physics of the Solid State **40**, 1190–1192 (1998).

Appendix

A.1 SPICE model of a cryogenic photodiode

The cryogenic photodiode can be described with a SPICE subcircuit. To closely match the model to the real photodiode, the maximum power point, the shunt current as well as the open circuit voltage needs to be determined.

```
*Cryogenic Photodiode
*
.subckt Photodiode 1 2 3 ;
xu1 1 2 3 PV_cplx voc=0.5 isc=5.0e-6 vmp=0.375 imp=3.64e-6
.ends
*
*PhotoVoltaic Cell model
*
* necessary parameters
*voc - open circuit voltage
*isc - short circuit current
*vmp - maximum power voltage
*imp - maximum power current
*
.subckt PV_cplx v+ v- illu
D1 N002 v- pvdiode2
Rsh N002 v- R=rsh
Rs N002 v+ R=rs
Bph v- N002 I=ipv*v(illu)/1
R5 illu 0 5E-6
.param rs (voc-vmp)/(2*imp)
.param rsh vmp/(isc-imp)
.model PVDiode2 D(Is=io N=a_n Tnom=temp)
.param io ((rs+rsh)*isc-voc)/(rsh*exp(voc/(a_n*vt)))
.param vt (1.38e-23*(273+temp))/1.6e-19
.param ipv isc*(rsh+rs)/rsh
.param a_n 1.2*voc/0.55
*
.ends

```

Acknowledgements

B

An dieser Stelle möchte ich mich bei allen Beteiligten bedanken, die mich während des Physikstudiums und der Zeit als Doktorand begleitet haben.

Zunächst möchte ich meinen bei meinem Mentor und Professor Tim Bartley bedanken. Zum Einen für die Möglichkeit interessante Projekte zu verwirklichen und unkonventionelle Lösungswege auszuprobieren. Zum anderen als Mentor der mir im wissenschaftlichen Lernprozess zur Seite gestanden hat.

Ich möchte mich herzlich bei meinem Zweitprüfer Professor Klaus Jöns bedanken, der mir die Möglichkeit der Prüfung gibt.

Die Projekte und den Erfahrungsgewinn konnte ich niemals ohne ein super Team realisieren. Ich möchte mich hier für eine tolle Zusammenarbeit mit meiner Arbeitsgruppe die Mesoskopische Quantenoptik bedanken; Dr. Jan Philipp Höpker, Dr. Evan Meyer-Scott, Moritz Bartnick, Dr. Johannes Tiedau, Dr. Stephan Krapick, Nina Lange, Timon Schapeler, Dr. Maximilian Protte, Julian Brockmeier, Johanna Biendl, Felix Dreher, Dominik Kostiuk, Elias Wippermann, Dr. Thomas Hummel, Waqaar Hussain, Niklas Lamberty, Markus Brieden, Isabell Mischke, Niklas Schröder, Stefan Vorwerk, Jessika Bruns, Anupam Kumar.

Im Rahmen dieser Arbeit möchte ich mich insbesondere bei Dr. Thomas Hummel der als Sparringspartner und Mentor bereit stand. Für die (un)produktive Zeit möchte ich mich ebenfalls bei Julian bedanken. Insbesondere während einer langen Zeit der Einschränkungen habt ihr Beiden viel Abwechslung im Alltag geschaffen (Team Tunics). Vielen Dank an Maxi der nicht nur den ein oder anderen Sample fertigstellen musste, sondern auch eine gute Laune mitgebracht hat. Nina, ich hoffe wir haben uns nicht zu sehr auf dem optischen Tisch beharkt und vielen Dank für deine Feedbacks. Timon, besten Dank für deine Programmiertipps und den Feedback beim Schreiben. Johanna, vielen Dank für die schnellen Hilfen im Reinraum und die gute Laune. JP, vielen Dank nochmal für die Unterstützung besonders als unsere Gruppe noch in ein Aquarium passte.

Unsere Projekte funktionieren nur schwer ohne optische Schaltkreise. Deshalb möchte ich mich insgesamt bei der Arbeitsgruppe der Integrierten Quantenoptik von Professor Christine Silberhorn bedanken. Mein besonderer Dank geht an Felix vom Bruch der mir bei der mir die Probenherstellung übernommen hat und auch sonst für dein Feedback. Des Weiteren möchte ich mich bei Dr. Christof Eigner, Dr. Harald Herrmann, Sebastian Lengeling, Raimund Ricken und Viktor Quiring für eure Mitarbeit bedanken.

Einzelne Photonen zu detektieren ist nicht einfach. Deshalb möchte ich mich bei unseren Projektpartnern am NIST bedanken; Sae Woo Nam, Adriana Lita, Varun Verma. Insbesondere möchte ich mich nochmal bei Adam McCaughan für ein aufschlussreiches Gespräch bedanken.

An dieser Stelle möchte ich mich ebenfalls bei dem Projektträger dem BMBF im Quantum Futur Projekt für die finanzielle Unterstützung bedanken.

Das Studium und der Laboralltag sind das Eine. Freizeit mit Freunden das Andere. Vielen Dank für eure Unterstützung und für die vielen schönen Abende online und offline gehen an Gesche Vigh, Mario Littmann und Marvin Krenz.

Theoretisch ist praktisch alles möglich, aber man muss es umsetzen. Ich möchte mich herzlich die Unterstützung vom Löschzug Wewer bedanken. Ein besonderer Dank geht an Holger, Henrik, Michael, Carolin und Fabian.

Eine herzliches Dankeschön möchte ich mich auch an meine Familie aussprechen, die mich stets unterstützt hat. Danke Karin, Alfons, Henrik, Lisa, Mathilde, Franz-Josef, Rita und Ralf. Mein Dank geht natürlich auch an die Familie Volmert und Sandmann die mich unterstützt haben.

Mein größter Dank geht an meine liebevolle, geduldige, aufmunternde, verständnisvolle, herzliche Freundin und Partnerin im Leben; Ruth.

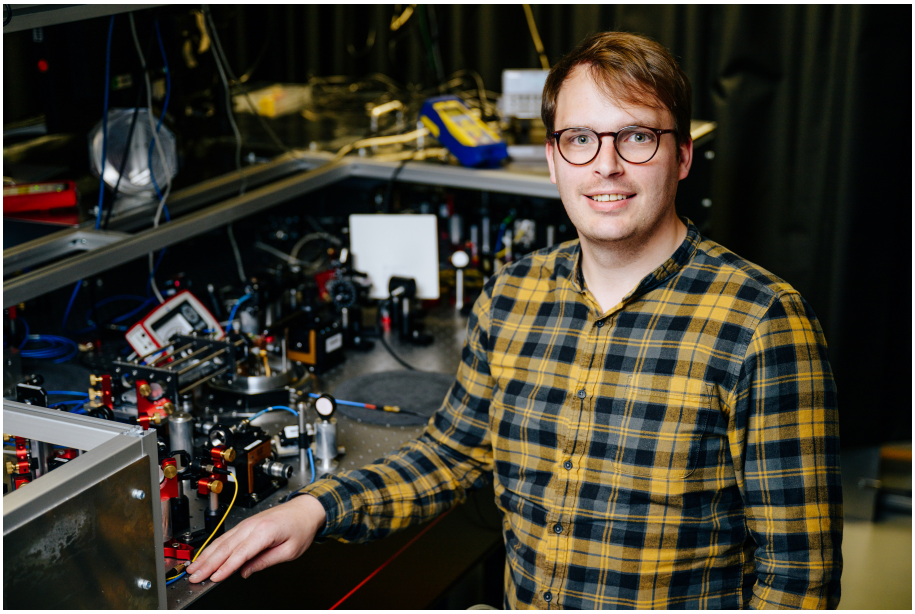

provided by Besim Mazhiqi

Erklärung

C

Ich versichere, dass ich die Arbeit ohne fremde Hilfe und ohne Benutzung anderer als der angegebenen Quellen angefertigt habe und dass die Arbeit in gleicher oder ähnlicher Form noch keiner anderen Prüfungsbehörde vorgelegen hat und von dieser als Teil einer Prüfungsleistung angenommen worden ist. Alle Ausführungen, die wörtlich oder sinngemäß übernommen worden sind, sind als solche gekennzeichnet.

Ort, Datum

Unterschrift